CURALF

CUbesat for Radio Astronomy at Low Frequencies

P. Manchanda

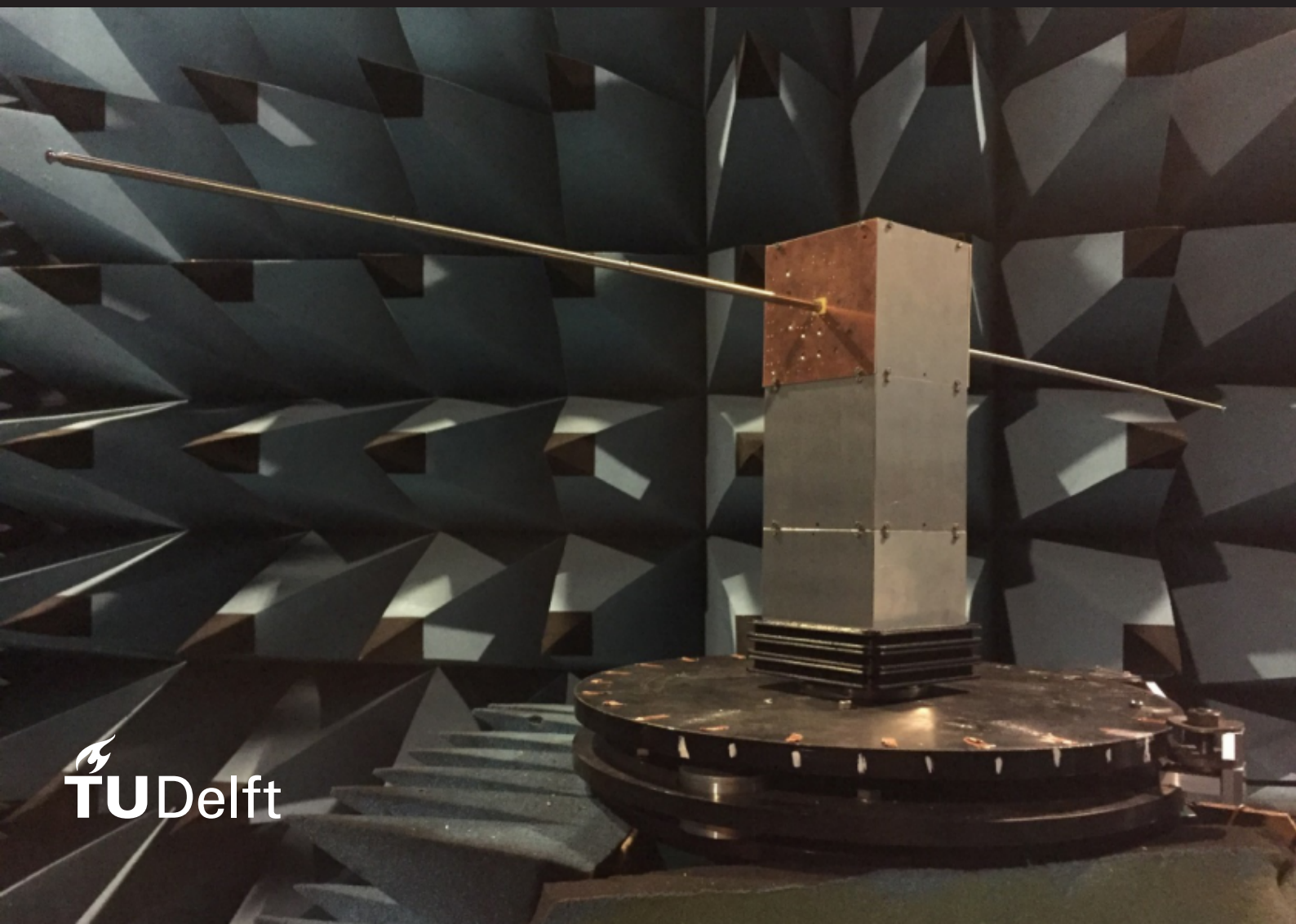

TU Delft

CURALF

CUbesat for Radio Astronomy at Low Frequencies

by

P. Manchanda

to obtain the degree of Master of Science
at the Delft University of Technology.
to be defended publicly on Monday November 25,2019.

Student number: 4718259

Thesis committee:

Prof. dr. ir. C.J.M. Verhoeven,	TU Delft, supervisor
Ir. A. Montagne,	TU Delft, daily supervisor
Prof. dr. ir. W.A Serdijn,	TU Delft
Prof. dr. ir. M. Bentum,	Eindhoven University of Technology, ASTRON
Dr. ir. D. Prinsloo,	Eindhoven University of Technology, ASTRON

Abstract

Space launches have been steadily increasing over the years as satellites are being used in various applications such as communication, military, and science. The costs of launching satellites are still high and depend on the dimensions and weight of the satellite. With the advancement in the field of autonomous robotics and telecommunications, the need for multiple satellites in swarms and constellations is also growing. Cubesats have emerged as an alternative for these issues as they provide a low cost and compact solution.

After the successful launch of NCLE (Netherlands China Low-Frequency explorer), a radio astronomy payload in the Chang'e 4 mission, efforts are being made to reduce the size of the payload to meet the cubesat standards. This work aims at investigating the design and implementation of a sensitive radio receiver for low-frequency radio astronomy from the lunar orbit with a cubesat platform. The aim is to study the practical aspects involved in realizing the design and improving the sensitivity of the instrument. The science objectives are similar to that of the NCLE payload which includes the frequency band of 80 kHz-80 MHz with high dynamic range and linearity. The thesis is a step further in the project OLFAR which aims to have a swarm of satellites in the lunar orbit to perform long-baseline interferometry at low frequencies.

This work focuses on the analog signal chain of the payload which contains the antenna, low noise amplifier, filters, and the ADC. For the design of the antenna, the antenna length, efficiency, and IXR of three antenna configurations have been presented. As radio frequency interference poses a problem during the design of the amplifier chain, the effects and coupling mechanisms of RFI have also been studied. Limits on all internal and external instruments for radiated emissions have been set for the design to be sky noise limited. The amplifier design takes the science cases into account and is designed to achieve the required sensitivity, using a structured electronic design approach. The implementation of the amplifier chain was done with discrete components at ASTRON (Netherlands Institute for Radio Astronomy) and measurement results have also been discussed at the end.

Acknowledgement

As the thesis was done in collaboration with TU Delft and ASTRON, I had the opportunity to meet some very inspiring and talented people throughout my thesis. Although it was a difficult challenge, I am glad that I pursued this area of research as it has helped me immensely in improving my technical abilities as an electronics design engineer.

First and foremost, I would like to sincerely thank my supervisor, Professor Chris Verhoeven for providing me with the opportunity to pursue research in the field of radio astronomy. Along with Anton Montagne, for making me understand the true procedure of structured electronic design which has helped me a lot not only during the thesis work but also in my personal life. Their guidance and support has been vital throughout the thesis. I would also like to thank Samaneh, Vishu, Raj and Maneesh for their help.

I would like to extend my gratitude to my guide at ASTRON, Mark Ruiter for helping me on a daily basis and answering all my queries in the field of RF and practical electronics design. I would also like to thank David Prinsloo, Michel Arts for helping me to establish my knowledge in the field of antenna design and the long discussions that we had in their office. I enjoyed sharing my office at ASTRON with Paulus Kruger who also helped me clear all my doubts no matter how silly they sounded.

I would also like to thank my friends Rishab, Abhairaj, Yaswanth, Pinakin, Shardul, Shubham, Anirudh, Raghu, Onam, Sahil and Krishna for helping and supporting me whenever I needed it.

A special thanks go to my computers that have endured my rough and long usage. I would also like to acknowledge the entire Dutch medical system that provided nurses for home care after my surgery, which allowed me to recover faster and continue my work on the thesis.

None of this would have been possible without the support, belief, and trust of my parents and family. I would like to dedicate this thesis to all the engineers and their contributions towards pushing the boundary of science.

P. Manchanda
Delft, November 2019

Contents

List of Figures

List of Tables

1 Introduction

Radio astronomy deals with the observation of the universe in the radio frequency band of the electromagnetic spectrum. It is a comparatively new branch of astronomy which has its root from the observation of the cosmic microwave background by Karl Jansky in 1931 [1]. Since his observation, radio telescopes have helped in several other major discoveries such as millisecond pulsars and the detection of new exoplanets. Recently, the first image of a black hole M87 was taken with the help of eighth radio telescopes situated at different geographical locations all around the world. Figure 1.1 shows the captured image.

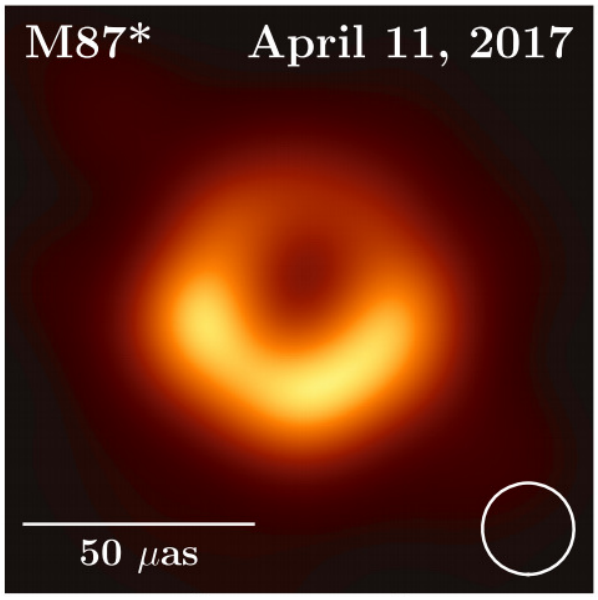

Figure 1.1: First ever black hole image was taken via combining data from eighth different radio telescope around the world.[2]

Apart from this, radio telescopes are also used to study the neutral hydrogen line at 1420 MHz which helps in determining the velocity, mass, and composition of individual galaxies. These observations are done in the higher radio spectrum, but in recent times, there has been a shift in focus towards low-frequency radio astronomy as it is one of the least explored windows in radio astronomy. Low-frequency observations provide a window into the past and study the Epoch of Reionization (EOR) [3], which is the time when the neutral gas in the universe became instantly ionized. This is one of the least understood epochs in the history of the universe.

Earth-based telescopes make observations from 30 MHz up to 1 THz. Telescopes such as LOFAR (LOw Frequency ARray) and UTR2 (Ukrainian T-shaped Radio telescope, second modification) observe low frequencies from around 10-240 MHz and 8-40 MHz respectively. The latest addition to the list is the SKA

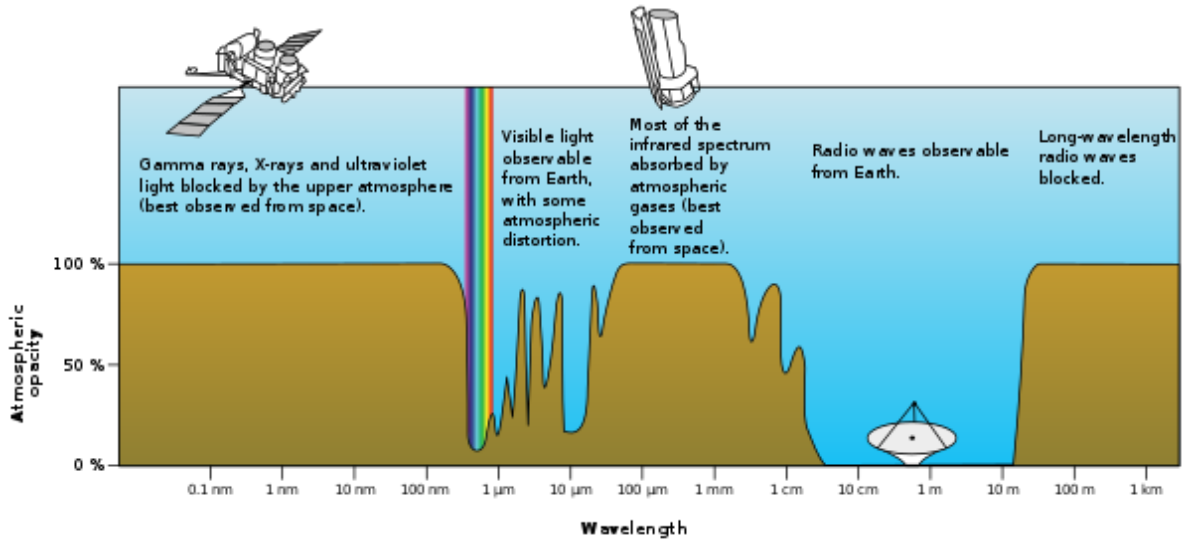

Figure 1.2: An image showing the opacity of the Earth's atmosphere for different wavelengths. It can be seen that short and long wavelengths are extremely difficult to observe them from Ground based telescopes [4].

(Square Kilometer Array), which is a phased array telescope in a one square kilometer area and plans to make observations from 50 MHz to 14 GHz. The atmosphere plays a major role in the inability to make observations at frequencies lower than 30 MHz as the atmosphere becomes opaque at those low frequencies. Figure 1.2 shows the atmospheric opacity with respect to wavelength. It can be seen from the figure that the Earth's atmosphere is completely opaque for long wavelengths.

Apart from opaqueness and distortions from the atmosphere, Radio Frequency Interferences (RFIs) also makes it difficult to make sensitive observations from ground-based telescopes. The interference can be of both natural and man-made origin. Man-made sources include HF transmitters, AM transmissions, etc. While the natural phenomenons include auroral discharges and lighting. These are broadband noise sources and therefore are difficult to fully characterize, making it difficult to remove them from observational data. Various techniques and methods have been developed to overcome these problems, such as modeling of the atmosphere, use of guide stars removal of uncorrelated noise, etc. But there is another solution to all these problems, space-based radio astronomy.

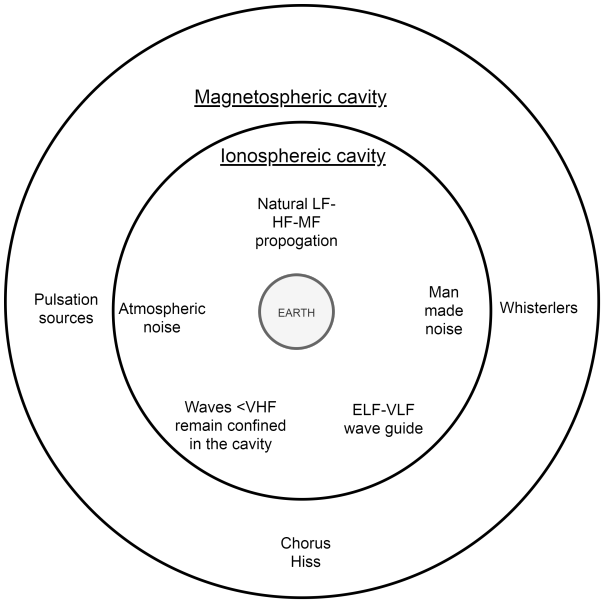

Figure 1.3: Image showing man-made and natural sources of RFI around the Earth.

Figure 1.3 shows various man-made and natural RFI sources from [5]. It can be seen that there are man-made and naturally occurring noise sources. These cause problems while making sensitive observations and show up in the measurement spectra.

The next section discusses the past missions and the vision for the future of space-based radio astronomy. Science objectives that can be achieved by long-baseline observation from space and the requirements for radio receiver are also discussed.

1.1. Space based Low-Frequency Radio Astronomy

Space missions provide a good solution towards mitigating the effects of atmosphere and radio frequency interference. There have been very few missions to explore the low-frequency sky apart from RAE 1 and RAE 2, which were launched in 1968 and 1973 respectively. The payload for RAE 2 consisted of two V-shaped 229 meter long antennas and a 37-meter dipole antenna. The missions were able to provide information about the absolute spectrum of the cosmic background noise and low-frequency planetary emissions from planets, especially from Jupiter. It was also able to study the solar corona and solar bursts, which are high power emissions from the sun. The two main outcomes from these missions which have helped steer the branch of space radio astronomy were the detection of intense and wide-band man-made radio emissions from Earth and the identification of a potential shielding spot from this noise at the Earth-Moon Lagrange point 2 [6]. Interestingly, RAE 2 was placed at the lunar orbit to achieve shielding from man-made interference detected by RAE 1.

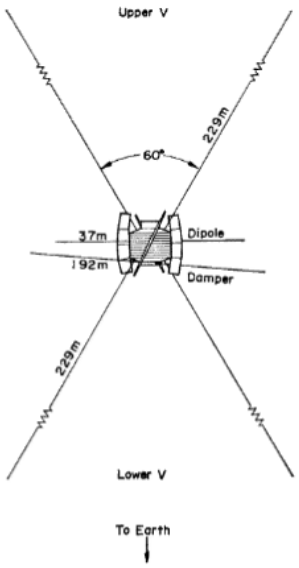

Figure 1.4: Image showing the antenna configuration of the RAE 2 payload on the explorer 38.[6]

Figure 1.4 shows the configurations of the 4 antennas that were used in the mission. These satellites were the first dedicated satellites for radio astronomy. The size of the satellites are quite large due to the long antennas which were used.
A lunar orbit is a suitable place for such missions because of the suppression of Earth-based radio frequency emissions. The data provided by RAE 2 shows there is a suppression of interference when the satellite is behind the moon with respect to Earth.

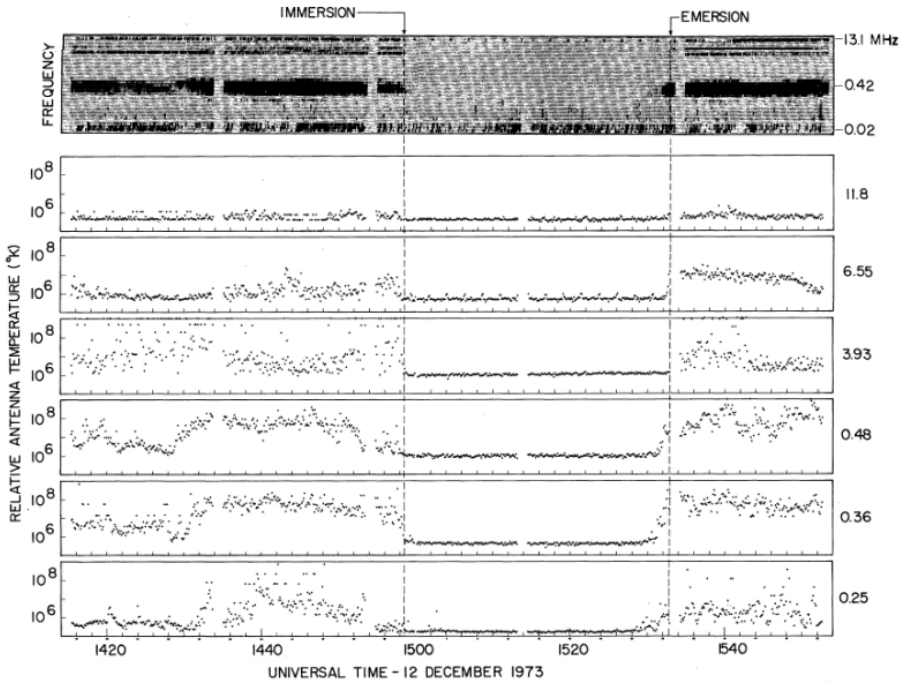

Figure 1.5: Image showing the extra suppression of interference provided by the Moon. [7]

Figure 1.5 shows the reduction in antenna temperature aboard the RAE 2 satellite. These satellites were decommissioned at the end of their lifetime, which is a natural consequence that satellite systems face. It is more convenient to have a big dish telescope in space which can provide sensitive data. But due to observations at such long wavelengths, the size of the telescope would be impractical to build even on Earth. To overcome this issue, a technique called interferometry is used.

1.1.1. Interfeometry

The angular resolution of a telescope depends upon the wavelength of observation and the diameter of the telescopes.

$$\theta = \frac{1.22\lambda}{D} \tag{1.1}$$

Where θ is the angular resolution in radians, λ is the wavelength of observation and D is the diameter of the antenna in meters. For example, for observation of a 3.7 km (80 kHz) wavelength at an angular resolution of 1 radian, a diameter of roughly 4.5 km would be required. This is too large not only for space-based telescopes but also for Earth-based telescopes as currently, the largest radio telescope FAST (Five hundred meter aperture spherical telescope) is 1 km in diameter.
To solve this issue, various telescopes are combined to form a virtual telescope. This technique is called interferometry. The size of the virtual telescope can be as large as the distance between the farthest telescopes, which increases the angular resolution by several factors. Figure 1.6 shows the basic concept of interferometry where two telescopes are used to detect the source and their data are combined to get a better resolution. The data from each telescope first goes through a beamformer to look at specific areas of the sky and then through a correlator to combine the data from different telescopes. This technique not only helps in achieving high angular resolutions but also helps to eliminate uncorrelated noise, thus providing better sensitivity.

For these advantages, it is beneficial to have an interferometer in space instead of a usually large dish. But the physical dimensions of these satellites are too large to send multiple units to achieve long baseline interferometry from space. The development and launching costs would be extremely high. Therefore, a more practical solution is needed.

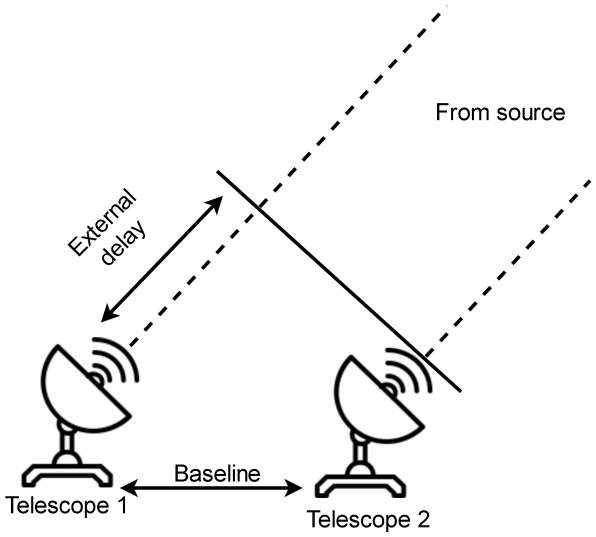

Figure 1.6: Image showing the concept of interferometry with two telescopes. The time delay at the first telescope can be compensated digitally to form a virtual telescope

1.1.2. Towards space-based low-frequency radio astronomy baselines

]The idea of having baselines in space is not new. Many studies have been conducted in the past which have proposed building telescope on the surface of the moon or with orbiting satellites at the lunar orbit. Project OLFAR aims at deploying scalable autonomous swarm which can perform low-frequency radio astronomy. Figure 1.7 shows the road-map of the OLFAR project.

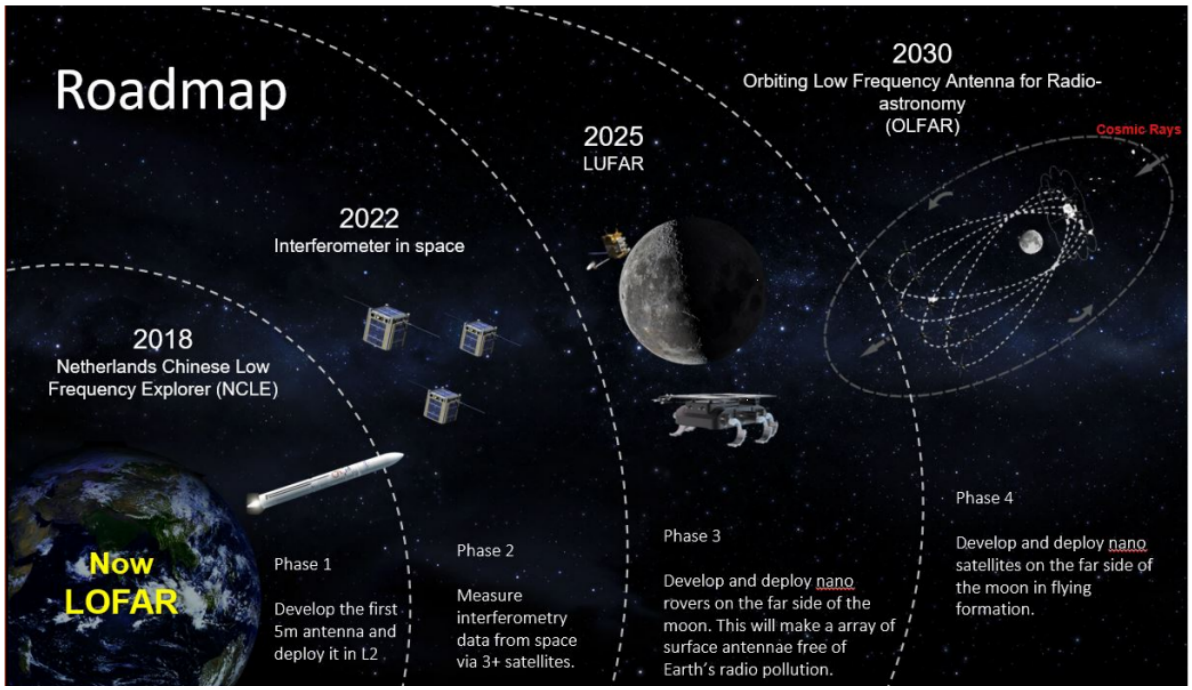

Figure 1.7: The raod-map of the OLFAR project which aims to have a scalable autonomous swarm of satellites in the lunar orbit to perform low frequency radio astronomy.[8]

With the recent successful launch of the relay satellite Chang'e 4 containing the NCLE (Netherlands China Low-frequency Explorer) payload, a step has been taken towards performing low-frequency radio astronomy from the Earth-Moon Lagrange point L2. The payload contains three 5-meters monopole antennas and aims to observe in the bandwidth of 80 kHz to 80 MHz. Apart from providing new insights into the low-frequency data from the universe, it can also provide conclusive evidence of shielding of the interference by the Moon

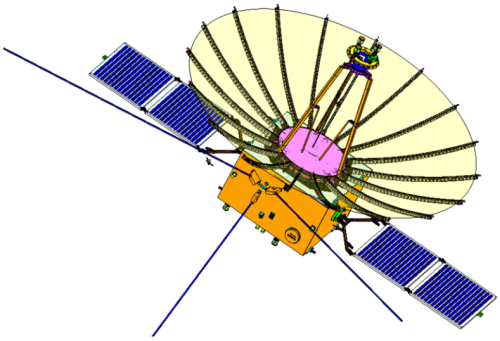

Figure 1.8: Image showing a model of the Chang'e 4 satellite containing the NCLE payload with three 5-meter antennas.

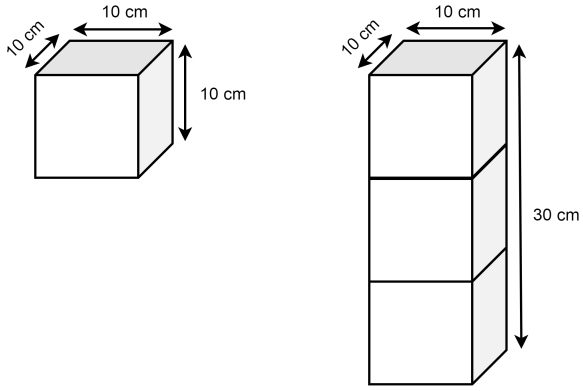

Figure 1.9: Figure showing the dimensions of 1U cubesat and how they can be stacked together to make larger satellites.

to establish the site for future missions.

Figure 1.8 shows a model of the Change'4 relay satellite which contains the NCLE payload. The satellite is primarily used to establish a communication link between the Chinese rover on the far side of the moon to the Earth, therefore contains a large dish antenna for communication purposes. The three monopole antennas can be seen that is used for the radio astronomy payload. As this is not a dedicated satellite for radio astronomy, there can be several factors that could hinder performing sensitive observations. Therefore there is a need for the development of dedicated satellites for radio astronomy. As seen from figure 1.7 the concept of OLFAR uses cubesat technology for establishing the orbiting low-frequency antenna for radio astronomy.

1.1.3. Why small satellites

The launching costs of satellites depend on various factors such as the dimensions and weight of the satellite. As seen from previous examples of RAE missions and NCLE, the cost of launching these satellites are immense as the amount of fuel required to establish them in the required orbits is too high. Apart from launching costs, the development time and fabrication costs of numerous systems will only add to the costs.
With the emergence of small satellites, based on off the shelf technology, these costs can be minimized.

Emergence of small satellites

In 1999, standards were established for cubesat technology to help make space flight more accessible to universities and students. Since then there has been a steady increase in the launches of small satellites in various sectors of science. A cubesat unit dimension is standardized to a 10cm x 10cm x 10cm with a weight constraint of around 1.2 kg. Multiple units of such cubesats can be stacked together to make bigger units as shown in figure 1.9.
In the past, there was a concern regarding the success rate of these small satellites. But with time, advancements have been made to ensure that not only the launches become successful, but even that cubesats are used for actual scientific payloads. Figure 1.10 shows the number of cubesats launched from 2002 onward [9].

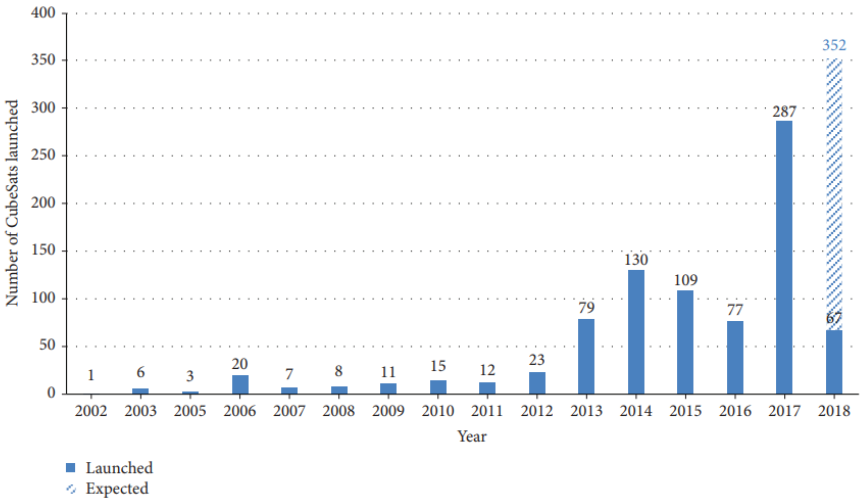

(a) Graph showing the number of cubesat launches per year since 2002

(b) Graph showing the success rate of cubesats per year since 2002

Figure 1.10: Statistics showing the number of launches the success rate over the years for cubesats.[9]

It can be seen that there has been a steady increase in the number of cubesats launched in recent years[9]. In the early days, there were several issues with the new technology and therefore the rate of the successful launch was low. But as seen in figure 1.10 (b), the success rate of cubesats has also been increasing steadily.

Although there are benefits of using small satellite technology in terms of launching costs, there are some challenges as well. Due to the weight and size constraints, the design of electronic circuits has to be carefully chosen as there might be no space to make systems redundant. Increasing the size of the cubesat would then lead to an increase in costs. Mechanical designs of antennas and other systems also have to be taken into consideration as the maximum weight cannot exceed 1.2 kg for a 1U cubesat.

Therefore cubesat provides compact and cost-effective solutions for interferometry in space as the number of nodes can range from 100s to 1000s.

We have established that small satellites provide a viable solution for deploying swarms in the lunar orbit for low-frequency radio astronomy. The next section describes the science objectives for which these missions are being planned as they lead to the requirement for various sub-systems of the payload.

1.2. Science Objectives

There have been several case studies which have brought forward numerous science cases for low-frequency astronomy [10–13],[14]. Some of the science cases are discussed here but they can be found be in detail in the above-mentioned literature.

- Cosmology
  The study of cosmology and the formation of structure in the universe is currently a fundamental question of research. The study of the highly red-shifted 21cm hydrogen line and the Epoch of reionization can be studied to give an insight into the so-called Dark ages beyond reionization. This would require measuring the power spectrum of the 21-cm line up to z=50, which would require a baseline in tens of km and a large number of antennas [8].

- Planetary and Solar transients Low-frequency radio astronomy can be used to study the emissions from the sun. The sun produces broadband radio bursts through its magnetic activity and its corona. These bursts can be dangerous to both humans and space electronics. The system dynamic range needs to be enough for the system to not saturate during these events. Whereas planets emissions are usually caused due to their magnetization and interaction with charged particles from solar winds and bursts. Jupiter is a major source of radio emissions in our solar system apart from the sun. These observations help us to understand the dynamics of our local solar system which is essential in finding exo-planets and intelligent life in the future.

- Space weather monitoring There is currently a gap in the monitoring of space weather such as coronal mass ejections from the sun and solar winds. Ground-based telescopes can only make observations till 30 MHz, and thus there is a need for observations at even lower frequencies. This can help in the prediction of such events and study their interaction with the Earth's atmosphere in greater detail.

- Surveys Apart from this, there is a goal to map the sky at these ultra-long wavelengths. Synchrotron emission from pulsars and radio galaxies can be observed. With a wideband receiver, highly redshift galaxies can be seen which enables us to look into the past and study the formation of galaxies and stars in the early universe. Apart from this, active galactic nuclei and galaxy clusters can also be studied in detail. With telescopes such as LOFAR and Murchison Widefield Array, low-frequency astronomy has benefited in several discoveries, but these can only be used till 30 MHz and the radio frequency interference from Earth are a limiting factor in their sensitivity.

The science cases are summarised in Figure 1.11 according to the band of emission and priority set by the NCLE mission. This work will follow the same case and use these science cases for the design of the analog receiver. The system-level specifications are also described in literature present for the OLFAR mission.

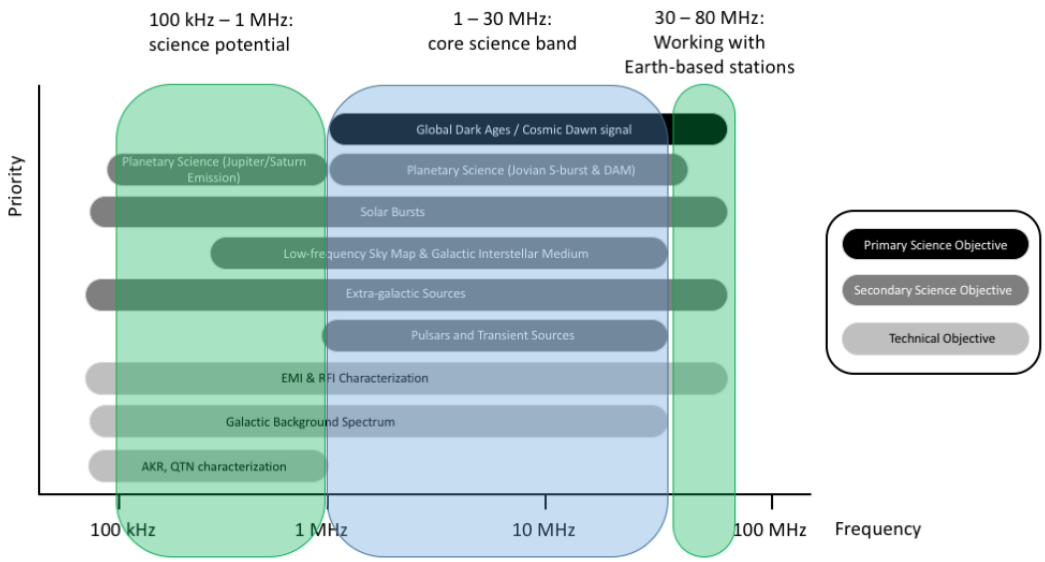

Figure 1.11: Summary of the science cases as per their emission band and priority as considered by the NCLE mission.

Using the science cases described above, various requirements have been derived for the system and subsystem level. These serve as a basis for the start of design and help to make design choices in the future.

1.3. Requirements

The requirements for the OLFAR mission have not been well defined. The requirements are derived from the science cases mentioned in section 1.2. They are summarised in table 1.1.

Table 1.1: Table summarizing the requirements from the OLFAR mission.

Parameter	Minimum	Unit
Observational Frequency Range	0.08-80	MHz
Number of antennas	2-3	
Maximum baseline	100	km
Dimension (board)	10x10	cm
Deployment location	Earth Moon Lagrangne point L2	-
Instantaneous bandwidth	20	MHz
Dynamic Range	50-90	dB
Temperature Range	-55 to 125	$^{\circ}C$

Several of the requirements specific to the analog receiver, are derived when separate subsystem components are being designed. As the project focuses on the implementation of radio receivers with small satellites, some of the requirements are much more important such as the dimensions and weight of various subsystems as the weight limit for cubesats is restricted. This leads to the study of antennas and other systems as to how can they be minimized.

These requirements serve as a basis for the design, but there are still some requirements that are specific to the analog signal chain which needs to be defined. These are done based on the signals and environment which the receiver is going to function in and done in specific sections of the text. There are some terms and concepts regarding the signals that are common in radio astronomy which appear often in the document. These are explained in detail in the next section.

1.4. Signals in Radio Astronomy

To derive various requirements such as receiver noise, dynamic range, and common-mode rejection ratio, a knowledge of the minimum and maximum signal levels that the system is expected to receive are needed. The low-frequency sky map has been made from various sources and can be found in detail in the works of Zarka et. al. [13]. The three major signals that are used throughout the work are the galactic background noise, solar flares and the noise requirement of the receiver. All these signals are first expressed in terms of spectral noise flux density. Figure 1.12 shows the levels of these signals.

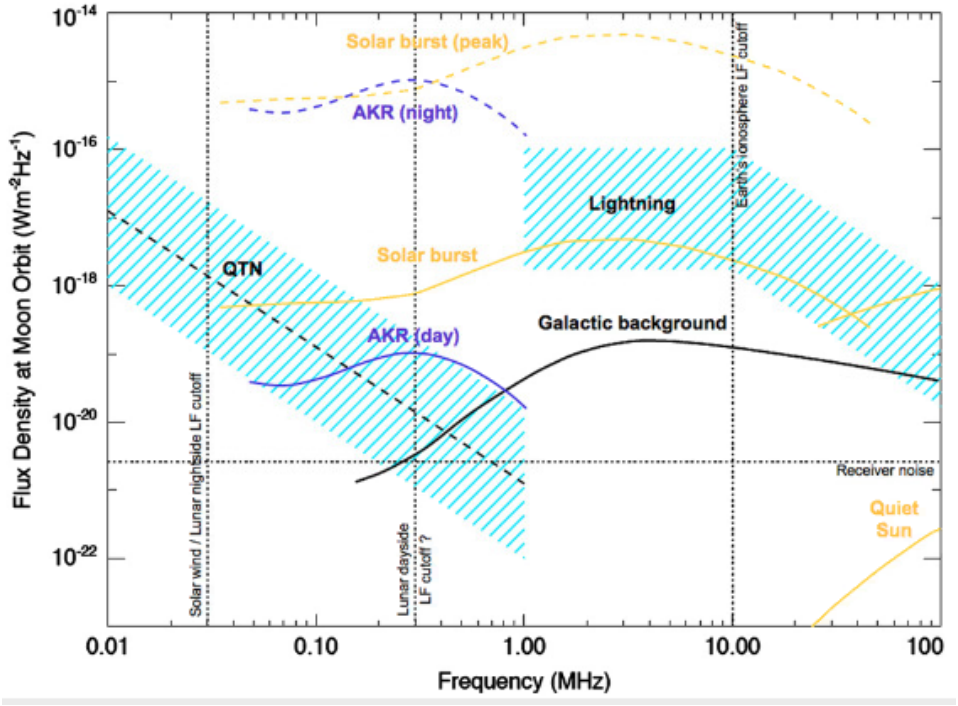

Figure 1.12: Image showing the levels of various signals from the lunar orbit including galactic background noise, solar bursts and quasi thermal noise.[13]

As seen in figure 1.12, the level of solar bursts(peak) is the highest, whereas the quite sun is seen at high frequencies.

1.4.1. Sky noise

There are various sources of "noise" present in space. The most commonly known source is the cosmic microwave background. Other sources of noise include radio source background noise, synchrotron radiation, and integrated extra galactic noise. All these sources combine to form a noise floor which will be called skynoise throughout this document. It serves as a reference level for other signals to compare with. It can be assumed that sky noise is an isotropic source of noise in which will be seen by the receiver in space-based radio astronomy. This is a mere simplification done to make the understanding of the system simpler. As seen in figure 1.12, there are two sources of noise to consider, the galactic background noise and QTN (Quasi Thermal Noise). At low frequencies ($simeq$1MHz), QTN starts to dominate over galactic background noise. Therefore the requirements for receiver noise contribution consider the combination of the QTN, galactic background noise synchrotron radiation, etc.

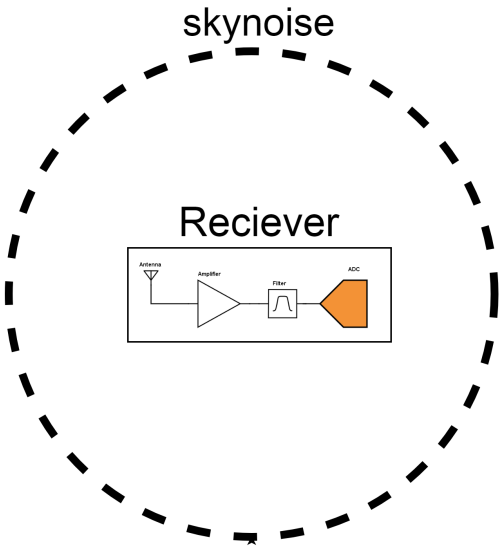

Figure 1.13: The galactic background noise is assumed to be isotropic, in which the receiver is analysed.

Figure 1.13 shows that the sky noise is assumed to an isotropic noise source which means that it is equal in all directions. A simple block diagram of the receiver chain is also shown which contains the antenna, amplifier, filter and the ADC. These are the basic blocks which are the analog components in a typical radio receiver. The sky noise is modelled using the work in [12]. The skynoise temperature can be modelled over frequency using the equation 1.2.

$$T_{\text{sky}} = \begin{cases} 16.3 \times 10^6 K \left(\frac{\upsilon}{2\text{MHz}}\right)^{-2.53} & \text{at } \upsilon > 2\text{MHz} \\ 16.3 \times 10^6 K \left(\frac{\upsilon}{2\text{MHz}}\right)^{-0.3} & \text{at } \upsilon \leq 2\text{MHz} \end{cases} \tag{1.2}$$

1.4.2. Solar Flares/Bursts

Another important high power signal in radio astronomy comes from the sun, referred to as space weather. As seen in 1.12, the spectral noise flux density of the quiet Sun is in the order of 10^{-22} $(W/m^2/Hz)$, whereas the active sun is around 10^{-15} $(W/m^2/Hz)$. The bursts can last for minutes to a few hours. Therefore these signals can deteriorate the functionality of the analog receiver and therefore needs to be considered during the design phase.

Table 1.2 shows the various kind of solar bursts from [15]. It can be seen that the noise temperature of type III are the highest. They can hinder the performance of the receiver by either producing unwanted high level signals or saturating the amplifier. Almost all the type of solar bursts are ultra wide-bandwidth and last for about a few minutes to weeks. These bursts need to characterized for the dynamic range requirement of the receiver.

Table 1.2: Table summarizing the different types of solar bursts with their frequency range, duration, polarization, noise temperature, and the emission mechanism.

Burst type	Duration at100 MHz or 10 GHz	Temperature (K)	Frequency range/ bandwidth	Emission mechanism
I	1 s	10^{10}	50-300 MHz/~1 MHz (burst)	fundamental plasma
I storm	days to weeks	10^{10}	~100 MHz (storm)	
III storm	days to weeks	10^{10}	50 MHz – 30 kHz/	fundamental and/or harmonic plasma
II	10 min	10^{8} – 10^{11}	200 $\rightarrow$ 1 MHz/10 MHz	fundamental and harmonic plasma
III	few seconds	10^{8} –10^{12} (to 10^{13} at~1 MHz)	200 $\rightarrow$ 1 MHz/10 MHz2 harmonics	fundamental and harmonic plasma
IV moving	~30 min	10^{8} – 10^{9}	200 $\rightarrow$ 10 MHz/>10 MHz	gyrosynchronous and/or plasma
IV flare continuum	~20 min	10^{8} – 10^{12}	200 $\rightarrow$ 10 MHz/100 MHz	plasma ?
IV storm continuum	few hours	> 10^{8}	50 – 300 MHz/100 MHz	fundamental plasma
V	>1 min	10^{8} – 10^{11}	100 $\rightarrow$ 10 MHz/50 MHz	harmonic plasma
Microwave impulse	>1 min(at 10 GHz)	10^{7} – 10^{9}	3 – 30 GHz/10 GHz	gyrosynchronous (Maxwellian or power law)
microwave IV	~10 min	10^{7}– 10^{9}	1 – 30 GHz/5 GHz	gyrosynchronous (power law)
microwave post-burst	minutes to hours	~ 10^{7}	1 – 10 GHz/5 GHz	thermal bremsstrahlung
microwave spike burst	~10 ms (burst)~10 min (group)	> 10^{13}	~0.5 – 5 GHz/few MHz	cyclotron maser

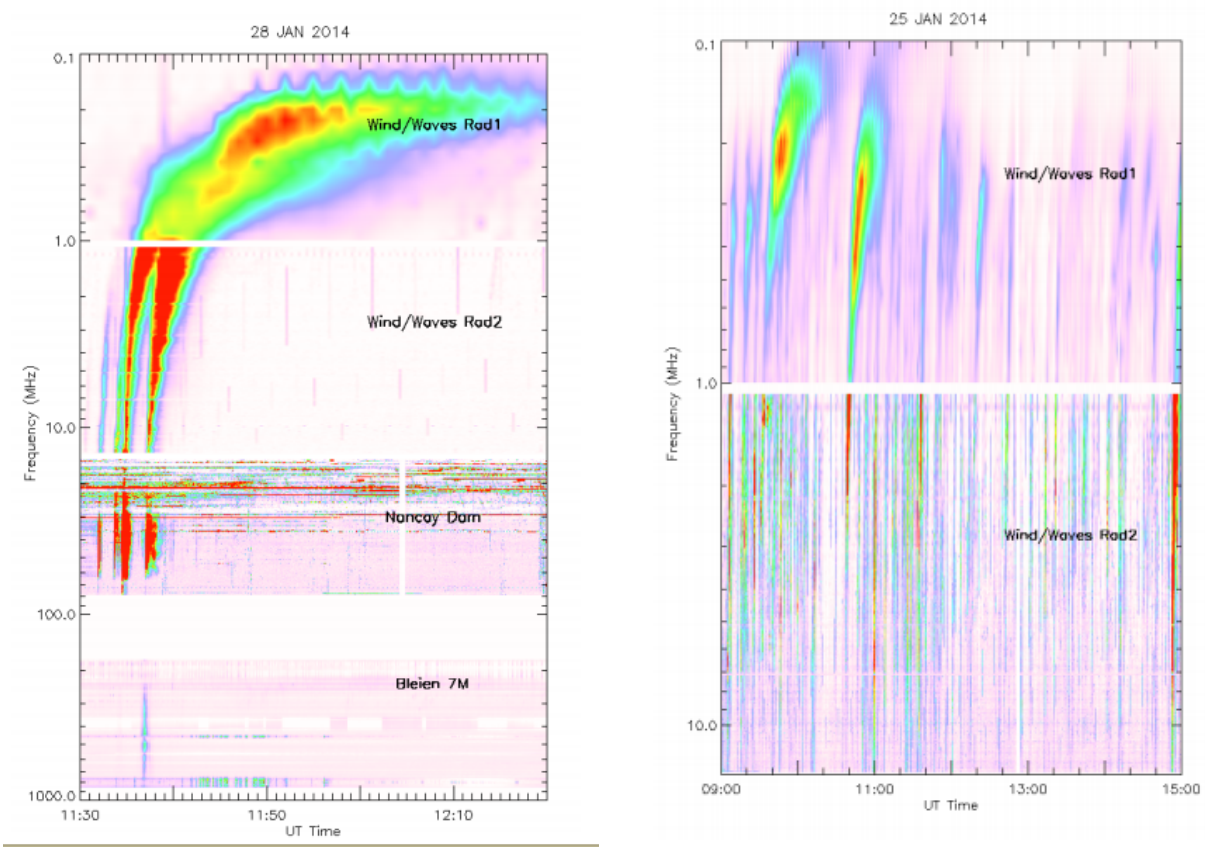

(a) (b)

Figure 1.14: Image showing the spectrum of a type *III* solar bursts. Figure (a) shows the wide-band spectrum measured from various telescopes. Figure (b) shows the spectrum measured from the WIND spacecraft.[16]

Figure C.2 from [16], show an example of type *III* solar bursts. The Figure C.2 (a) shows the measured solar bursts in different frequency bands from various telescopes such as Bleien telescope, Nancay Decametre Array and the WAVES experiment on-board the WIND spacecraft. It can be seen that there are various solar bursts recorded all over the frequency band but they seem to converge at low frequencies of around below 1 MHz which lies inside our band of interest. This convergence may cause an increase in power seen at the input of the analog chain and may cause saturation. If these bursts are for short duration, the effect would not damage or hinder observations. But as seen from the figure C.2 (b), solar bursts lasting 6 hours have been measured from the WIND spacecraft. It can be seen that they are distributed all over a wide frequency band and the intensity seems to be more towards the low frequencies. Therefore, solar bursts are both a good source to understand the physics and behavior of the sun and an important signal source for design parameters of the analog chain.

The level of sky noise and the science cases are used to set the noise contribution of the receiver. The noise contribution from the receiver has to be lower than that of sky noise to make the receiver sky noise limited. The three signals in spectral noise flux density are shown in figure 1.15

It is seen that long baselines are required to increase the angular resolution, and distributed network can be used instead of making big dish telescopes. The concept of small satellites is emerging as a viable alternative to big satellites if the number of satellites required are large. In radio astronomy the major signals which are used to design the analog chain are skynoise and solar burst. Now that the basics of radio astronomy and the need for small satellite radio receiver is presented, the next section explains the importance of this work.

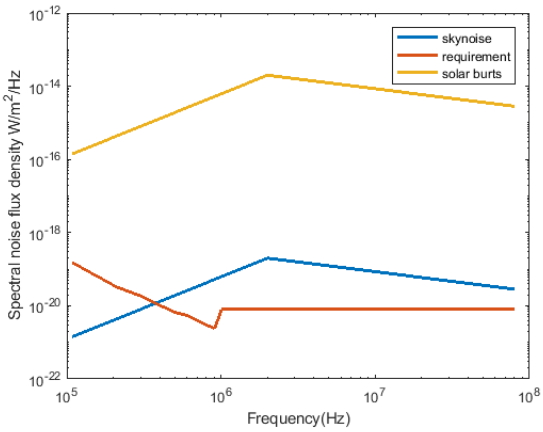

Figure 1.15: Image showing the skynoise, solar bursts and requirement level for the analog receiver chain in terms of spectral noise flux density.

1.5. This Work

This work focuses on a single unit cubesat for the OLFAR project. It aims to design and implement a sensitive radio receiver for the bandwidth of 80 kHz-80 MHz. There are various challenges in the design such as the type, length, and orientations of the antennas to be used. The effects of radio frequency interference and methods to mitigate its effects. The technology and topology of the amplifier that can be used for achieving higher sensitivity. Also, the work provides further requirements such as the limits on radiated and conducted emissions, the effect of the length of on the noise budget of the amplifier, the dynamic range of the system and the linearity of the system. The aim to test and measure the design and show proof of the concept that low-frequency radio astronomy can be performed with cubesats.

The first part of the thesis introduces some basic antenna concepts which are required to make design choices regarding the antenna. The polarization response of three different antenna configuration has also been presented. The next part of the thesis discusses radio frequency interference, its causes and effects on the overall system. Limit on the internal and external instruments on radiated emissions has been presented. Some measurement results for emission levels have also been discussed. In the next chapter, the requirements for the system design are discussed in detail. It also discusses the implementation of the low noise amplifier and filters . In the next section, measurement results are shown during which some issues with the design are identified. Methods to mitigate these problems and a new input stage has also been proposed. In the end, conclusions and talking points are presented.

2

Antenna Design

Introduction

The first part of the analog chain to be designed is the antenna. This chapter presents the background for antenna design with some fundamental concepts and definitions which are required to make design decisions for choosing the type of antenna to be used and its configuration. Figure 2.1 shows the basic block diagram of the analog receiver with the antenna highlighted, this is a basic representation of the analog chain.

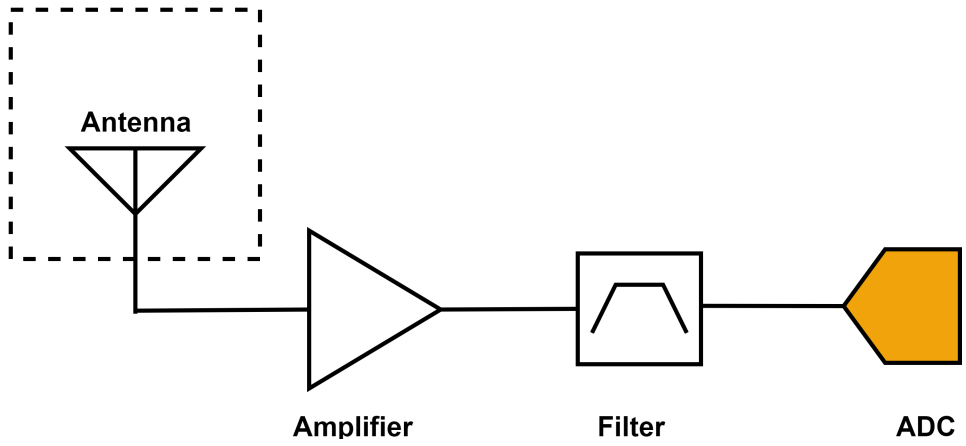

Figure 2.1: A basic block diagram of the analog chain.

Antenna, in general, can be used to detect and electric field or a magnetic field. In this work, the electric field is being measured as the loop antenna required for the detection of magnetic fields for such a wide-bandwidth will become impractical.

2.1. Antenna Theory

To evaluate the behavior of electromagnetic waves in free space, we start with the analysis of the simplest antenna, the Hertzian dipole. The Hertzian dipole is a theoretical construct rather than a physical entity. It is an infinitesimally small conductor [17].

2.1.1. Fields in free space

Assume a Hertzian dipole in free space-oriented along the z-axis, as shown in figure2.2. The fields obey Maxwell's equations in free space outside the wire. The resulting electric and magnetic field can be expressed in spherical coordinates as shown in equation 2.1 and 2.2 [18]:

$$\boldsymbol{E_\theta} = \frac{I_0 d}{2\pi}\eta\left(\frac{1}{r}-\frac{j}{kr^2}\right)\frac{e^{-jkr}}{r}\cos\theta\hat{\boldsymbol{r}} + \frac{I_0\Delta z j\omega\mu}{4\pi}\left[1+\frac{1}{jkr}-\frac{1}{(kr)^2}\right]\frac{e^{-jkr}}{r}\sin\theta\hat{\boldsymbol{\theta}} \tag{2.1}$$

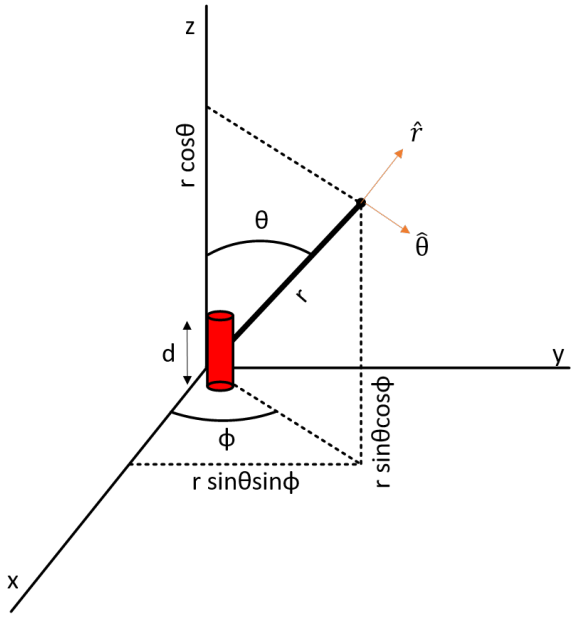

Figure 2.2: Figure showing the small antenna placed at the center of the coordinate, oriented towards the z-direction

$$H_\phi == \frac{I_0 d}{4\pi} jk\left(1+\frac{1}{jkr}\right)\frac{e^{-jkr}}{r}\sin\theta\hat{\phi} \tag{2.2}$$

Where,
d=size of the Hertzian dipole,
μ_0=magnetic permeability of free space,
I_0=current,
c_0=speed of light in free space,
r= the radial distance from the origin,
k_0=wavenumber.

Given the radial dependence of the radiated field components, two approximations can be applied to fields defined near to the radiating antenna, and fields that can be considered far from the radiating source. Many theories have different ways to define the near field and far-field of an antenna. In most cases, the distance $\gg 2D^2/\lambda$ is considered to be far-field. Where D is the longest dimension of the antenna, the length or diameter [19]. Alternatively, it can be thought of in this way, in the far-field region, the waves have a spherical wave-front whereas, in the near field this assumption is not valid, which can also be seen by figure 2.3. The electric field in these two regions is described in the following sections.

Near field

In the near field, $(k_0 r) \ll 1$ and (exp)jk$_0 r \sim 1$. Where k_0 is the wavenumber in free space and r is the distance of a point in free space from the antenna. Using these assumptions,the electric and magnetic fields reduce to equations 2.3 and 2.4.

$$\vec{E}(r,\theta,t) = \frac{Qd}{\epsilon_0 4\pi r^3}\left(2cos\theta\hat{r} + sin\theta\hat{\theta}\right) \tag{2.3}$$

$$\vec{H}(r,\theta,t) \simeq \hat{\phi}\frac{\mu_0 Qd}{\epsilon 4\pi r^2} sin\theta \tag{2.4}$$

It is seen that in the near-field region, the radiated electric field has a radial component as well.

Far field

In the far field region, the assumptions taken are $k_0 r \gg 1$ and $(exp)jk_0 r$ is no longer equal to 1. The electric and magnetic field can be described by Equations 2.5 and 2.6.

$$\vec{E}(r,\theta,t) = j\frac{\mu_0 \omega I_0 d}{4\pi} sin\theta\left(\frac{e^{-jk_0 r}}{r}\right)\hat{\theta} \tag{2.5}$$

$$\vec{H}(r,\theta,t) = j\frac{\mu_0 \omega I_0 d}{4\pi c_0} sin\theta \left(\frac{e^{-jk_0 r}}{r}\right)\hat{\phi} \tag{2.6}$$

They show a property of propagating electromagnetic waves with spherical waterfronts. The radially directed component are negligible when considering fields from the far field region . The detailed analysis of the far field approximation can be found in the work of [20]. The relation shown in Equation 2.7 also stands.

$$|\vec{E}| = |\vec{H}|\eta_0 \tag{2.7}$$

Where η_0 is the impedance of free space ~ 377 Ω. This analysis shows that in the far-field, we can assume that there is no radial component of the electrical field observed. Therefore, the magnitude of the electric field can be written as shown in Equation 2.8.

$$|E| = \sqrt{|E_\theta|^2 + |E_\phi|^2} \tag{2.8}$$

Figure 2.3 shows the difference in the near filed and far field regions.

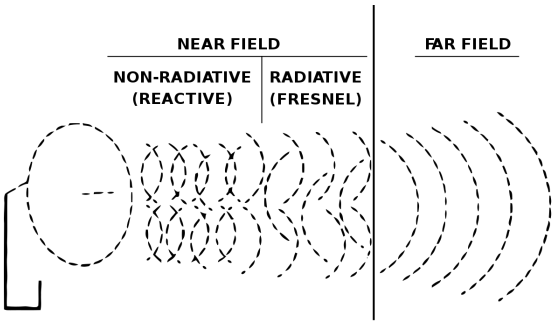

Figure 2.3: Image showing the difference of electromagnetic waves in the near field and far field.[19]

2.1.2. Radiated Power

The Poyntinmg vector is the measure of the directional energy of an electromagnetic field. Calculating the Poynting vector(Power Density) S, as shown in Equations 2.9.

$$\vec{S} = \epsilon_0 c_0^2 \vec{E} \times \vec{H} \tag{2.9}$$

The above equation can be integrated over θ and ϕ to find the total radiated power as shown in Equations 2.10.

$$P_{tot} = \int_0^{2\pi} d\phi \int_0^{\pi} r^2 sin\theta \langle S(\theta,\phi)\rangle d\theta \tag{2.10}$$

Which results in the total power radiated by the Hertzian dipole as shown in Equation 2.11:

$$P_{tot} = \frac{\pi \mu_0 c_0 I_0^2}{3}\frac{d^2}{\lambda^2} \tag{2.11}$$

This shows that the radiated power is a function of the currents on the antenna and the dimensions of the antenna.

2.1.3. Radiation patterns

The radiation pattern refers to the directional dependence of the strength of the radiated fields from the antenna. The radiation pattern is drawn to depict the electric/magnetic field or other related quantities. The distance of the plot from the origin is proportional to the magnitude of the quantity being considered. They can be plotted in polar and Cartesian coordinates. It can be seen from equations 2.5 and 2.6 that, for a constant r, the fields are proportional to $\sin\theta$, whereas equation 2.10 shows that for a constant r, the power is proportional to $\sin^{\theta}$. This shows that the field amplitudes and power density for a Hertzian dipole will show directional dependence. This can be seen in the radiation pattern for the Hertzian and dipole antennas. Figure 2.4 shows the radiation pattern in polar and Cartesian coordinates for a dipole antenna oriented in the z-axis.

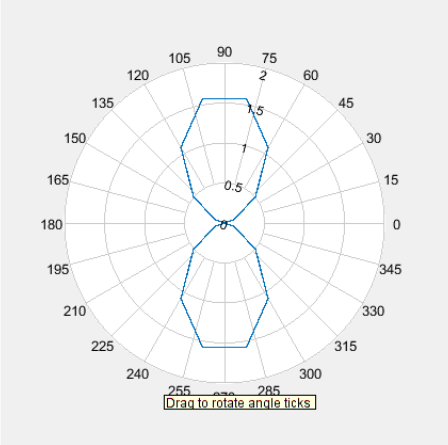

(a) The gain of a dipole antenna in polar coordinates with varying theta

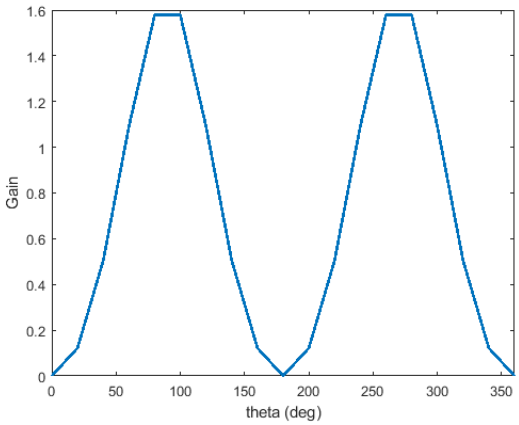

(b) The gain of a dipole antenna in polar coordinates with varying theta

Figure 2.4: The gain of a dipole antenna in polar and Cartesian coordinates with varying theta

2.1.4. Radiation Intensity

In the far-field region, the radiation intensity is the power per unit solid angle in a given direction. It can be expressed as shown in Equation 2.12:

$$U(\theta,\phi) = \frac{r^2}{2\eta}\left[|E_\theta(\theta,\phi)|^2 + |E_\phi(\theta,\phi)|^2\right] \tag{2.12}$$

The total radiated power power can be found by integrating the radiation intensity over a full sphere. Therefore the radiation intensity of an isotropic source (i.e. radiating equally in all directions) would be as shown in Equation 2.13:

$$U_0 = \frac{P_{rad}}{4\pi} \tag{2.13}$$

2.1.5. Directivity

The directivity of an antenna is defined as the ratio of radiation intensity in a particular direction to the radiation intensity averaged over all directions [21]. Equation 2.14 shows the directivity in terms of radiation intensity and radiated power.

$$D(\theta,\phi) = \frac{U(\theta,\phi)}{U_0} = \frac{4\pi U(\theta,\phi)}{P_{rad}} \tag{2.14}$$

Table 2.1 lists typical directivity of some common antennas.

Table 2.1: Table showing typical directivity values for different kind of antennas

Antenna Type	Typical Directivity	Typical Directivity (dB)
Short Dipole Antenna	1.5	1.76
Half-Wave Dipole Antenna	1.64	2.15
Patch (Microstrip) Antenna	3.2-6.3	5-8
Horn Antenna	10-100	10-20
Dish Antenna	10-10,000	10-40

It can be seen from table 2.1, that dipole and monopole antennas have the lowest directivity amongst the other antennas. In terms of radio astronomy, this is a beneficial parameter, as this would help to have an all-sky view irrespective of the orientation of the cubesat with respect to the source. This might not be the case if a directive antenna is considered such as a horn antenna, as the cubesat will have to change its orientation to align the antenna towards the source to make observations. Also, cubesats do not carry any propellants which can help in controlling their orientation, therefore antennas with low directivity are preferred.

2.1.6. Gain

The gain of the antenna is defined as the ratio of radiation intensity in a particular direction and the radiation intensity that would be obtained when the antenna is radiating isotropically. It is expressed in Equation 4.3.3.

$$G(\theta,\phi) = \frac{4\pi U(\theta,\phi)}{P_{in}} \tag{2.15}$$

The equation for gain is similar to the equation for directivity, apart from the fact that instead of radiated power, input power is considered. According to IEEE standards [22], the definition of gain does not consider mismatch and transmission line losses. Therefore, the gain of the antenna can be expressed in terms of the directivity as shown in Equation 2.16:

$$G(\theta,\phi) = eD(\theta,\phi) \tag{2.16}$$

Where, e is the efficiency of the antenna.

2.1.7. Effective aperture area

Effective aperture area of the antenna is the ratio of the power at the antenna ports to the flux density of a plane wave incident at the antenna which is matched to its polarization. Mathematically, it can be expressed as shown in Equation 2.17:

$$A_e(\theta,\phi) = \frac{P_A}{W_i(\theta,\phi)} \tag{2.17}$$

Where,
A_e=effective aperture in m^2,
P_A=power delivered from source to load in W,
W_i=Power flux density of the incident wave in W/m^2.

The effective aperture in terms of gain of the antenna is given by equation 2.18

$$A_e(\theta,\phi) = \frac{\lambda^2 G(\theta,\phi)}{4\pi} \tag{2.18}$$

Where G is the gain of the antenna.

2.1.8. Impedance

The input impedance of the antenna can be written as sown in Equation 2.19:

$$Z_A = R_A + jX_A \tag{2.19}$$

Where,
R_A=resistance of the antenna,
X_A=Reactance of the antenna.

The resistance of the antenna consists of two parts the radiation resistance and loss resistance as shown in Equation 2.20:

$$R_A = R_r + R_{loss} \tag{2.20}$$

Where,
R_r=radiation resistance (Ω),
R_{loss}=loss resistance (Ω).
As per IEEE, the radiation resistance is defined as the ratio of the radiated power to the square of rms current referred to a specific point [21] as shown in equation Equation 2.21. The loss resistance is the resistance due to finite conductivity or energy loss.

$$R_r = \eta\frac{2\pi}{3}\left(\frac{d}{\lambda}\right)^2 \tag{2.21}$$

Where,
η=Impedance of free space,
d=length of short dipole
λ=wavelength

As the Hertzian dipole's length is much smaller than the wavelength λ, the impedance of a Hertzian dipole would be much smaller to 377 Ω. The antenna can be represented as a Thevenin equivalent circuit, with an impedance and a voltage source. Using the efficiency equation 2.22, the efficiency of the antenna can also be expressed as shown in Equation 2.22:

$$Efficiency = \frac{R_r}{R_r + R_{loss}} \tag{2.22}$$

Figure 2.5 shows how the real part of the impedance can be divided into parts, radiation resistance and loss resistance. Where,

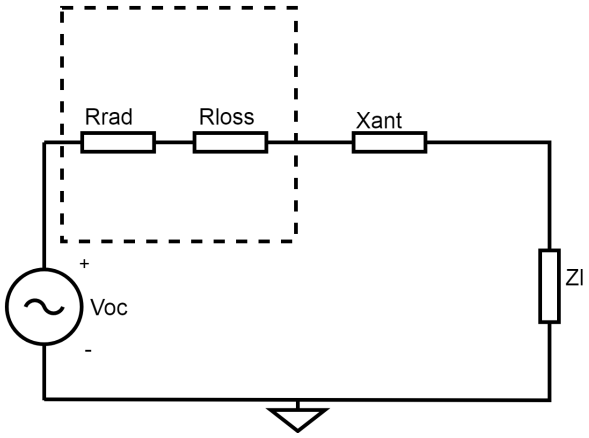

Figure 2.5: Model of the antenna with the radiation resistance and loss resistance.

Voc= Open circuit voltage,
R_{rad}=radiation resistance of antenna (Ω),
R_{loss}=loss resistance of antenna (Ω),
Z_l=load impedance.
To find the efficiency of the antenna, two simulations are used. The first simulation is done using a real world material (with losses), aluminium in this case, to find the radiation resistance R_r. To find the loss resistance, a the same simulation is done using a perfect electric conductor as the material. The loss resistance R_loss is given by equation 2.23

$$R_{loss} = R_{pec} - R_{alu} \tag{2.23}$$

Figure 2.6 compares the radiation efficiency of three different length dipoles. It can be seen that the length of the antenna has an effect on the efficiency of the antenna at low frequencies. Longer antennas tend to have higher efficiencies at low frequencies, which serves as a motivation to choose longer antennas.

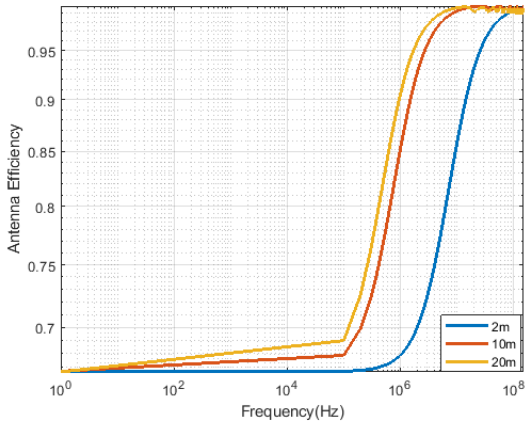

Figure 2.6: Image comparing the efficiency of dipole of three different length with respect to frequency

2.1.9. Open circuit Voltage

The open-circuit voltage of an antenna is defined as the voltage induced between the antenna terminals when they are open circuit. Assume that an incident electric field (E_{inci}) is incident on an antenna, of which the electrical model is shown in figure 2.5. The spectral flux density is given by equation 2.24.

$$S_{inci} = E_{inci} H = \frac{|E^2|}{Z_0} \tag{2.24}$$

The available power by the antenna is given by equation 2.25

$$P_{received} = S_{inci} A_{eff} \tag{2.25}$$

Where A_{eff} is the effective aperture of the antenna given by the equation 2.18. Therefore the power received from the antenna can be written as shown in equation 2.26

$$P_{received} = \frac{E_{inci}^2 \lambda^2 G(\theta,\phi)}{4\pi Z_0} \tag{2.26}$$

It is given by Equation 2.27:

$$Voc = \frac{\sqrt{R_{ant} G(\theta,\phi)}\lambda}{2\sqrt{\pi Z_0}} E_{inci} \tag{2.27}$$

Where,
R_a=real part of the antenna impedance.
$G(\theta,\phi)$=directive gain of the antenna in the direction of the incident electromagnetic wave,
λ=wavelength,
E_{inci}=electric field strength of the incident wave,
Z_0=impedance of free space.
Using the equation 2.27 above, the effective length of the antenna in meters can be found by Equation 2.28.

$$\frac{Voc}{E_{inci}} = l_e = \frac{\sqrt{R_{ant} G(\theta,\phi)}\lambda}{2\sqrt{\pi Z_0}} \tag{2.28}$$

The open-circuit voltage and the length of the antenna depend on the real part of the impedance of the antenna. This helps us in the design of the rest of the analog chain as it serves as the basis of conversion of flux density into a voltage at the input of the amplifier. The effective length of the antenna is directly related to the amount of open-circuit voltage that will be generated by the antenna. Therefore a longer antenna can convert the electric field into a larger voltage compared to a shorter antenna.

2.2. Half wave dipole

A half-wave dipole is an antenna whose length is half of the wavelength and is made by placing two conductors end to end with a small feed gap between them as shown in figure 2.7. The current distribution in a half-wave dipole can be expressed by Equation 2.29:

$$I(z) = I_0 \left(e^{i\omega t} cos kz \right) \tag{2.29}$$

Where,
k=$2\pi/\lambda$
and z is from -$\lambda/4$ to $\lambda/4$.
The electric field for a Hertzain dipole of length d from Figure 2.2 is used. Each element of length dz is radiating a field given by Equation 2.30:

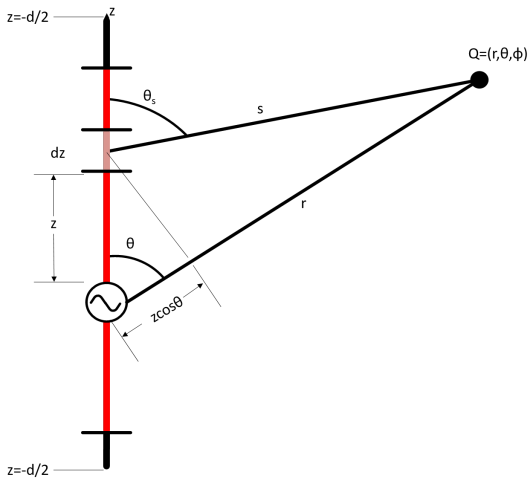

Figure 2.7: Figure showing the concept of integration of small Hertzian dipoles to compute characteristics of a half wave dipole.

$$d\vec{E}_\theta = j\frac{jk\eta_0}{4\pi}\vec{I}_z dz\left(\frac{e^{-jks}}{s}\right)sin\theta \tag{2.30}$$

This field can be integrating over the length to find the field for the entire dipole:

$$\tilde{E}_\theta = \int_{-\lambda/4}^{\lambda/4} d\tilde{E}_\theta \tag{2.31}$$

Which results in:

$$\tilde{E}_\theta = j\eta I_0\left(\frac{cos\left[(\pi/2)cos\theta\right]}{sin\theta}\right)\frac{e^{-jkr}}{2} \tag{2.32}$$

The flux density can written as:

$$S(r,\theta) = \frac{\left|\tilde{E}_\theta\right|^2}{2\eta_0} \tag{2.33}$$

It can be seen that the radiation pattern of this dipole would be similar to that of the Hertzian dipole by comparing equation 2.32 to equation 2.5.

2.2.1. Current distribution

The current distribution on a dipole antenna changes according to the wavelength of the incident wave. This affects the radiation pattern of the antenna. This allows us to characterize the antenna with varying the incident frequency and studying its current distribution. The varying current distribution and the radiation pattern with increasing wavelength are shown in figure 2.8.

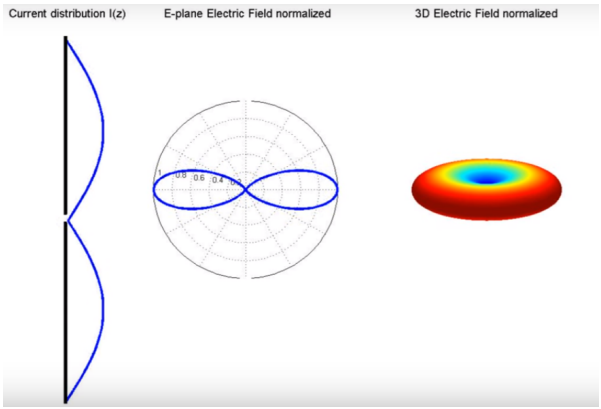

(a) Figure showing the current distribution ona dipole antenna with its polar and radiation pattern for 0.3λ

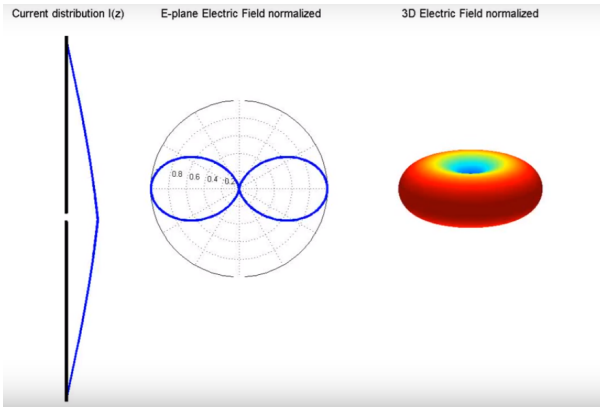

(b) Figure showing the current distribution ona dipole antenna with its polar and radiation pattern for 1λ

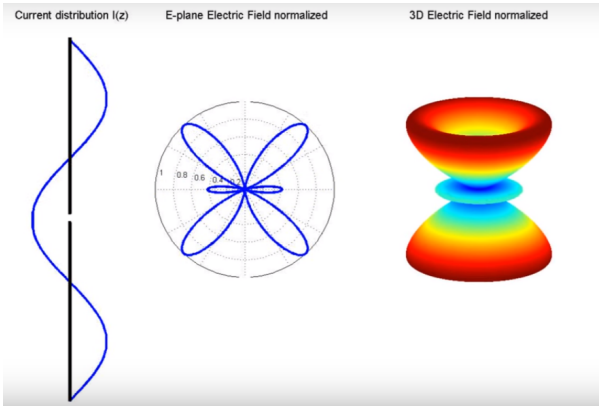

(c) Figure showing the current distribution ona dipole antenna with its polar and radiation pattern for 1.5λ

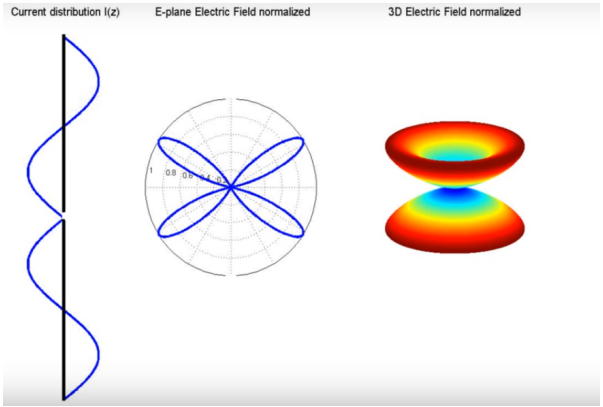

(d) Figure showing the current distribution on a dipole antenna with its polar and radiation pattern for 2λ

Figure 2.8: Comparison of skynoise levels to the receiver noise requirements

It can be seen from image 2.8, that with an increasing wavelength of the incident wavelength with respect to the antenna, the current distribution on the antenna changes, which has a direct effect on the radiation pattern of the antenna. In the case of wide-band designs, these effects need to be characterized to properly calibrate the instrument. Similarly, the current distribution of the monopole antenna over a perfect ground plane can be found out using image theory, which is discussed in the next section.

2.3. Image theory

Image theory can be used to analyze the behavior of antennas over a ground plane. Antennas can be designed to make use of an infinite ground plane. The concept is described in this section.

Imagine a dipole antenna placed vertically over an infinite, perfectly conducting ground plane as shown in Figure 2.9, represented by P and P'. Using boundary conditions a virtual dipole is formed and shown in figure 2.9. This virtual dipole is called an image of the dipole. As the ground plane doesn't need to be in the far fields, all the electric fields have to be considered, which is shown in equation 2.1. This equation can be condensed in Equation 2.34:

$$E = Ccos\theta\hat{r} + Dsin\theta\hat{\theta} \tag{2.34}$$

The radial component of the upper dipole is written as shown shown in Equation 2.35 and 2.36 :

$$E_{r1} = Ccos\theta_1 \tag{2.35}$$

$$E_{r2} = Ccos\theta_2 \tag{2.36}$$

When we look at the radial components of the virtual dipole at the bottom, the magnitude and distance factor, represented by C, remain constant as they are equidistant from a point along the plane that was previ-

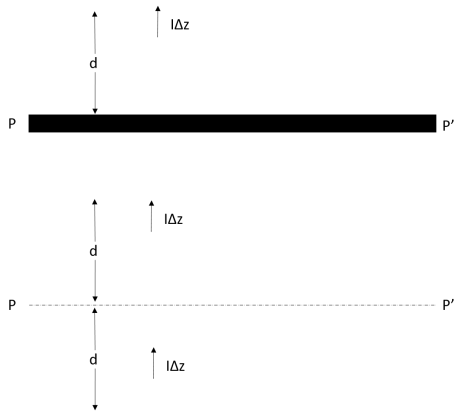

Figure 2.9: Image showing the application of image theory on a dipole antenna.

ously the ground plane. This leads to Equation 2.37:

$$\theta_1 + \theta_2 = 180^0 \tag{2.37}$$

through which we can conclude:

$$E_{r1} = -E_{r2} \tag{2.38}$$

If we draw the resulting vectors, the dipoles produce tangential electric fields along the plane that cancels out. Therefore, they satisfy the boundary condition of a PEC being present at the location.
For the $\vec{\theta}$ component, it can be shown that along the boundary, the following conditions hold:

$$\sin\theta_1 = \sin\theta_2 \tag{2.39}$$

The tangential components of the electric fields also cancel out. This analysis can be summarised as the resulting fields above a perfect conducting infinite ground plane can be found by summing the fields of the primary source above the ground plane and its image below the ground as if they were acting in free space.

2.3.1. Effects of the finite ground plane on the monopole antenna

As per the above analysis, the electric field can be calculated above the ground plane by using image theory. But that is not the case in a cubesat environment. There is not only an infinite ground plane present, but the size of the existing ground plane is also quite small. The ground plane would be the chassis of the cubesat which would serve as the ground terminal for all the electrical subsystems of the cubesat. The effects of a finite ground plane on the behavior of the monopole antenna have been shown in previous work [23][24][25]. The size of the ground plane directly affects the impedance of the antenna which is needed to match the analog chain for better noise performance of the system. Figure 2.10 shows the effect of changing the ground plane sizes. As the size of the ground plane is changing, the impedance of the antenna is also changing. This needs to be taken into account while designing the analog chain if only monopole antennas are chosen.

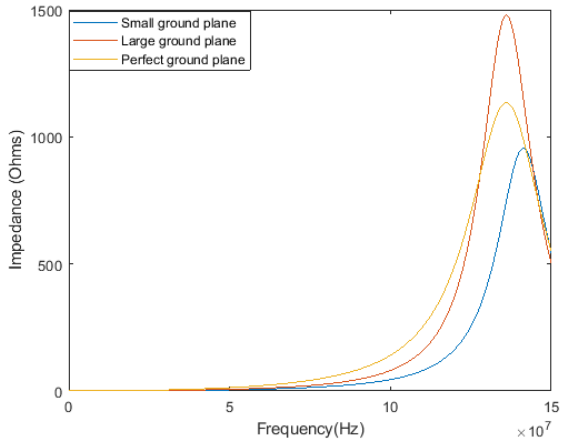

Figure 2.10: Image showing the effects of the size of the ground plane on the impedance of the monopole antenna

It can be seen from the image 2.10 that the impedance is varied by almost 400-500 /$Omega$ when a small or large plane is considered. The radiation pattern of the monopole antenna also changes due to the size of the ground plane. It can be seen in Figure 2.11. The first figure has a 1 m antenna with a 1 m^2 ground plane, compared to a 1 unit m with a 3 m^2 ground plane.

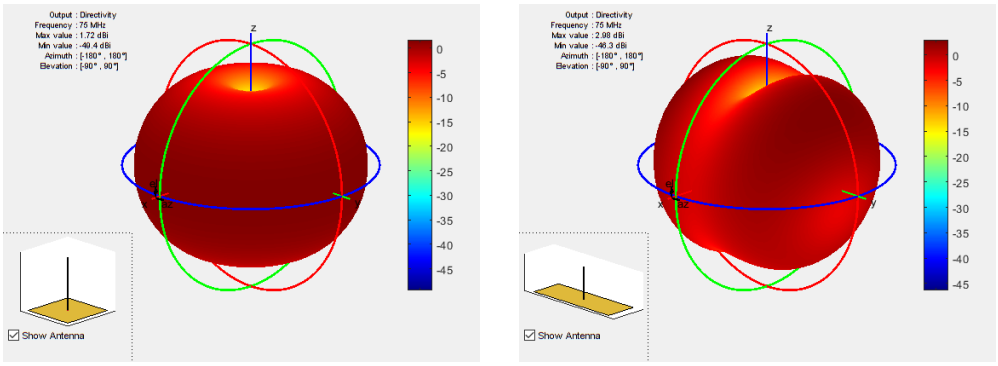

(a) radiation pattern of a monopole antenna over a ground plane of $1m^2$

(b) Radiation pattern of a monopole antenna with a rectangular ground plane of $3m^2$

Figure 2.11: Figure showing the effect of ground plane area on the radiation pattern of monopole antennas.

The dependence of radiation pattern on the size of the ground, to a certain extent, can be reduced by deferentially combining two opposing monopoles into a dipole.

It can be seen that monopole antennas can be analyzed similarly as the dipole antennas only if an infinite ground plane is present. In satellite environments where the length of the antenna is much longer compared to the body of the cubesat and also the chassis of the cubesat acts as a return path for all the currents, it cannot be considered to an ideal ground plane. Therefore, this starts to affect the radiation pattern and the impedance of the monopole antenna. It may be possible to characterize this behavior but this issue can be easily solved by the use of dipole antennas as they do not require a ground plane. Each arm of the dipole is referenced to each and therefore the effects of the ground plane are minimized. There is one way to solve the issue of ground planes with monopoles, that is is to convert the signals from two monopoles into a dipole antenna either in the analog domain itself or in the digital domain. This option is not considered as it increases the number of channels and the ADC in the analog chain and also doubles the number of amplifiers used.

2.4. Simulations

The antenna parameters were simulated in Altair FEKO. The cubesat in its entirety is difficult to model, therefore the structure of the cubesat was simplified and modeled as a 3U cuebsat with a thickness of 5 mm. A

model of an SMA connector was constructed to simulate the effect of a connector that would connect the antenna to the electrical system inside the cubesat. A hole was made on each face of the cubesat to not short circuit the antenna with the body of the cuebsat. The antenna ports were made between the antenna chassis of the cubesat through the SMA connector.

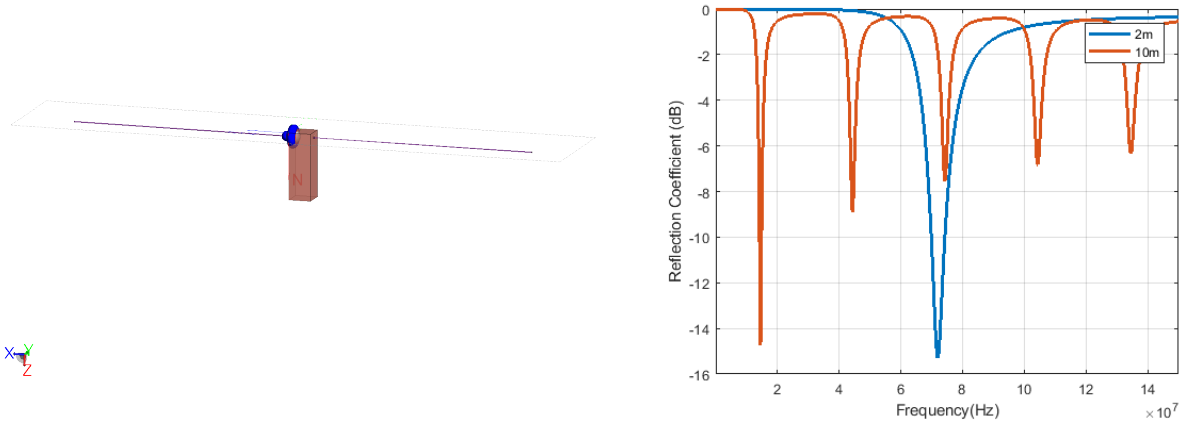

(a) Figure showing the simulation model of the antenna with the body of the cubesat

(b) S parameters of a 2m and 10m tip to tip dipole antenna

Figure 2.12: Figure showing the simulation model of the antenna with the cubesat body and the reflection coefficient of a 2m and 10m tip to tip dipole antenna

It is seen from figure 2.12, that the S-parameters of the two antennas are as expected. It can be seen from [26] that the effect of the cubesat body and feed gap point has a negligible effect on the performance of the antennas. Therefore the body of the cubesat does not affect the behavior of the antenna in the band of interest. This model can be further used to find the impedance and polarization behavior for different configurations of antennas.

2.5. Polarimeter

Polarimetry is an instrument that measures the polarization of an electromagnetic wave. Polarimetry is used for observation of various science objectives such as synchrotron emissions, Zeeman splitting, and Faraday rotation. The information can be represented in various forms of vectors. The Jones vector describes the amplitude and phase of the observed signal components, whereas the stokes vector describes the overall polarization characteristics of the signal. Thus in general cases, the Jones vector is used when describing the receiver system and the Stokes equation is used to know more about the physical characteristics of the source [27]. The Jones and the stoke vectors carry the same information and are linked to each other with some transformations.

The Jones vectors describe the polarization state of the wave, and contains two amplitudes:

$$E = \begin{bmatrix} E_x \\ E_y \end{bmatrix} = E_x \begin{bmatrix} 1 \\ E_y/E_x \end{bmatrix} \tag{2.40}$$

For example, a single electromagnetic wave can be represented by the Jones matrix given by:

$$\vec{E} = \begin{pmatrix} E_x \\ E_y \end{pmatrix} = \begin{pmatrix} \hat{E}_x e^{i(kz-\omega t+\phi_x)} \\ \hat{E}_y e^{i(kz-\omega t+\phi_y)} \end{pmatrix} = \begin{pmatrix} \hat{E}_x \\ \hat{E}_y e^{i\Delta\phi_{xy}} \end{pmatrix} \tag{2.41}$$

For its applications in radio astronomy, we assume that the source is a point source in the sky of a quasi-monochromatic and is a fixed point source in the sky. If the propagation is in the z-direction, the signal e can be represented by equation 2.42.

$$e = \begin{bmatrix} e_x \\ e_y \end{bmatrix} \tag{2.42}$$

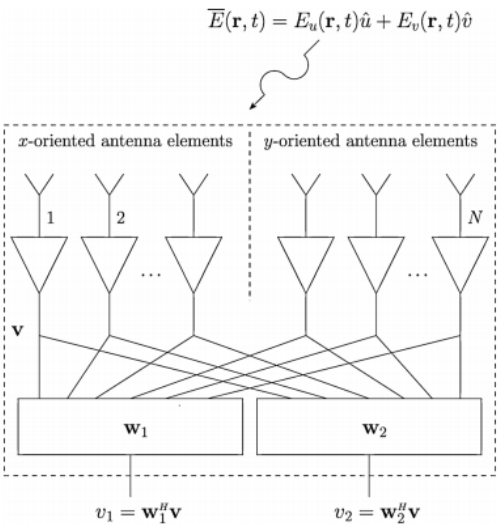

Figure 2.13: Figure showing the image of a polarimeter with x and y oriented antennas.

The assumption here is that all transformations along the signal path are linear. Therefore all linear transformations can be represented by equation 2.43.

$$e^{'} = Je \tag{2.43}$$

Where, J is the Jones matrix. Further assuming that there are two receiving feeds with two antennas a and b. The voltages generated at the end of the feed are linear to e. Therefore the relationship is given by equation 2.44.

$$v = \begin{bmatrix} V_a \\ V_b \end{bmatrix} = Je \tag{2.44}$$

Where J is the Jones matrix which the relation between the voltages at the terminal of the antenna and takes in to account all the propogation effect from the source including the antenna. These parameter are used to compare the polarization response of different antenna configurations with a cubesat. The next section describes the method used to compare the intrinsic cross polarization ratio of three different antenna configurations.

Figure 2.13from [28] shows the image of a polarimeter formed by x and y oriented antennas with active beamforming. Therefore the polarization information can be fully reconstructed by extracting data received from two orthogonal polarisations.

2.6. Intrinsic Cross Polarization Ratio

It is a relatively new concept introduced in 2011 [29], to introduce a new figure of merit for polarimeters. It is defined independently of a coordinate system. The IXR of the antenna or antenna configuration can is given by Equation 2.45

$$IXR = \left(\frac{\kappa(J)+1}{\kappa(J)-1}\right)^2 \tag{2.45}$$

Where,
J=Jones matix of the polarimeter,
κ=condition number of the Jones matrix.

2.6.1. IXR of Antenna configuration

The choice between a monopole and a dipole antenna can be made based on IXR of a preferred configuration of the antennas. As the satellite orientation may not be controlled in real-time, the antenna configuration should provide a good polarization response to minimize the effect of the orientation of the satellite. Using monopoles, the best way to cover all the polarization is to have three monopoles at adjacent faces on the cubesat. Whereas with dipoles, three dipoles across each face of the cubesat would cover all the polarization.

A study is done to compare data between a "tri-monopole", cross dipole and a "tri-dipole" configuration as shown in Figure 2.14, 2.15 and 2.16.

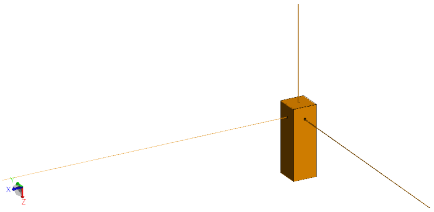

Figure 2.14: The "tri-monopole" configuration of antennas with the cubesat used for IXR comparison

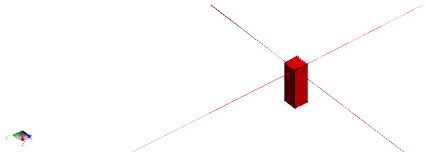

Figure 2.15: The "cross-dipole" configuration of antennas with the cubesat used for IXR comparison

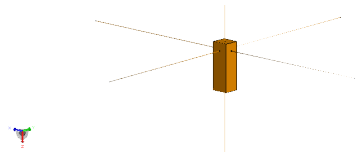

Figure 2.16: The "tri-dipole" configuration of antennas with the cubesat used for IXR comparison

The IXR were compared for antennas of 5m each, and for three frequencies:80 kHz, 1 MHz and 80 MHz so as to cover the entire range of the bandwidth of interest.

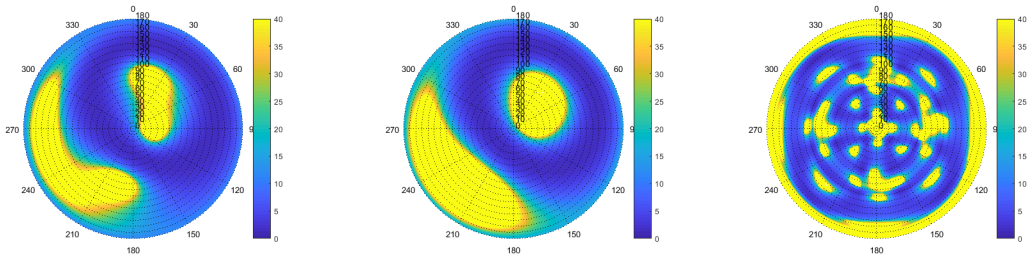

Figures showing the IXR at (a)80kHz (b)1 MHz (c)80 MHz for "tri-monopole" configuration.

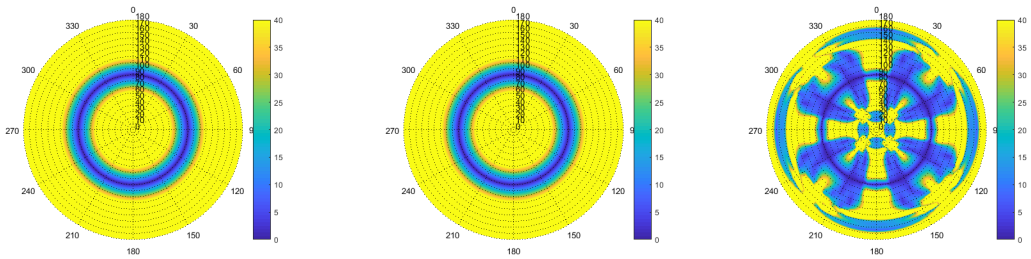

Figures showing the IXR at (a)80kHz (b)1 MHz (c)80 MHz for cross dipole configuration.

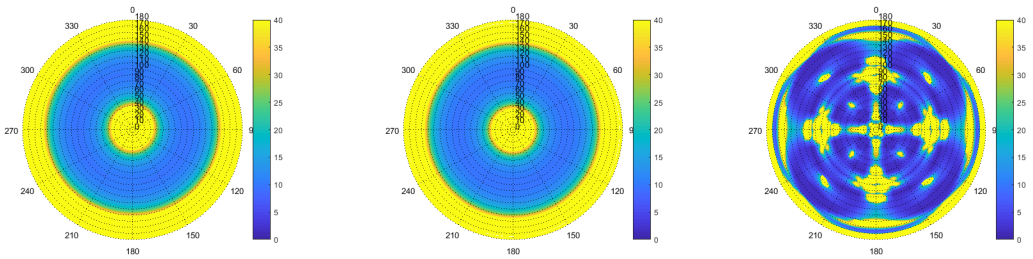

Figures showing the IXR at (a)80kHz (b)1 MHz (c)80 MHz for "tri-dipole" configuration.

As IXR plots are difficult to interpret visually, Table 2.2 showing the values of 40^{th} percentile values of IXR for the three different configurations of antenna.

Table 2.2: Table showing the 40 percentile IXR for three types of antenna, "tri-monopole",cross dipole and "tri-dipole".

Frequency	"Tri-Monopole"	Cross-Dipole	Tripole
80 kHz	16.5306 dB	23.04 dB	24.38 dB
1 MHz	17.59 dB	22.7260 dB	23.62 dB
80 MHz	18.47 dB	6.525 dB	15.41 dB

As seen from table 2.2, the IXR values for three configurations are similar at low frequencies, but the values for the cross dipole decrease drastically at high frequencies. The reason could be that the cross dipole is meant to detect only two orthogonal polarization, whereas the other two configurations would be detecting all the polarization. But as the reduction is only seen at those high frequencies, the cross dipole is chosen as it reduces the number of channels required and provides similar IXR at low frequencies as compared to the "tri-monopole" or "tri-dipole" configuration.

2.7. Conclusions

The choice of the antenna can be taken based on various considerations. As per the requirements, antennas with low directivity are required to reduce the dependence on the orientation of the cuebsat. Monopoles and dipoles are such antennas which have omnidirectional radiation pattern and are not very directive as shown in table 2.1. Therefore, they have a larger sky view compared to other directive antennas. But further, the choice between the two can be made by comparing the polarization response of the two configurations. As shown in section 2.6.1, the IXR response of the "tri-dipole" antenna configuration is the best over the frequency. But the increase in performance that can be achieved by adding another channel for the third dipole setup is not much when compared to the cross-dipole setup. Therefore, a cross dipole setup can be chosen if the power budget is not met. By analyzing these parameters, the cross dipole antenna configuration is selected. The power consumption and the number of ADC channels are also reduced by using two cross dipoles instead of 3 dipoles as it reduces the number of total channels. The only variable left to decide is the length of the antenna, which is chosen in the section 4.2.1 according to the noise budget for the amplifier. These points are summarised in the table below:

Table 2.3: Table comparing the two antenna configurations considered based on various parameters

Parameter	Tri-monopole	Cross dipole
Radiation pattern	-	+
IXR	-	++
Power Consumption	-	+
ADC channel	-	+
Antenna elements	+	-

3

RFI Consideration and Measurements

Electro-Magnetic Interference (EMI) in general is disturbance generated by natural or man-made sources that affect the functionality of electronic systems. These signals are mostly detrimental to the system. Radiofrequency interference (RFI) is a subset of EMI noise, which occurs in the radio frequency spectrum. The two terms are usually used interchangeably. This interference can affect the performance of the system in the form of introducing non-linearity in the system due to the introduction of high-level signals and intermodulations. Therefore, they need to be characterized during the design phase itself. For this work, RFI is considered to be the interference that originates from the local satellite subsystems, whereas EMI is the interference that is caused due to the environment, other surrounding satellites or man-made noise.

In the case of radio astronomy, this interference can be more harmful, if these signals are in the far-field region. It would become very difficult to differentiate them from the signals being received from an astronomical source. EMI can be broadly divided into two types, radiated and conducted emissions. In simple terms, radiated emissions are propagated through the air, away from the radiative source. Conductive emissions are caused due to stray currents which are usually generated either due to the development of a potential difference between two reference planes in circuits or a difference in the current in the hot and return path. This chapter discusses the sources of interference and its effect on the performance of the system if the standards are not met. Measurement results of interference tests are also shown.

3.1. Sources of RFI

In space, there can be various sources of interference and can be divided into natural and self-generated interference. Natural sources such as lighting, plasma, etc are not predictable and therefore circuit protection elements such as diodes or varistors are used to protect against these phenomenons. These are short and high power phenomenons, which can permanently damage the system if correct protection techniques are not used. This is not to be mixed up with the effects of radiation, which also contains a separate subset of single-event upsets and some of the prevention techniques overlap. Whereas the noise sources from the satellite itself, can be characterized to some extent and therefore are under the control of the designer. Subsystems such as power supply units, onboard computers, telemetry subsystem, satellite bus, and clock generators generate radiated emissions. All of these have some sort of switching circuits in them that produce a time-varying signal or can couple to traces on the board or other signal paths. It has been identified that the power supply unit is one of the major sources of interference and therefore has been considered for the characterization of RFI.

3.1.1. Main source of RFI

To identify the RFI sources and their corresponding effects on the system, a basic block diagram of the system is shown in figure 3.1:

The power supply unit usually contains an MPPT (Maximum Power Point Tracking) module, which transfers the maximum available power from the solar panels using a control loop. This control loop contains DC-DC converters which switch at various frequencies, causing radiated emissions. The on-board computer

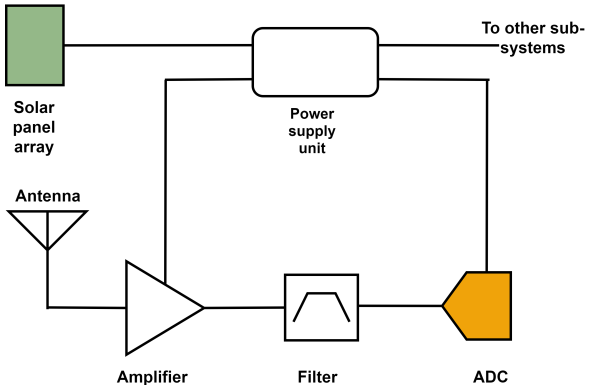

Figure 3.1: System level block diagram of the analog chain with the power supply unit and the solar panels

also causes radiated emissions due to switching and clock circuitry[30]. To investigate further, the block diagram of a typical power management system is shown in figure 3.2

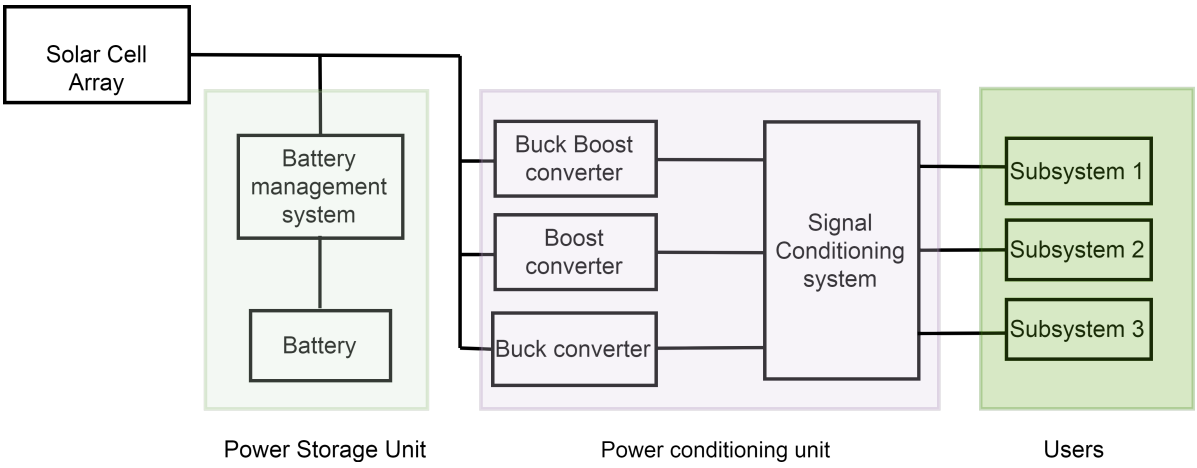

Figure 3.2: Block diagram of a typical power supply unit in cubesats

DC-DC converters are used to supply a set DC power to the system. They are efficient, low cost and are compact systems due to which are used in space missions. As seen from figure 3.2, various sub-systems may use different supply voltages that make use of different DC-DC converters and therefore different switching frequencies. This adds to the radiated emissions.

3.2. Coupling mechanism of RFI

The issues with RFI can be broken down by dividing the system into three sections, the source, coupling path, and the receiver. As discussed in the previous section 3.1.1, DC-DC converters have been identified as a major source of RFI and hence it acts as a source of emissions. The path can be described as the ways this source can affect the system and enter the signal chain. There are three paths through which the signal can enter the signal chain in this case, which are shown in figure 3.3. The receiver is the element through which the interference of the system, which in this case are is the antenna and the power supply line.

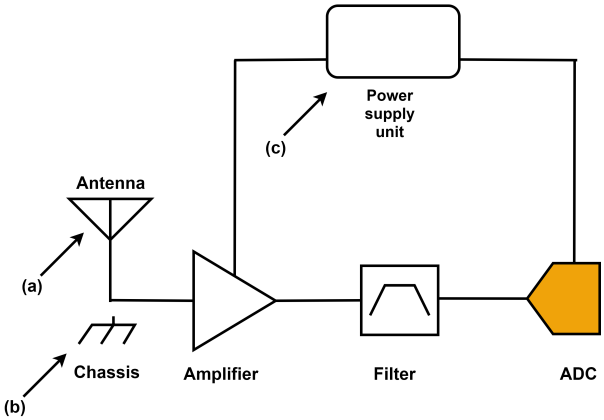

Figure 3.3: The image shows three coupling paths for RFI to enter the system chain. Path (a) shows that the emissions can couple with the antenna and enter the signal chain. Path (b) shows the path through which stray currents can enter the system due to a potential difference between two reference nodes. Path (c) shows the power supply path through which RFI can couple into the system

Figure 3.3 shows the three mechanisms through which interference can enter the signal chain and affect the instrument. The first path (a) shows the coupling through the antenna, which causes emissions to enter the signal chain. If this level is too high, it becomes very difficult to distinguish between the interference and signal from the source. The second path (b) shows the coupling of stray currents caused due to a difference in potential between two reference nodes, which can cause stray currents on the chassis of the cubesat. There can also be emissions due to a difference in the hot and return path of current. The third path (c) shows the coupling of interference through the supply line to the subsystems.

3.3. Effects of RFI

This interference can introduce non-linearity in the systems if their levels are high. As they can also couple with the power supply path, they also put requirements on the power supply rejection ratio. Due to the coupling with the antenna, they also put a requirement on the common-mode rejection ratio of the system.

3.3.1. Power supply rejection ratio

The power supply rejection ratio is defined as the ratio between the change in power supply voltage change to the voltage required at the input to nullify its effect at the output [31] as shown in 3.1.

$$PSRR = \frac{V_p}{V_{id}} \tag{3.1}$$

Where V_p is the change in power supply voltage and V_{id} is the differential input voltage.

3.3.2. Common mode rejection ratio

The common-mode rejection is defined as the ratio of the differential gain of the system to the common mode gain of the system as shown in equation 5.3.3 from [31].

$$CMRR = \frac{A_{dm}}{A_{cd}} = \frac{\frac{V_o d}{Vid}}{\frac{V_{od}}{V_c}} \tag{3.2}$$

Where, A_{dm} is the differential gain and A_{cd} is the common-mode gain. It can be seen that the common-mode gain should be as small as possible to have a high common-mode rejection ratio. The interference can have a differential and a common mode component. If the common-mode component of the interference is high, it may drive the amplifier into saturation, therefore it is necessary to have a high common-mode rejection ratio. There are certain ways to reduce the effect of common-mode interference during the design such as having a fully differential architecture and galvanic isolation between grounding paths.

3.3.3. Linearity

Subsystems such as communication and power supply unit, radiate high levels of interference which can affect the functionality of the analog receiver chain as the signals can couple to the signal chain and cause the

amplifier to saturate and cause and cause clipping distortion. There are several methods to mitigate these effects which include filtering of signals outside the band of interest for the communication subsystem and also using filtering for the power supply unit. The dynamic range of the amplifier should include a margin for the case where the interference levels are higher than that of the maximum signal to be received from the source.

3.4. Calculation of RFI

The limits for radiated and conducted emissions are set by different agencies for different applications. We focus on the requirements provided by MIL-STD 461 C, which provide a limit on narrow-band and broadband interference for both conducted and radiated emissions [32]. The following sections show the allowed levels of conducted and radiated emissions according to the science objective requirements.

3.4.1. Radiated emissions

To calculate the levels of RFI needed, we look at the signal levels coming from various bodies and phenomena in space. The galactic background noise as discussed in chapter one is assumed to be an isotropic noise

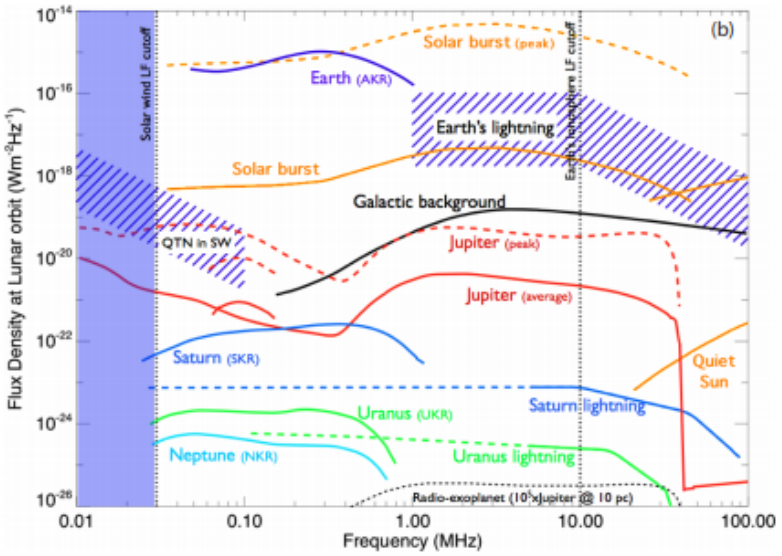

Figure 3.4: Spectral noise flux densities of signals from various bodies and phenomena in space

source and is considered to be a reference value. We can convert the spectral noise flux densities into an electric field using equation[33]:

$$E = \sqrt{SZ_0\Delta f} \tag{3.3}$$

Where,
E=electric field in V/m,
S=Spectral noise flux density in $W/m^2/Hz$,
Z_0=Impedance of free space(377 Ω),
Δ f = bandwidth of observation in Hz.
Therefore, the electric field equivalent of the sky noise can be found by assuming a bandwidth of 1 Hz. Any instrument that is outside the cubesat, and produces RFI will couple directly to the antenna. The resulting signal should not mask the galactic background signal. If the external instrument's radiated emissions are below the values shown in figure 3.5, then the system will not be RFI limited. For instruments inside the cubesat coupling with the antenna, the levels can be around 40dB higher as the body of the cubesat chassis can provide around 40dB of suppression. The values for internal and external instruments with the allowed MIL-STD-461C radiated emission are shown in figure 3.5.

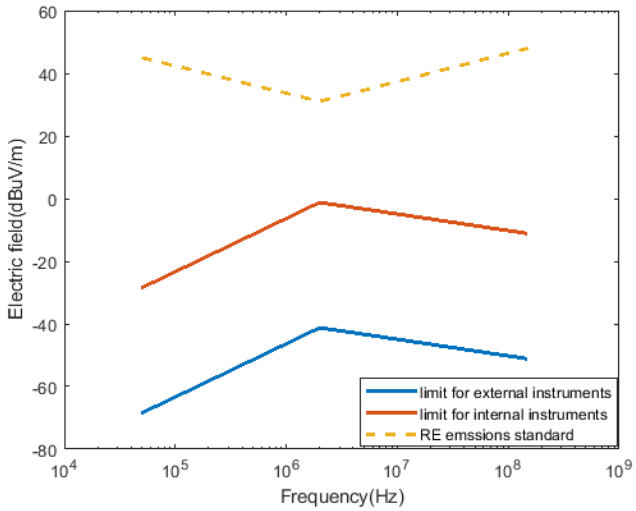

Figure 3.5: The maximum allowed radiated fields inside and outside the system in comparison to the maximum field allowed set by MIL-STD-461C

3.4.2. Conducted emissions

The chassis of the cubesat is used as a ground terminal for all the electronic systems. Therefore the return currents flow on the surface of the cubesat. Any change in the supply and the return currents can give rise to a potential difference between the two panels of the cubesat. This would change the ground potential and therefore reducing the dynamic range of the system if the system is referred to the ground in the case of a monopole antenna or a single-ended system. Assume a case of a single-ended amplifier, if the ground potential is zero or the same as that of the antenna reference, the amplifier input will have the maximum dynamic range. But in the case where the potential of antenna reference ground and amplifier ground is changed, the amplifier input will not have a maximum dynamic range anymore. Therefore, it is necessary to asses the levels of currents and designs the signal chain such that the effects can be minimized. The allowed current limit should not produce a potential on any panel greater than the voltage produced by the galactic background signal to retain the maximum dynamic range of the system. This can only be assessed if the maximum impedance difference between the two panels of the cubesat is known. This is difficult to calculate and is usually found by measurements on a fully integrated system as the calculated and the measured values have been found to vary by a factor of 10-100. Therefore, by assuming an impedance difference of 1Ω, the values of the current limits are found and are shown in figure 3.6 , where it is compared to the MIL-STD-461C current limit.

Using the signals in radio astronomy and the MIL-STD461C, levels have been defined for the internal and external instruments for radiated and conducted emissions. It can be seen from figure 3.5 that the limit for external instruments is already around 30dBuV/m lower than the allowed limit, which is difficult to attain in the real-world systems. The chassis of the cubesat provides extra shielding, therefore, the limit on internal instruments is relaxed. Whereas for conducted emissions, the results have only been shown for an impedance difference of 1Ω, which are already much lower than the standard limit. Therefore looking at these levels, it would be difficult to meet these specifications in practical design, therefore, the analog chain needs to be designed considering that the set levels are not met and the emissions can be as high as the MIL-STD limit.

3.5. Measurements

As described in section 3.1, the MPPT module serves as the power control block which is housed inside the cubesat. The point where the wires connect the solar cell array to the power subsystem inside the cubesat is a susceptible site for RFI emissions. Ideally, the current on the HOT and the return wire should be equal, canceling the radiated RFI by the respective paths, as the directions of the currents would be the opposite. But in the real world, due to mismatch or losses, the two currents may not be the same and give rise to emissions. The worst-case scenario would be when an instrument outside the cubesat generates RFI above the permitted level which couples through the antennas and enters the signal chain or the current has a long return path creating ground loops. To test this and measure the level of RFI, measurements were conducted.

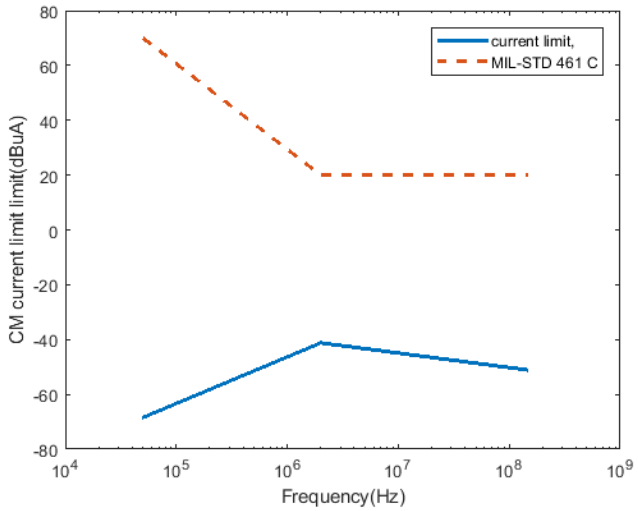

Figure 3.6: The CM current limit in comparison to the MIL-STD-461C standards.

The block diagram is shown in figure 3.7

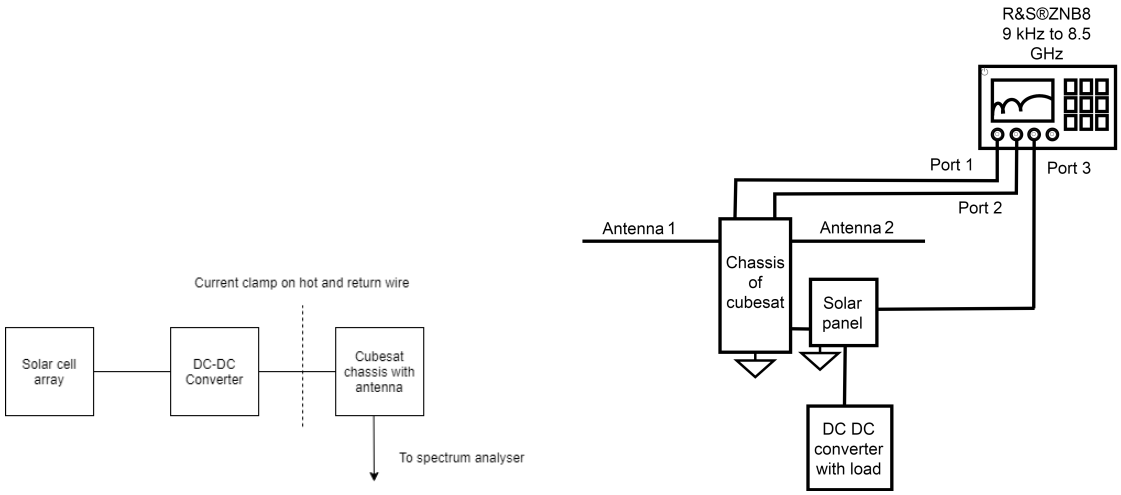

(a) Figure showing the block diagram showing the measurement setup for conducted emissions

(b) Measurement setup for radiated emissions and measurement of coupling between the antenna and the solar panels.

Figure 3.7: Figure showing the block diagram for conducted emissions test and the setup for measurements of radiated emissions.

3.5.1. Measurement setup

The aim is to find the open-circuit voltage of the antenna and convert it back to an E-field or noise power flux density to compare it to the galactic noise or limit found in the previous section. The differential and common mode currents would generate RFI and thus need to be measured on the two wires. A calibrated current clamp is used to determine the change in current, which can be translated to the open-circuit voltage of an antenna if the coupling between them is known for conducted emissions as shown in figure 3.8. The coupling is measured via a network analyzer by assigning a port on the solar panels and the antenna. Using equation 3.4 from the work of [34] the open circuit voltage for the antenna can be found.

$$V_{oc} = S_{ab}\left(\frac{\sqrt{Z_0 Z_L}}{2\sqrt{Re(Z_L)}}\right) J_p \tag{3.4}$$

Where,
V_{oc}=Open circuit voltage,

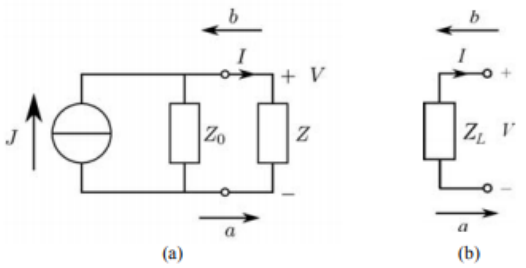

Figure 3.8: Image showing the schematic diagram of the solar panel as a current source and calculation of the open circuit voltage via the load impedance.

S_{ab}=S parameter between the two ports(Coupling),
Z_0==Impedance of the solar panel array equivalent current source impedance,
Z_L=Load impedance of the antenna,
J_p=Current measured by the current clamp on the hot and return wire.
A one-meter monopole was used as the antenna. A DC-DC converter was used to asses the radiated and conducted emission by them. No EMI filters or common-mode cokes were used to find the worst-case scenario. Figure 3.9 shows the open-circuit voltage produced on the antenna converted to an electric field and compared to the limits set in section 3.4.1.

For radiated emissions, the output is from the antennas are directly taken from the port of the antennas to a spectrum analyzer and then converted into a voltage over an impedance of 50Ω (impedance of spectrum analyzer).

Figure 3.9 shows the measured values for radiated and conducted emissions with respect to the maximum allowed emissions according to the science case and MIL-STD 461C. Both of the measured values seem to exceed the limit but the measurements were done without any sort of filtering from the DC-DC converters and absence of other subsystems. Therefore, the design of the analog receiver should take into account the interference from the common mode current which can couple into the system and reduce the dynamic range. Whereas for radiated emissions, when the converters are placed inside the cubesat, these levels are expected to drop significantly. Also shielding by isolating the power supply unit by enclosure in a metal box should be implemented to further reduce the effects of these emissions.

3.6. Mitigation of RFI

There are a few steps to mitigate RFI and its effects from the system. They are explained from a different frame of reference as follows:

- From source It is one of the easiest ways to mitigate RFI. If the emissions from the source are reduced, the effects will be reduced from the chain. For example, the emissions from the power supply unit can be mitigated by adding sufficient filtering. Common mode chokes and RFI filters are used. Another method is to ensure that the switching frequency can be outside the band of interest. The power can also be reduced from the source side which causes RFI.

- Coupling/path There are a few methods to reduce the coupling of emissions from the source to the receiver. The distance and position between the two can be changed to make sure that the coupling is reduced. The cables being used can be upgraded to be more EMI resilient by double braiding to improve the shielding of the signal. Apart from this, a shielding enclosure can be used to cover the source of interference as it reduces the propagation of emissions.

- From receiver The last step is to try to mitigate the effects of RFI is from the receiver side. As RFI has the most effect on the power supply rejection and common-mode rejection, these parameters should be made critical during the design phase. Other considerations such as using a differential topology for rejection of common-mode can be used. Galvanic isolation can be used to mitigate the effects of stray currents from entering the signal chain. As the levels of RFI can be quite high compared to the source signal, the dynamic range of the system should be increased.

Figure showing measured radiated emissions converted to an electric field and compared to the limit set and the MIL-STD-

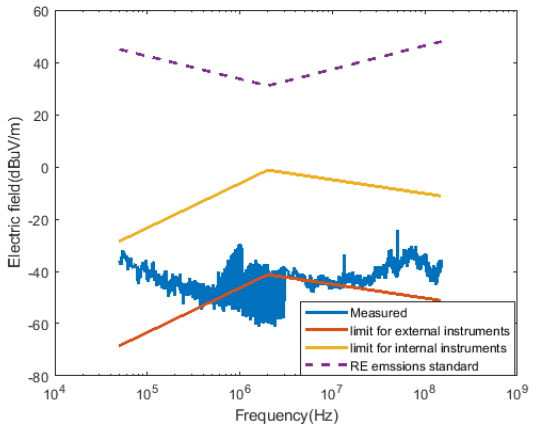

Figure 3.1(b) Measured current on the hot wire compared to limit set and MIL-STD-461C.

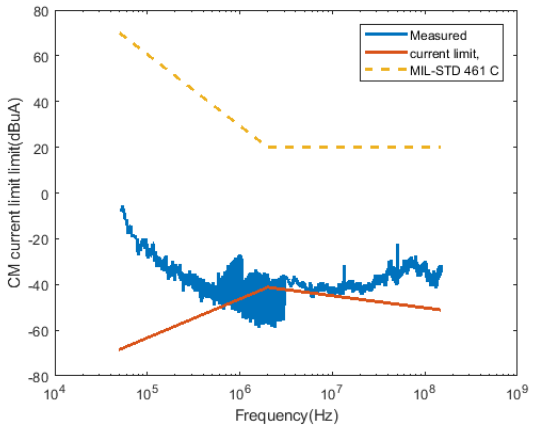

Figure 3.9: Figure showing measured radiated emissions converted to an electric field and compared to the limit set and the MIL-STD-461C standards. Figure 3.1(b) Measured current on the hot wire compared to limit set and MIL-STD-461C.

3.7. Conclusions

The requirements are set by using galactic background noise as a reference. Any RFI produced with a level greater than the background noise would mask the signal. Therefore, the level of the RFI generated by the cubesat should be below the level preferably for the entire band. The values are set for both radiated and conducted emissions as found for which the instrument would be sky noise limited. A small test is done to determine the emissions by the DC-DC converter alone. These are compared to the limits set by the standards. It was found that the DC-DC converter alone does produce enough RFI which can be detected by the antenna in an anechoic chamber and for the worst-case scenario, no filters or common mode chokes were used for the measurements. The DC-DC converter with ample filtering and common mode chokes can be made to adhere to the RFI levels. However, nothing can be predicted until tests are done on a fully assembled system.

4

System Design

In chapter 2, the design choices for the antenna were presented. It was concluded that the dipole antenna will be used for the target application. However, the length of the antenna was not decided. In the third chapter, the levels of RFI for radiated and conducted emissions were shown. In this chapter, we discuss the requirements and design of the analog receiver chain, which contains the antenna, and the amplifier, ending at the ADC.

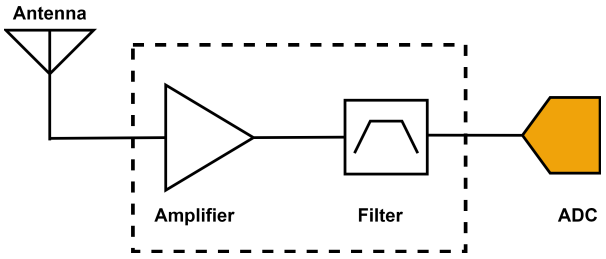

Figure 4.1: A block diagram of the analog receiver chain with the amplifier and the filter highlighted.

The chapter aims to derive the requirements for the analog chain after the antenna. To do so, the chapter starts with an explanation of the concept of noise temperatures and its relation to flux density and sensitivity of the system. Using the relation and the given requirement for the noise of the analog chain, various requirements such as the gain, linearity, dynamic range, input-referred noise, etc are found. Depending on the requirements, architecture, and implementation of the low noise amplifier and filter is also discussed. In the end, the final design is presented.

4.1. Concept of Noise Temperature

In general, noise temperature is a method of expressing the available noise power contributed by a source or component. The power spectral density of the noise is expressed in temperature that would produce the same level of Johnson noise [35].

$$P_n B = k_b T \tag{4.1}$$

Where,
P_n=Noise power (W),
B=Bandwidth (Hz),
k_b=Boltzmann's constant (J/k),
T=Noise Temperature (K)

Radio astronomy receivers contain a few basic blocks such as the antenna, amplifiers, filters, ADC, etc. All these elements contribute to the total noise of the receiver. The noise added can be of thermal or other noise generation mechanisms. All the contributions from various noise sources are lumped together and can

be described by a noise temperature T as given in equation 4.2.

$$T = \frac{P}{B}\frac{1}{k_b} \tag{4.2}$$

Using the concept of noise temperatures, the concept of brightness intensity and conversion of noise temperatures to flux density can be understood as these units are associated with the strength of the signal and sensitivity of the receiver in radio astronomy.

The spectral noise power flux density can be derived from the Rayleigh-Jeans approximation. The Plank law for black body radiation is given by equation 4.3.

$$B_\upsilon = \frac{2h\upsilon^3}{c^2}\frac{1}{e^{h\upsilon/kT}-1} \tag{4.3}$$

Where, B=Brightness intensity (W/m^2/Hz/rad^2),
h=Planck's constant,
υ= frequency (Hz),
k=Boltzman's constant (J/K),
T=Temperature (K).

For radio frequencies, Taylor expansion can be used to expand the term $e^{h\upsilon/kT}-1$ as it is often true that $h\upsilon \ll$ kT. This leads to the Rayleigh-Jeans approximation for black body radiation:

$$B_\upsilon = \frac{2kT}{\lambda^2} \tag{4.4}$$

Equation 4.4 is known as Rayleigh–Jeans law. It is seen that the intensity increases with reduction in frequency.
The flux desnity of a source with brightness B_υ subtending a small angle $\Omega \ll 1$ sr, is given by equation 4.5

$$S_\upsilon = B_\upsilon \Omega \tag{4.5}$$

These equations are used to transform various signal sources as described in section 1.4.2 can be converted from one domain to the other. The three important signals are shown in spectral noise flux density and noise temperature in figure 4.2.

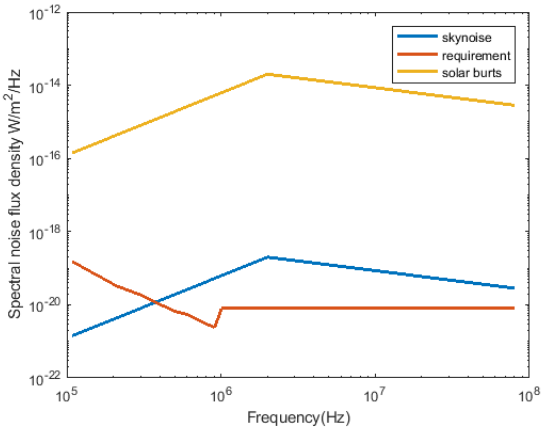

(a) Sky noise and requirements in spectral noise flux density

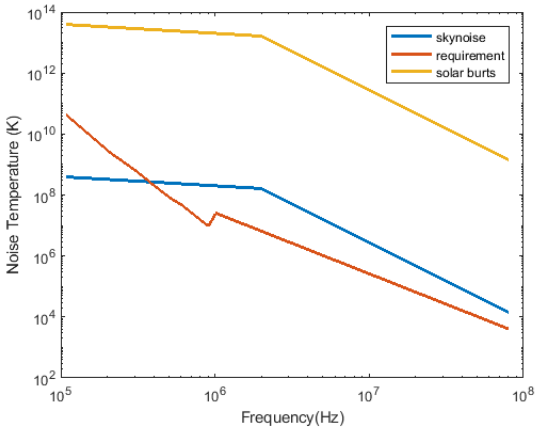

(b) Sky noise and requirements in noise temperatures

Figure 4.2: Comparison of skynoise levels to the receiver noise requirements

4.1.1. Measure of sensitivity

A common method of comparing sensitivity of radio astronomy receiver is by the comparison of the SEFD (System Equivalent Flux Density) of the system. It is the flux density for a given system noise temperature,

and is expressed as:

$$SEFD = \frac{2kT_{sys}}{A_e} \tag{4.6}$$

Where,
k=Boltzmann's constant (J/K),
T_{sys}= system noise temperature (K),
A_e=Effective area of the antenna.

It can be seen from equation 4.6 that the system noise temperature is directly proportional to the system sensitivity and therefore a lower system noise temperature is desired. In the next section, we look at the various components of the system noise temperature and use it to derive the requirements of the analog chain.

4.1.2. System Noise Temperature

The system temperature is the measure of noise in the system due to various factors including the antenna, surrounding and the receiver itself. The system noise temperature contributions are represented by equation 4.7 from [36]

$$T_{sys} = T_{sky} + T_{bg} + T_{spill} + T_{cal} + T_{rec} \tag{4.7}$$

Where,
T_{sys} = System noise temperature in Kelvin,
T_{sky} = Noise from radio background in K,
T_{bg} = Noise from atmosphere emissions in K,
T_{spill} = Noise from ground emissions in K,
T_{cal} = Noise from injected noise for calibration in K,
T_{rec} = Noise from the receiver in K.
Considering that the system has to be operated in space, noise contributions from T_{bg},T_{spill}, and T_{cal} are considered to be much lower than the level of the background noise and the receiver noise. Therefore, equation 4.7 can be reduced to the following expression:

$$T_{sys} = T_{sky} + T_{rec} \tag{4.8}$$

It can be seen from equation 4.8, that there can be two causes for the system temperature. If the receiver temperature is more than t_{sky}, the system will be receiver noise limited. Whereas, in the second case, if the noise temperature of the receiver is less than t_{sky}, the system will be sky noise limited. To keep the system sky noise limited, the noise contribution from the receiver needs to be lower than skynoise, which is the case as seen from figure 4.2.

4.1.3. Receiver Noise temperature

To find the noise contributions from the receiver, we need to find the noise sources and their contributions to the total receiver noise. Figure 4.4 shows a simplified block diagram of the analog chain used for analysis.

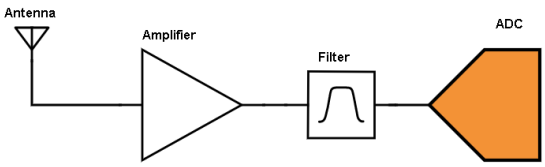

Figure 4.3: Figure showing a representation of the analog chain of the receiver.

The noise from the analog chain contributing to the receiver noise referred to the input of the receiver can be written using the Friis formula as:

$$T_{rx} = (T_{ant} + T_{LNA}) + \frac{T_{ADC}}{G} \tag{4.9}$$

Where,
T_{ant} = noise temperature contribution of the antenna including feed losses,

T_{LNA} = noise temperature contribution of the amplifier,
T_{ADC} = noise temperature contribution of the ADC.
G=Gain of the stage before the ADC.
Therefore, it can be seen that, to reduce the noise contribution from the ADC, gain is required before it.
The total system noise temperature can now be represented as:

$$T_{sys} = T_{sky} + T_{rec} \tag{4.10}$$

Assuming, that the noise contribution from the ADC has been reduced by adding a gain stage before it and is much lower compared to the noise contributions from the LNA and antenna. As the antenna and LNA are the two noise contributors in the receiver system, they are used to set limits on the noise budgets for the receiver.

4.2. Receiver noise analysis

In the last section, it was seen that the system noise temperature has two major contributors, skynoise temperature and receiver noise temperature. We have already discussed the levels of skynoise temperature, therefore in this section, we find the contribution of the receiver noise temperature. As seen in equation 4.10, the two contributions for system noise temperature are from the antenna and the receiver. Therefore we need to find the contributions from each of them. This is done by assuming two systems:

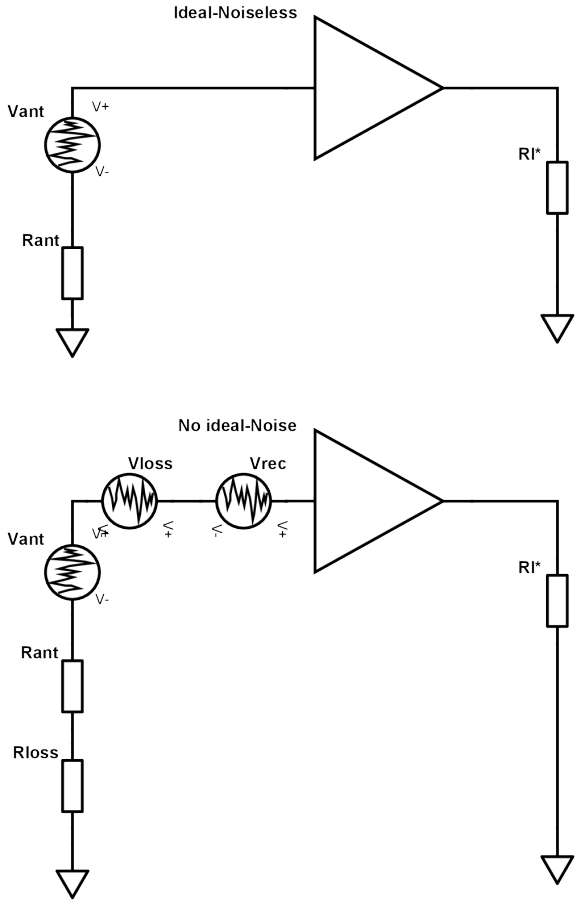

Figure 4.4: Two systems are considered for finding the individual noise temperature contributions. The first system is assumed to be ideal therefore it has a noise temperature of 1 K. Whereas, the second system is nonideal and all the noise sources are modeled at the input of the system.

- Ideal system: A system is assumed which contains the antenna and a receiver, and the noise temperature is 1. Therefore the noise from the antenna can be given by:

$$V_{ant} = \sqrt{4kR_{ant}} \tag{4.11}$$

V_{ant} is the noise contribution at the input of the amplifier due to the antenna. R_{ant} is the radiation resistance of the antenna as described in section 2.19 and as T=1.
The total output noise power at the output is given by:

$$V_{nonoise}^2 = 4kR_{ant}G_{av} \tag{4.12}$$

Where, G_{av} = Available power gain when the systems are conjugately,

- Non-Ideal system: A second system is assumed where the antenna losses are considered as well as the noise from the receiver is modeled. The noise in the system can be modeled as:

$$\begin{aligned} V_{ant} &= \sqrt{4kT_{sky}R_{rad}} \\ V_{loss} &= \sqrt{4kT_{amb}R_{loss}} \\ V_{rx} &= \sqrt{4kT_{rec}R_{ant}} \end{aligned} \tag{4.13}$$

Where,
T_{amb} is the ambient temperature in which the system is being used.
The total noise power at the output is given by:

$$V_{noise}^2 = (4kT_{sky}R_{rad} + 4kT_{amb}R_{loss} + 4kT_{rx}R_{ant})G_{av} \tag{4.14}$$

These systems are shown in figure 4.4.

Now the system noise temperature is found by using equation 4.12 and 4.14

$$T_{sys} = \frac{V_{noise}^2}{V_{nonoise}^2} \tag{4.15}$$

$$T_{sys} = \frac{(4kT_{sky}R_{rad} + 4kT_{amb}R_{loss} + 4kT_{rec}R_{ant})G_{av}}{4kR_{ant}G_{av}} \tag{4.16}$$

which leads to:

$$T_{sys} = T_{sky}\frac{R_{rad}}{R_{ant}} + T_{amb}\frac{R_{loss}}{R_{ant}} + T_{rec} \tag{4.17}$$

Using equation 2.22, we can express this as:

$$T_{sys} = T_{sky}(\eta) + T_{amb}(1-\eta) + T_{rec} \tag{4.18}$$

Where,
η =radiation efficiency of the antenna,
T_{amb}=Ambient temperature. Equation 4.18 shows that the system temperature is affected by the efficiency of the antenna and the receiver noise temperature. Therefore it is the combination of two which leads to the system sensitivity rather than just one of them. Therefore the design of the antenna and the amplifier are correlated and cannot be done independently of each other. The efficiency of different lengths of dipole antennas is shown in figure 2.6. Therefore the first two terms of the equation 4.18 can be calculated and the required noise temperature can be found.

Figure 4.5 shows the noise temperature contribution of the first two terms of the equation 4.18. The efficiency of the antenna affects both the terms in the equation, therefore it can be seen from the first graph that the length of the antenna does not majorly affect the sky noise temperature. But from the second graph, shows the noise contribution antenna due to the ambient temperature in which the antenna is operated. For simplicity, a standard temperature of 290 K is assumed, and it can be seen that the longer antenna contributes much lower compared to the short antennas. This is due to their increased efficiencies at low frequencies. This also serves as a motivation to choose a longer antenna.

We have looked into the first two terms that constitute the system noise temperature. To analyze the LNA noise temperature, we need to define the length of the antenna and convert the requirements to a voltage domain. This is done to make the analysis of amplifier architecture and topology easier as the specifications of all electronic devices are specified in the electrical domain. The next section is used to determine the length of the antenna based on the noise budget by the various lengths of antennas.

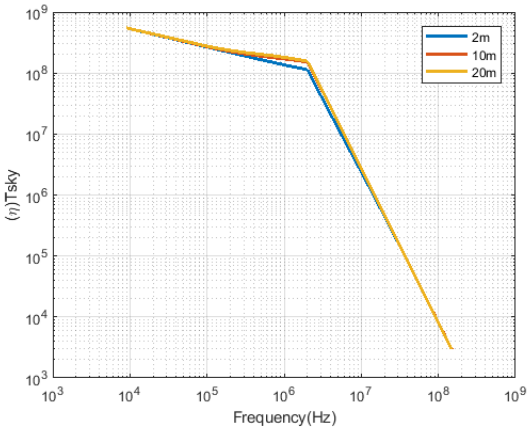

(a) Graph showing the first term of the equation with different length of antennas

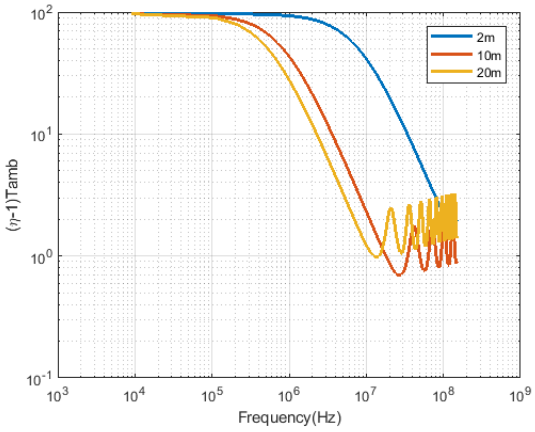

(b) Graph showing the second term of the equation with different length of antennas and ambient temperature of 290K.

Figure 4.5: Figure showing the effect of antenna efficiency on the system temperature which makes the first term of equation 4.18 and the effect of ambient temperature, taken as 290K, which is the second term in the same equation.

4.2.1. Noise budget and length of Antenna

To find the effects of the length of the antenna, we need to find the noise budget it provides for the rest of the analog chain. For this purpose, it is easier to look into the voltage domain as the specifications for the amplifiers are expressed in terms of voltages rather than flux densities. As the antenna converts the spectral flux density to an electrical signal, we can convert the receiver requirements given to convert it into a noise budget at the input of the amplifier. This helps to make design decisions regarding the topology, architecture technology, etc for the rest of the analog chain. Using the approach of structured electronic design, we can model all the noise sources from the amplifier as a voltage and current source at the input of the amplifier. Where,

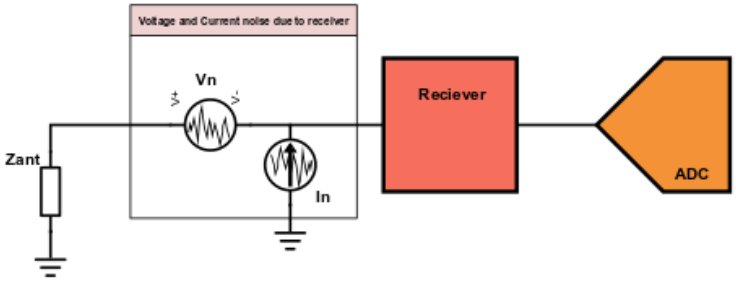

Figure 4.6: Figure showing the equivalent voltage and current sources modelled at the input of the analog chain of the receiver.

V_n=equivalent voltage noise density from the receiver,
I_n=equivalent current noise density from the receiver.

As shown in section 1.4, that the sky noise is assumed to an isotropic noise source, the required noise flux density is also assumed to be isotropic and therefore can be converted into a noise density at the input of the amplifier.
Using the equation 4.19, the spectral noise flux density can be converted into an electric field, which then can be converted into a voltage. When Δf as 1 Hz, we get the spectral voltage noise:

$$E = \sqrt{S_{\text{galactic background}} Z_o \Delta f} \tag{4.19}$$

Where, E is the electric field in (V/m), S is spectral noise flux density in $(W/m^2/Hz)$, Z_0 is the impedance of free space and Δ is the bandwidth of observation in Hz.

$$S_v = EL_e \tag{4.20}$$

Where,
l_e = Length of the antenna.
Different length antennas are considered to determine the voltage noise budget.

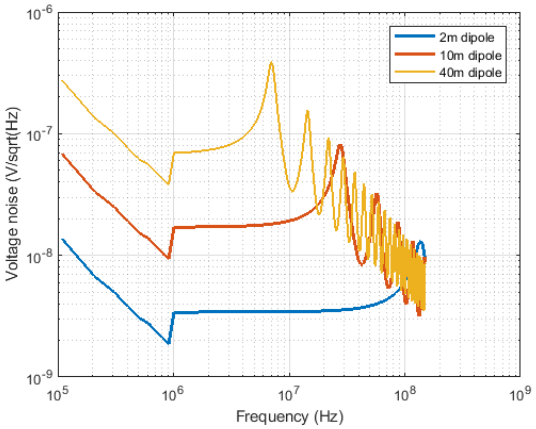

Figure 4.7: Graph showing the total noise budget for different antenna length

It can be seen in the figure that the benefit of using a long antenna directly affects the noise budgets. As the antenna length increases, the noise budget for the amplifier is also relaxed and therefore a trade-off has to be made between the length of the antenna, the sensitivity that the system can achieve. This can be made based on the type of device being used as there are certain practical limits in terms of noise that can be achieved by discrete technology.

The contributions from the efficiency of the antenna have been seen and it can be seen that longer antennas are better both in terms of efficiency and allowed noise budgets. The next section discusses the other requirements of the analog chain.

We have seen that the system noise temperature for the space-based system depends on the receiver noise temperature, which is due to the noise contributions from the antenna and the low noise amplifier. The noise from the ADC can be suppressed by using ample gain before the ADC. The effect of antenna efficiency on system noise temperature has also been seen, where antennas of different lengths were used to compare their noise contributions. Using the length of the antenna, the noise budget has been found which helps to make a design choice for the type of device to be used and the architecture of the amplifier. In the next section, other requirements for the analog chain are discussed.

4.3. Requirements

As the length of the antenna has been fixed, which also gives us the noise budget for the amplifier, other requirements for the analog chain need to be determined. This section uses the basic signals in radio astronomy explained in section 1.4 to define some of the requirements such as gain, linearity, dynamic range, etc.

4.3.1. Dynamic Range

Dynamic range is defined as the ratio of the maximum power of the signal to the noise power. The dynamic range of the system can be derived from the requirements of observing the solar flux and the galactic background noise. Figure 4.8 shows the highest level of the signal that needs to be detected (Solar flares). The lower level of the signal is defined by sky noise. This drives the requirement for the dynamic range of the receiver. The difference between the signals from solar bursts and skynoise is around 60dB as seen in figure 4.8. Therefore the minimum dynamic range should be 60dB to receive signals from the highest and lowest input signal. But there can be a case where the level of interference is even higher than the level of solar bursts as discussed in chapter 3.

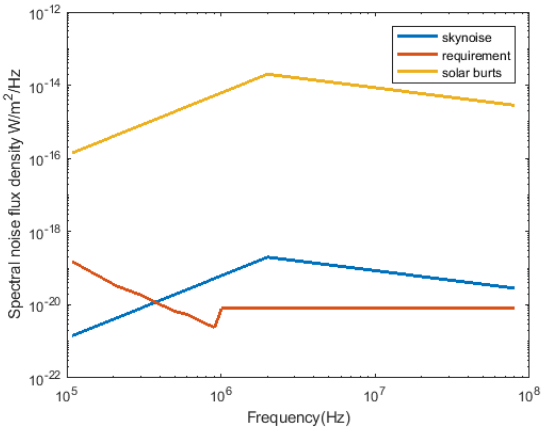

(a) spectral noise flux density of requirement, sky noise and solar flares.

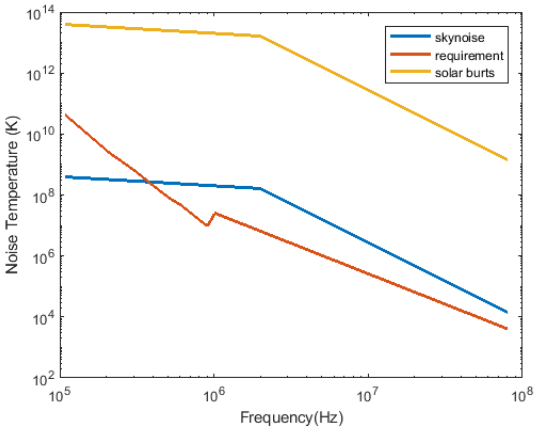

(b) Image comparing the noise temperature of sky noise, solar bursts.

Figure 4.8: Image comparing the spectral noise flux density and noise temperature of sky noise, solar bursts compared to the requirements for the analog receiver.

Figure 4.8 shows the spectral noise flux density and noise temperature of requirement, sky noise and solar flares. But as seen in the previous section 3.4.1, the level of MIL-STD461c is much higher than the equivalent emissions allowed for the instrument to be sky noise limited. Considering the case where the emission limits are not met and are near the limit of the allowed emissions, the radiated emissions would be higher than the level of solar flares as well. Therefore in the worst case, the requirement of dynamic range can increase drastically. Figure 4.9 shows the level of all the signals in a common unit, spectral noise flux density. Only the radiated emissions have been considered as the conducted emissions are difficult to predict. Therefore two

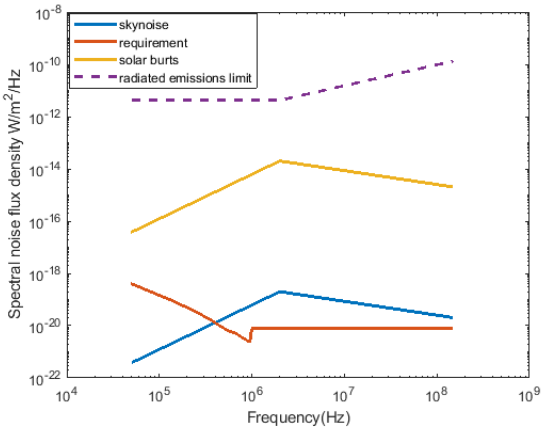

(a) [Image comparing the spectral noise density of sky noise, solar bursts and MIL-STD461C to determine the dynamic range.

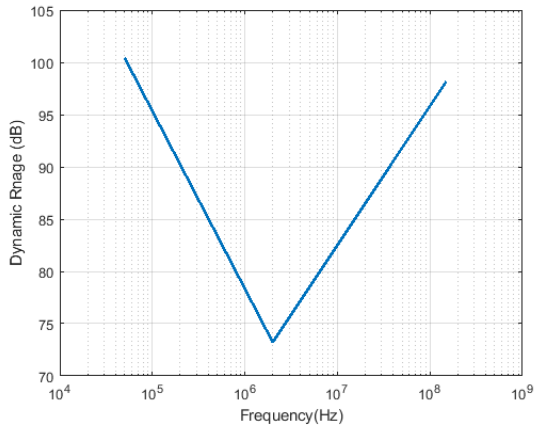

(b) Increase in dynamic range due to MIL-STD4 61C.

Figure 4.9: The dynamic range required in the case where RFI levels are higher than the level of solar bursts

cases for dynamic range can be considered. The first where solar bursts are the highest level of the signal that needs to be observed and RFI levels are under the standard value provided. In this case, the dynamic range of the system needs to be around 60dB as the difference in the level of the signal between skynoise and solar bursts is around that value. The second case is where RFI is the limiting factor and it dominates over solar bursts as the highest signal. In that case, the dynamic range can be as high as 100dB in some parts of the band such as low frequencies.

4.3.2. Linearity

The linearity of the system can be specified by several different methods such as Harmonic Distortion (HD), total harmonic distortion (THD) and intermodulation distortion (IMD). IMD gives a better performance evaluation of the receiver as it analyses the effect of multi-tones. As mentioned in chapter 3, there can be strong interference from the communication subsystem, power supply unit and the on-board computer. Therefore setting a requirement on the harmonic distortion needs to be defined. The distortion specifications are derived from the largest signal that is to be observed by the amplifier. In the case where the solar flares are the highest signal that will be observed, we would want the intermodulation products to be below the galactic background noise. As seen from Figure 4.8, the spectral noise flux density of solar flares is $\simeq$ 50dB higher than the sky noise limit. Therefore the harmonic distortion level should be at least 50dB lower than the signal power.

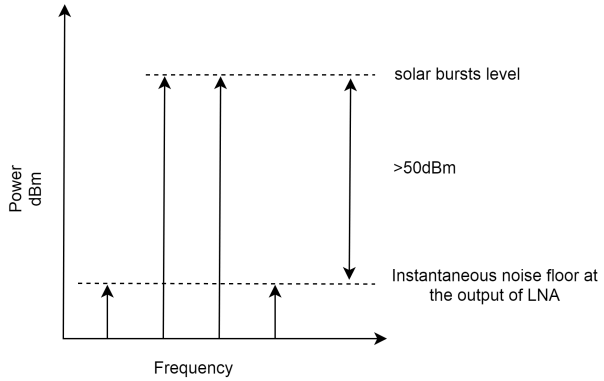

Figure 4.10: Image showing the linearity requirements assuming that the power from the solar flares are at 0dBm, the 3rd order intermodulations should be at least -50dBm lower.

Figure 4.10, shows the linearity requirements assuming the power from solar flares to be at 0dBm, the third-order intermodulation products, should be at least below -50dBm for them to be below the instantaneous noise floor of the amplifier output. In the worst-case scenario where the RFI limit is not met, the radiated emission is much higher than the level of solar flares, therefore the distortion specifications of the amplifier are much more stringent, in order of 90 dB-100 dB.
Intermodulation distortion also depends on the architecture being used by the amplifier. In a fully differential amplifier, the even-order harmonics would be canceled and only the odd-order harmonics would be seen. This is an advantage as the RFI levels are not fully defined, therefore we would want the intermodulation products to be lower than the sky noise as specified.

4.3.3. Gain

The gain of the system can be set by two constraints. The first constraint can be seen from equation 4.21, where the gain before the ADC stage determines the noise contribution from the ADC. Therefore the gain of the stage should be enough to suppress the noise of the ADC. The second consideration of gain is to utilize the entire dynamic range of the ADC.
To find the clip level for the ADC, the highest possible input signal power needs to be known. The highest signal according to the science case, is coming from solar bursts. The signal from a solar flare at the input of the amplifier can be found by converting spectral flux density to a voltage by the length of the antenna. Using the equation 4.19, solar bursts can be converted to a voltage at the input of the amplifier. Using the impedance of the ADC and the possible input peak to peak voltage, the highest possible gain for the amplifier can be found. Equation 4.21 finds the gain of the amplifier by converting the maximum peak to peak voltage to an rms and dividing it by the integrated maximum voltage.

$$\text{Gain} = 20\log\frac{\frac{V_{adc|pp}}{2\sqrt{2}}}{V_{input}} \tag{4.21}$$

The voltage at the input of the amplifier is integrated for the bandwidth of interest- 80 MHz. It is assumed that the ADC has an input voltage of $2V_{pp}$. This gives the value of gain to around 50dB.

As the voltage at the input of the amplifier is dependant on the length of the antenna being used, the value of gain also depends on the length that is chosen.

4.3.4. Bandwidth

The bandwidth required is from 80 kHz to 80 MHz. Filtering is required before the amplifier because the skynoise approaches high values at low frequencies. This may cause the amplifier to saturate if the low frequencies are not rejected. The short antenna will act as a first-order filter as the efficiencies at low frequencies reduce rapidly, thus the conversion of signal would automatically reduce as shown in figure 2.6. High power level signals from the communication or clock subsystems can couple to the antenna or signal traces, which can cause distortions and introduce nonlinearities in the amplifier. These high-frequency signals and need to be filtered out as well. Therefore filtering has been used before and after the first stage of the design.

Therefore the requirements can be summarised as shown in table 4.1.

Table 4.1: Table summarizing the requirements for the antenna and the analog chain

Parameter	Min	Typ.	Max	Unit
Dynamic Range	60	70	90	dB
IM2		50		dBm
Gain	30	40	60	dB
Bandwidth	0.08		80	MHz
Input referred noise (Depending on the length of antenna used)	1	10	40	nV/sqrt(Hz)
Polarization (Orthogonal)	2			

4.4. Amplifier Consideration

Using the requirements in the previous section, the design of the low noise amplifier will be implemented. As the application is wideband, and the input impedance (antenna) is not constant over frequency, the design of the amplifier is critical. The first design choice that needs to be made is between a single-ended or a differential system.

There are a few advantages in choosing a deferential topology over a single-ended topology. In a differential system, the even-order harmonics would be canceled, which is not the case in a single-ended system. A fully differential system is also inherently more immune to the common mode and external noise sources. It is also seen from section 2.3.1 that the impedance of monopole is susceptible to conducting ground planes, which is not the case in dipole antennas. Single-ended systems are referenced to the ground of the chassis which again can introduce noise into the system. The dynamic range of a differential system is 3dB higher than that of the single-ended systems. Single-ended systems would detect the common mode and differential mode signal, which is an advantage over the differential system. But in the case of strong RFI signals having a high common-mode component, the amplifier input range might not be enough. Wit single-ended systems, the number of ADC required would double compared to differential signals. Due to these reasons, a fully differential architecture has been chosen.

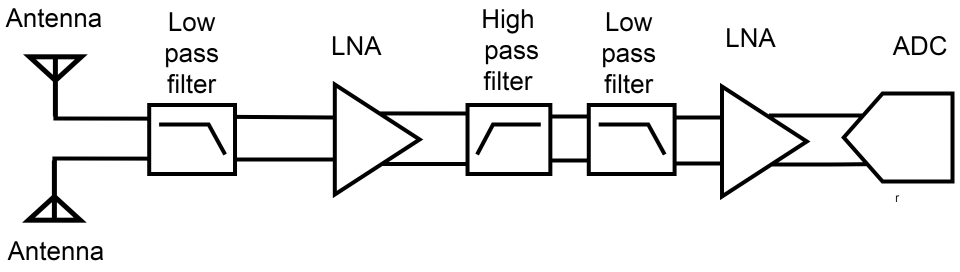

Figure 4.11: Block diagram of the fully differential topology chosen.

4.4.1. Device Choice

As the implementation is going to be done with op amps, we compare different technology op amps. Table 4.2 compares different specifications of different fully differential amplifiers. The Opamp THS4511 was chosen on the basis of higher gain bndwidth product, slew rate, and rail to rail capability. Another advantage of the

Table 4.2: Table comparing the various parameter for different opamps

Parameter	OPA818	OPA858	OPA859	THS4511	LMH5401
Technology	FET/CMOS Input	FET/CMOS Input	FET/CMOS Input	ADC driver(BJT)	ADC driver(BJT)
Architecture	Single Ended	Single Ended	Single Ended	Fully Differential	Fully Differential
Current per channel(mA)	27.7	20.5	12.1	39.2	55
Slew Rate (V/us)	1400	2000	1150	4900	17500
Voltage Noise (nV/rt(Hz)	2.2	2.5	3.3	2	1.25
Current noise @100 kHz (fA/rt(H))	20	8	8	2000	3000
Bandwidth (MHz)	790	1200	1800	1600	6200
Rail to Rail	no	no	no	In to V-	no
Available in radiation hardened package	no	no	no	yes	yes
Supply Voltage (V)	13	5.25	5.25	5.25	5.25
HD2 10 MHz ,100 MHz(dBc)	-64,:	-88,-64	-90,-60	-117,-64	-102,-98
HD3 10 MHz, 100 MHz (dBc)	-96,:	-86,-68	-86,-64	-106,-80	-102,-95

IC is that it is also available in radiation hardened package which increases the reliability of the system. The trade off here is that the current noise in BJT op amps is much higher at low frequencies. But due to high distortion requirements, we make the trade off towards a BJT implementation with slightly more noise. The gain required is high to reduce the noise contribution from the ADC, and due to the limited gain bandwidth of the op amp, two stage are used.

4.4.2. Noise analysis of topology

The amplifier is used in a very wideband, a simple resistive feedback topology is chosen. The various noise

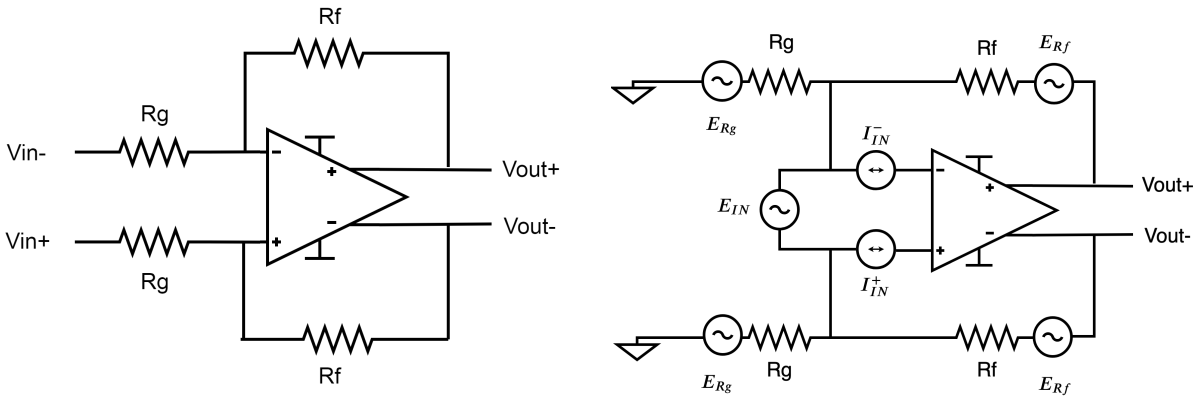

(a) Op-amp with resisitive feedback

(b) op-amp with resisitive feedback and equivalent noise sources

Figure 4.12: Figure depicting the amplifier topology and its equivalent noise sources.

sources can be translated to the output using the Equation 4.22

$$E_{od} = \sqrt{\frac{(2E_{in})^2 + (2I_{in}R_{eq})^2 + (2I_{in}R_{eq})^2 + [2(E_{Rg})(1-\beta)]^2 + [2(E_{Rg})(1-\beta)]^2}{(2\beta)^2} + E_{Rf}^2 + E_{Rf}^2} \tag{4.22}$$

Where,
E_{od} = differential output noise voltage,
E_{in} = equivalent noise voltage from the amplifier,
I_{in} = equivalent current voltage from the amplifier,
$\mathrm{R_{eq}} = \dfrac{R_g R_f}{R_g + R_f}$,
$\beta = \dfrac{R_g}{R_g + R_f}$,
$E_{\mathrm{Rf}} = \sqrt{4kTR_f}$,
$E_{\mathrm{Rg}} = \sqrt{4kTR_g}$.

The input-referred equivalent voltage noise can be found by dividing the total output referred noise by the gain of the amplifier.
Using flat band values for E_{in} and I_{in} from the datasheet, 3nV/$\sqrt{Hz}$ and 2pA/$\sqrt{Hz}$ respectively. The total noise from the opamp is 3.5nV/$\sqrt{Hz}$ which can be modeled as a voltage source at the input of the amplifier.
A second gain stage is used to provide more gain and reduce the noise of the ADC. The same architecture has been used with the same op-amp. The values for R_f are chosen to be 1825Ω and there are two ways to use R_g, the first is to place a 50 Ω resistor, or to use the characteristic impedance of the filter as R_g. For the second stage, the value for R_f has been chosen to be 1200Ω.

4.4.3. Filter design

As a fully differential architecture is chosen, the filter design becomes critical as the filters need to be balanced before the input of the amplifier. To reduce mismatch losses, the order of the filter should be chosen carefully as it would directly affect the response of the amplifier.
The cutoff frequency can be chosen to be a bit higher than 80 MHz to ensure minimum losses incur in the band of interest due to mismatches. A trade=off needs to be made between the fall off and the order of the filter. The main reason to use filters at the input of the amplifier is to filter out any high-frequency signals that might cause distortions. Signals from the communication, which can be high in amplitude can cause the amplifier to saturate if not suppressed enough.

The design of differential filters follows a simple methodology. A single-ended filter that meets the design requirements can be converted into a differential filter by folding and repeating the design across a ground terminal. The ground terminal can then be removed and the value of the common terminal can be recalculated. Any common design tool can be used to design filters of required characteristics.

There are two common types of filters which in the ideal case do not give a ripple in the passband. Chebychev type 2 (inverse Chebyshev) and Butterworth filters. The order of inverse Chebyshev filter can be found by the expression as shown in Equation 4.23.

$$N = \frac{cosh^{-}1(\sqrt{1-\delta_2^2}/(\epsilon\delta_2))}{cosh^{-}1(\omega_s/\omega_p)} \tag{4.23}$$

Where,
δ_1=the maximum pass band attenuation,
δ_2=required stop band attenuation,
ω_s=normalised stop band frequency,
ω_p=normalised pass band frequency,
$\epsilon = \frac{\sqrt{1-{\delta_1}^2}}{\delta_1}$.

If we use the normalized passband frequency to be 1 and the normalized stop band frequency to be 1.4, with 3dB of passband attenuation and 20dB of stopband attenuation. A 4th order filter would be required. Similarly Equation 4.24 shows the equation for the order of a Butterworth filter.

$$H_{j\omega} = \frac{H_0}{\sqrt{1+\epsilon^2\frac{\Omega_s}{\Omega_p}^{2n}}} \tag{4.24}$$

Where,
Ω_s=normalised stop band frequency,
Ω_p=normalised pass band frequency,
ϵ=$\sqrt{1-{\delta_1}^2}$,
H_0=maximum passband gain,
n=order of filter.
Using similar values as of the inverse chebychev filter, a butterworth filter would require a 7th order filter. Therefore it is seen that an inverse chebychev filter would need a lower order of filter to achieve the same specifications.

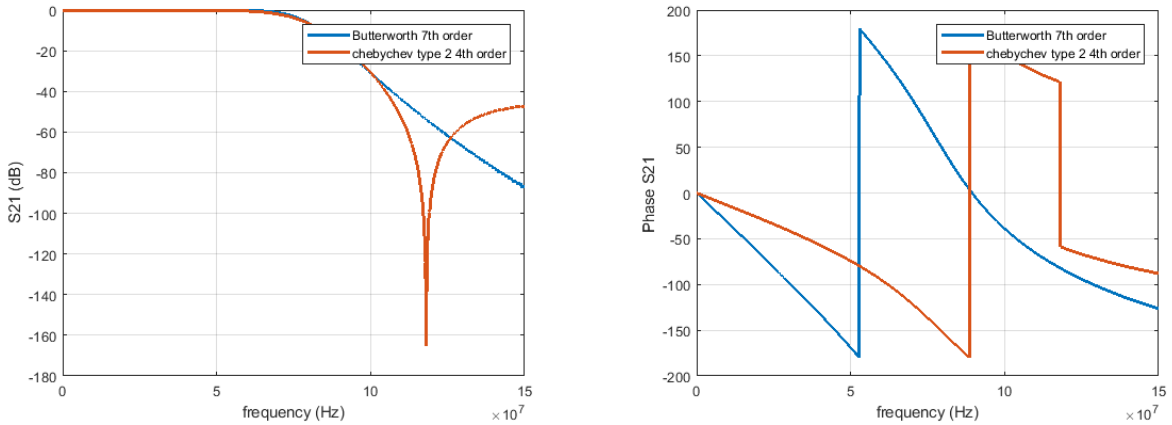

(a) gain comparison of the two filters

(b) phase comparison of the two filters

Figure 4.13: Imagecomparing the gain and phase of a butterworth and chebychev filter

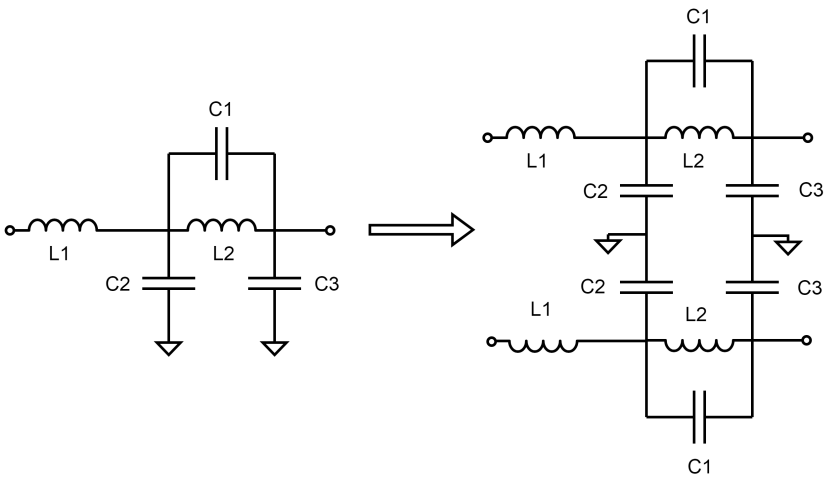

Figure 4.14: The conversion of a single ended to differential filter. The ground terminal can be removed and the value of the capacitor can be recalculated.

Low pass Filter

Figure 4.14 shows the design of a single-ended inverse Chebyshev filter to a differential filter. The ground node can be removed and the value of the capacitor can be recalculated.

Where, L1=68nH, L2=113nH, C1=16pF, C2=56pF, C3=15pF. Figure 4.15 shows the forward gain and phase of monte carlo simulation results a single ended filter and Figure 4.16 shows the same results for a differential filter. The simulation was run for 100 trials with 10variation on all the components.

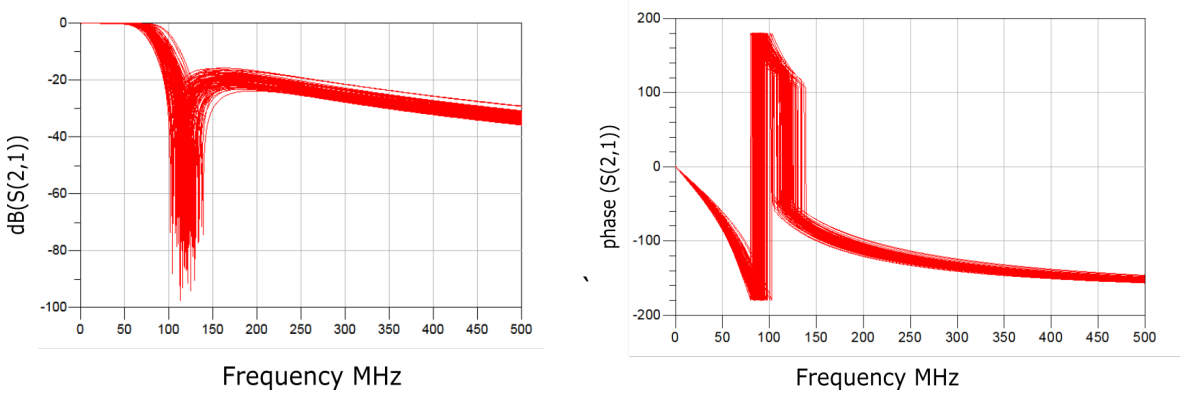

(a) Monte Carlo results for a single-ended filter gain

(b) Monte carlo results for a single ended filter phase

Figure 4.15: Monte carlo results for a differential filter gain

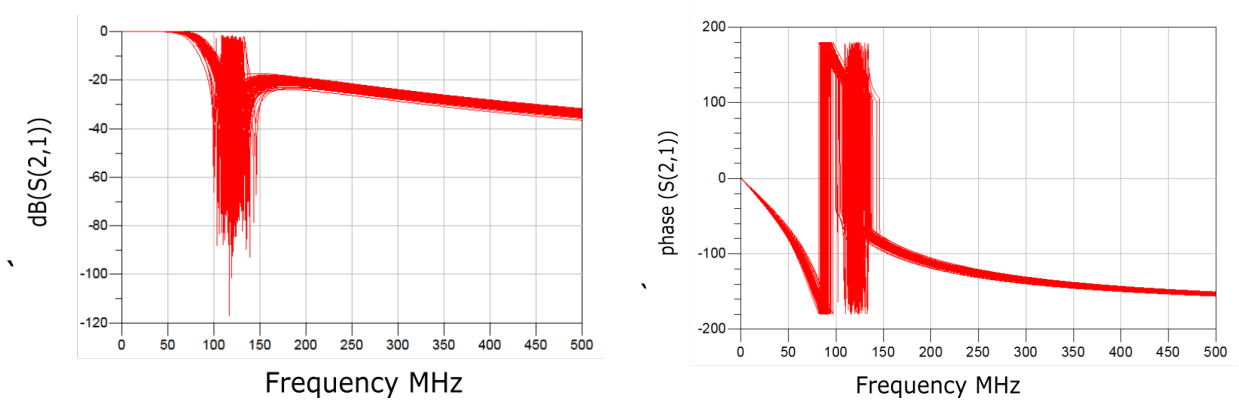

(a) figure

(b) Monte carlo results for a differential filter phase

Figure 4.16: Graphs showing the Monte Carlo results for a single-ended and differential filter gain and phase.

It can be seen that there are some extra peaks in the differential filter due to mismatches, but they occur outside the band of interest. The same filter was used after the first amplifier, but not in a fully differential configuration.

Highpass Filter

A 3rd order inverse Chebyshev filter was used, as shown in figure 4.17. These kinds of filters cannot be converted into a differential configuration as there are series elements to ground. Therefore they are used after the first amplifier to form a bandpass filter.

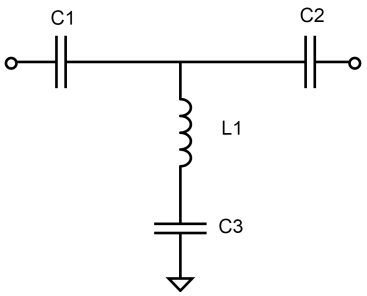

Figure 4.17: A single ended inverse chebychev 4th order filter

Where C1,C2=52pF

4.5. Common mode isolation

As mentioned in the previous chapter 3, common-mode signals can cause external noise to enter the system. Stray currents on the chassis of the body can also enter the system and cause distortion and degrade the performance of the amplifier. To mitigate these effects a transformer is used at the input of the amplifier. A 4:1 transformer from Mini circuits is used. The antenna is connected to a higher turn ratio of the transformer to reduce the impedance of the antenna to match the input filter better. The transformer helps in the following things:

- Isolate the grounds between the antenna and the amplifier
- Rejects high common-mode signals.
- Reduces antenna impedance.
- Reduces susceptibility of common mode currents from chassis to enter the system

4.6. Implementation

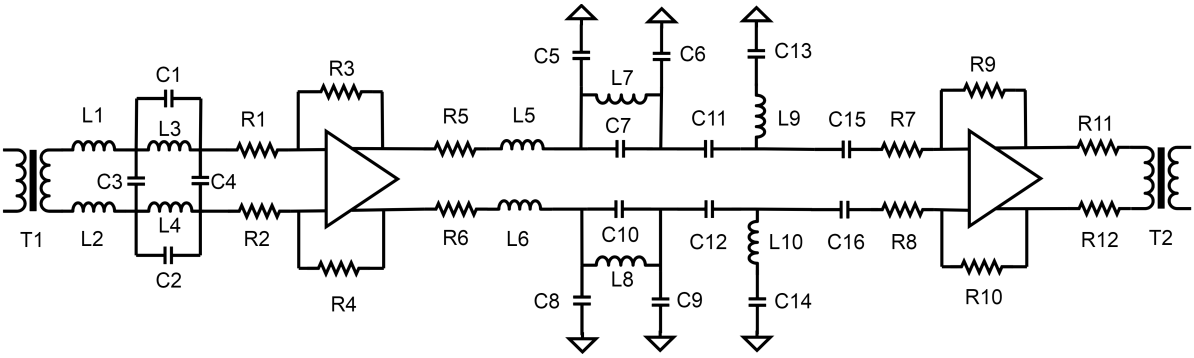

Figure 4.18: Image showing the integrated subsystems.

Figure 4.18 shows the final system implementation architecture. The input filter has been chosen to be fully differential with the transformer at the input to provide isolation at the input of the amplifier. Op-amp THS4511 has been chosen for both stages with a simple resistive feedback topology as a transimpedance amplifier. The second stage filters are not made differential due to practical issues during layout. A transformer is used at the output to help in shifting the level of voltage according to the input of the SDR and also to match better to it. The values are summarized in table 4.3.

Table 4.3: Table summarizing the values of components for the design.

Component	Value	Unit
T1	ADT4-6T (2:1)	
L1,L2,L5,L6	68	nH
C3,C5,C8	110	pF
L3,L4,L7,L8	113	nH
C1,C2,C10,C7	16	pF
C4,C6,C9	30	pF
R3,R4	1825	Ω
R1,R2,R7,R8,R11,R12	50	Ω
C11,C12,C15,C16	52	pF
L9,L10	65	uH
C13,C14	1	uF
R9,R10	1200	Ω
Amp1.Amp2	THS4511	

4.7. Summary

The receiver design has been done based on noise contributions from various blocks such as the amplifier, ADC and the antenna. The radiometer equation has been used to identify the noise contributions from the antenna, and it can be seen that the efficiency of the antenna also plays a role in determining the noise temperature of the antenna. To design the amplifier chain, the noise budget has been found by assuming that the receiver is noise requirements are also isotropic. It was found that at low frequencies the noise budget increases, because of the increases in galactic noise at low frequencies due to Quasi thermal noise. A fully differential architecture with IC THS4511 has been chosen based on high gain bandwidth, rail to rail capability and high common-mode rejection ratio. The design for differential filters has been shown, where a single-ended ended filter has been converted to a differential filter at the input of the amplifier. To provide common-mode isolation and galvanic isolation for RF and antenna ground, a transformer is used at the input of the amplifier. An output transformer is also used to match the ADC and adjust the level of output signals.

5

Measurement and Discussions

This chapter discusses the simulations and measurement results that were obtained by assembling the design shown in section 4.6. The simulation setup was made in Keysight ADS. The PCB was made at ASTRON and different measurements including gain, single and differential noise figure, linearity and open and short noise were conducted. The first part of the chapter compares the simulation and measurement results, whereas the second part discusses the inferences drawn from the results.

5.1. Simulation setup

The model of THS4511 is provided by Texas instruments and has been used for simulation. All the simulations have been done on Keysight ADS. The complete circuit is shown in figure 5.1.

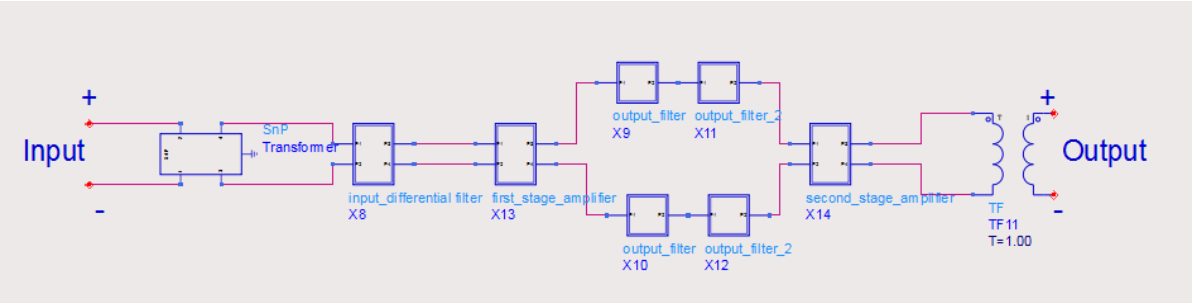

Figure 5.1: Image showing the simulation model of various blocks in Keysight ADS

The implementation of the design was done on a two-sided PCB with the FR4 substrate. The input transformer, filter, amplifier, and out filters were implemented on one PCB whereas the second stage amplification stage was implemented on a different PC board. The output lowpass filter values were changed a bit since a large inductor value was needed, which causes a self-resonance in the band of interest. Therefore the value of the inductor was reduced and the values of the capacitor were recalculated. In the following sections, simulation results are compared to measured results.

5.1.1. Gain

The gain pf the system can be found by measuring the S-parameters of the system. The measurement setup is shown in figure 5.2.

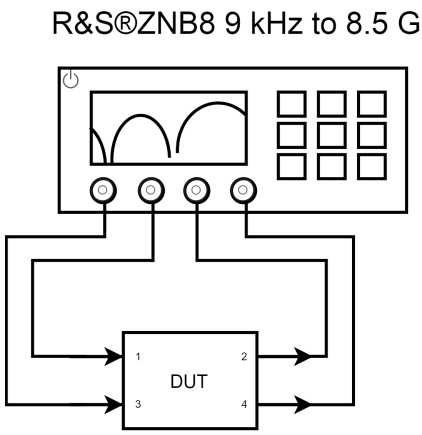

Figure 5.2: Figure depicting the measurement setup used to measure the four port S- parameters of the system.

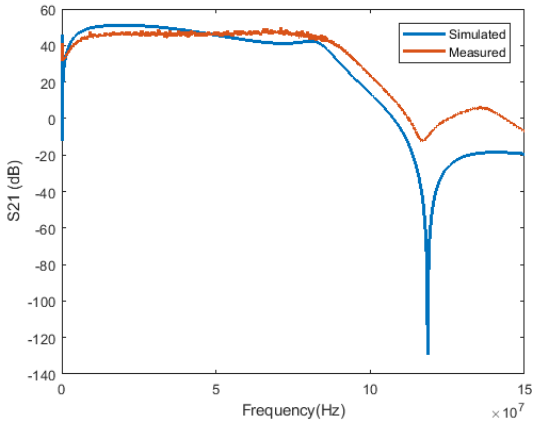

Figure 5.3: Graph comparing the simulated and measured S21 parameter

Figure 5.3 shows the measurements and simulated value of the differential gain of the system. The port S21 has been defined deferentially in the network analyzer where port two is the out of phase combination of port 2 and 4 and port 1 is an out of phase combination of port 1 and 3. It can be seen at low frequencies the two are a bit off, which is due to the simulation model being used. The filter response is not the same as the Q values for the real world filters are much lower than that of the simulation model.

5.1.2. Linearity

The linearity of the measure can be measured by several methods and is expressed in many different factors such as IIP3, IIP2, IM3, IM2, 1dB compression point, etc. The method used here is the measure of OIP3 and IM3. Using these the value for IIP2 can be found. The measurement is done by mixing two tones of equal power with a difference in frequency at the input of the amplifier. The non-linearity in the amplifier causes the mixing of the two tones and produces intermodulation tones at the output. The difference of the fundamental tone and the intermodulation product at the output is known as the IM3 value of the amplifier. The test setup is described in the figure 5.4.

$$OIP3 = -P_f + \frac{\Delta}{2} \tag{5.1}$$

$$IIP3 = OIP3 - Gain \tag{5.2}$$

Where P_f is the power at the output of the fundamental tone and Δ is the difference in power between the fundamental tone and the harmonics. The measurements are summarised in table 4.10 Table 5.1 summarises the values for OIP3 and IIP3

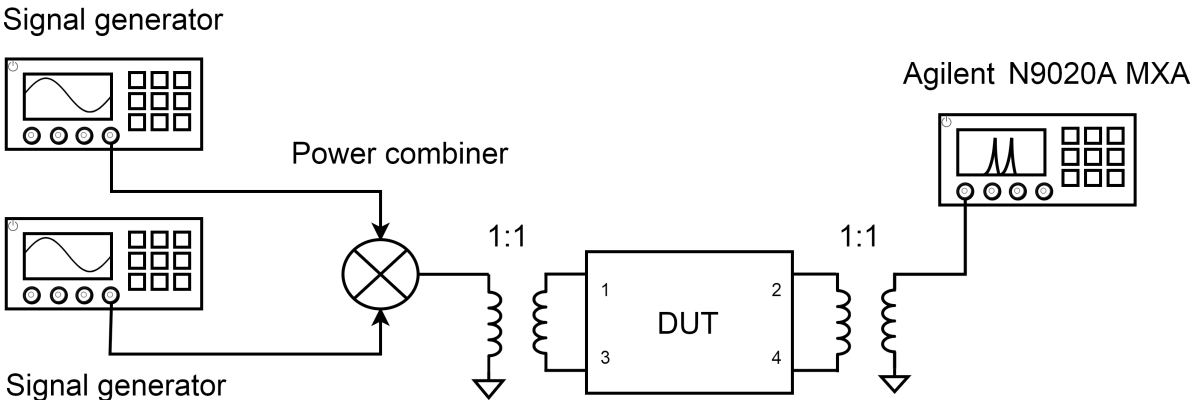

Figure 5.4: Image showing the test bench for linearity of the amplifier.

Table 5.1: Table summarizing the OIP3 and IIP3 values at three frequencies

Frequency	IM	Requirement IM	OIP3	IIP3
3 MHz	64 dBm	50 dBm	32 dBm	-1 dBm
30 MHz	62.6 dBm	50 dBm	31.3 dBm.	8.7 dBm
80 MHz	62 dBm	50 dBm	31 dBm	9 dBm

It can be seen from figure C.3, that the third harmonic levels are much lower than requirements for the entire frequency band. The intermodulation products have been sufficiently suppressed which helps in the mitigation of external noise and the differential architecture provides further suppression of second-order harmonics. It can be seen that the two transformers added to make the system single-ended are from Mini-Circuits, ADT1-1WT, and also add to losses in the circuit. These losses are small but are considered during measurements.

5.1.3. Noise figure

Noise figure is a measure of degradation of the SNR ratio from the input to the output of the system. It is defined as the ratio of signal to noise ratio at the input to the SNR at the output. It can be expressed as shown in equation 5.3.

$$\text{Noise Factor } (F) = \frac{\left(\frac{S_{in}}{N_{in}}\right)}{\left(\frac{S_{out}}{N_{out}}\right)} \tag{5.3}$$

Where,
S_{in}=Signal level at the input,
S_{out}=Signal level at the output,
N_{in}=Noise level at the input,
N_{out}=Signal level at the output.

When the noise factor is expressed in logarithmic terms, it is known as the noise figure. It is a commonly used term as a figure of merit of the amplifier or analog signal chain referred to as the input of the amplifier.

$$\text{Noise figure} = 20log\,(\text{noise factor}) \tag{5.4}$$

The measurement of the noise figure is an important parameter for low noise applications. Measurement of single-ended systems can be done using the Y-factor method which uses a "hot-cold" source. When measuring very low noise systems, it becomes important to de-embed the noise from the spectrum analyzer, which can lead to inaccuracies. To characterize the noise source, a parameter Excess noise Ratio is used (Excess noise ratio). This parameter is used to calibrate the noise source.

$$ENR_{db} = \frac{T_s^{on} - T_s^{off}}{T_0} \tag{5.5}$$

Where,
T_s^{on}=Noise temperature when the source is ON,
T_s^{off}=Noise temperature when the source is ON,
T_0=290 K.
The Y factor is the ratio of two noise power levels, one measured with noise source switched ON and the second one when the noise source is switched OFF.

$$Y = \frac{N^{ON}}{N^{OFF}} \tag{5.6}$$

As the noise powers are directly related to noise temperatures, the Y-factor can also be expressed in noise temperatures.

$$Y = \frac{T^{ON}}{T^{OFF}} \tag{5.7}$$

The first set of measurements is taken without the DUT with, the noise source connected directly to the spectrum analyzer and the cold and hot measurements are taken. This is done for calibration purposes, to remove the influence of the noise of the spectrum analyzer.

$$T_2 = \frac{\left(T_s^{ON} + Y_2\, T_s^{Off}\right)}{(Y_2 - 1)} \tag{5.8}$$

The second set of measurements are taken with the noise source at the input of the DUT. The noise

$$T_{12} = \frac{\left(T_S^{ON} - Y_{12}\, T_S^{OFF}\right)}{(Y_{12} - 1)} \tag{5.9}$$

Using the four measurements, the gain of the system can be calculated using equation 5.10

$$G_1 = \frac{\left(N_{12}^{0N} - N_{12}^{0FF}\right)}{\left(N_2^{0N} - N_2^{0FF}\right)} \tag{5.10}$$

and the noise temperature can be found using equation 5.11.

$$T_1 = T_{12} - \frac{T_2}{G_1} \tag{5.11}$$

The noise temperature found can be converted to noise factor a noise figure using equation 5.12.

$$F = \frac{T_0 + T_1}{T_0} \tag{5.12}$$

Where, T_0 is the reference temperature, defined to be 290 K and T1 is the noise temperature found from equation 5.11

5.1.4. Measurement of differential noise figure

The measurement of a differential DUT is more difficult than the measurement of a single-ended device. The procedure of measuring the differential noise figure is explained in the work [37] . To find the differential noise figure, first, the noise contribution is found for all four, two-port network combinations. These can be found from following the same procedure as done in single-ended devices, but with all other ports terminated to 50 Ω.

$$F_{21} = 1 + \frac{N_{21}}{kT_0\Delta f G_{21}}, \quad F_{23} = 1 + \frac{N_{23}}{kT_0\Delta f G_{23}}, \quad F_{41} = 1 + \frac{N_{32}}{kT_0\Delta f G_{41}}, \quad F_{43} = 1 + \frac{N_{42}}{kT_0\Delta f G_{43}} \tag{5.13}$$

These can be used to find the noise contributions of the amplifier at ports 2 and 4. This can be done by using equations 5.14.

$$\begin{aligned}
\frac{N_3}{kT_0\Delta f G_{21}} &= F_{21} - 1 - \frac{G_{23}}{G_{21}} - \frac{G_{24}}{G_{21}} \\
\frac{N_4}{kT_0\Delta f G_{43}} &= F_{43} - 1 - \frac{G_{41}}{G_{43}} - \frac{G_{42}}{G_{43}} \\
\frac{N_3}{kT_0\Delta f G_{23}} &= F_{23} - 1 - \frac{G_{21}}{G_{23}} - \frac{G_{24}}{G_{23}} \\
\frac{N_4}{kT_0\Delta f G_{41}} &= F_{41} - 1 - \frac{G_{43}}{G_{41}} - \frac{G_{42}}{G_{41}}
\end{aligned} \tag{5.14}$$

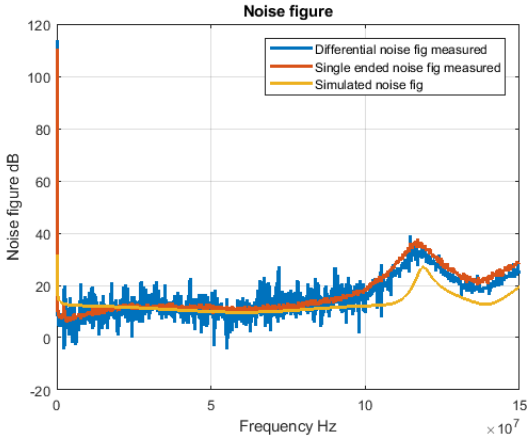

Figure 5.5: Image comparing the measured differential and single ended noise figure to the simulated noise figure.

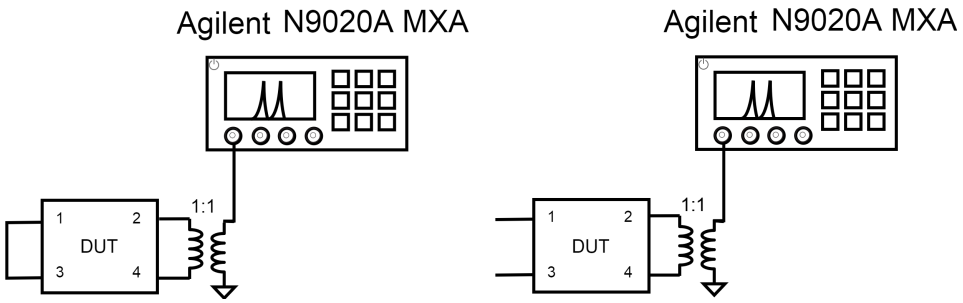

Figure 5.6: Image describing the test bench for open and short noise of the DUT

The set of equations from 5.14, have two equations for N3 and N4 and can be solved analytically or by averaging of multiple readings. This method requires prior knowledge of the gain of the amplifier, which are found in section 5.1.1. To completely analyse the noise behaviour, the noise co-relation between N3 and N4 need to addressed. They are found by using equation 5.15

$$\begin{aligned} N_{\text{as1}} &= \frac{N_3 G_{42} - N_4 G_{32}}{G_{31} G_{42} - G_{41} G_{32}} \\ N_{\text{as2}} &= \frac{N_4 G_{31} - N_3 G_{41}}{G_{31} G_{42} - G_{41} G_{32}} \end{aligned} \tag{5.15}$$

Finally, the differential noise figure can be found by substituting equation in 5.15 in equation 5.16

$$F_{\text{diff}} = 1 + \frac{N_{\text{as1}} + N_{\text{as2}}}{2kT_0\Delta f} \tag{5.16}$$

The measured differential, single-ended and simulated noise figures are shown in figure 5.5, It is seen that the noise figure measured matches the simulated noise figure for wide bandwidth, but there is a deviation near the edge of the stopband. This can be due to the losses in the real-world components.

5.1.5. Open and Short Noise measurement

Another method to asses the current and voltage noise of the analog chain is to measure the input-referred voltage and current noise. To find the input-referred voltage noise, the input terminals are left open and the power at the output is measured by on a spectrum analyzer. The analyzer is a 50Ω system, therefore the output referred voltage noise3 can be calculated from the noise power. This can be referred back to the input of the amplifier by diving it by the gain of the amplifier. The test setup is shown in figure 5.6.

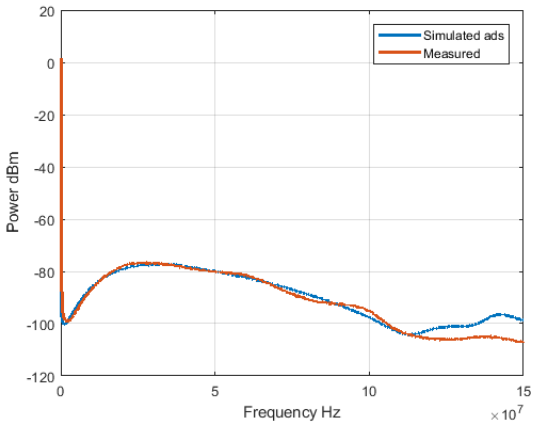

(a) Image showing the power spectrum at the output of the amplifier with the inputs open as measured by a spectrum analyzer, compared to simulated value.

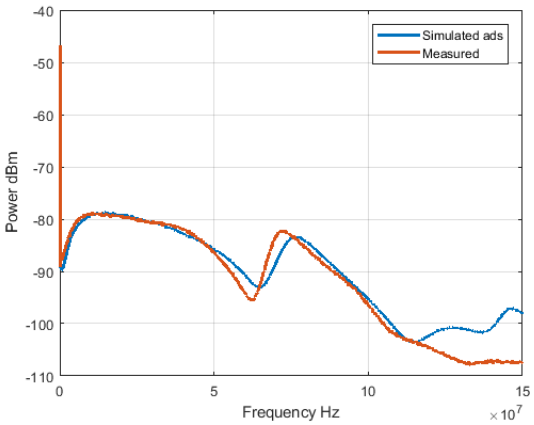

(b) Image showing the power spectrum at the output of the amplifier with the inputs short as measured by a spectrum analyser,compared to simulated value.

Figure 5.7: The image showing the power spectrum measured at the output of the amplifier with the inputs open and shorted compared to simulated values.

Figure 5.7 shows the simulated and measured open circuit and short circuit power measured at the output of the analog chain. The measured values match the simulated.

From the measurements conducted, it can be seen that the gain, linearity, and noise of the simulation model match the measured values. The gain curve is a few dB off at some frequencies but that can be due to the real-world component losses etc. The linearity is found from the IM2 measurements and then finding OIP and IIP values, where it can be seen that the amplifier can handle high power inputs. The differential and single-ended noise figure measurement values match as well. After conducting these tests, it is seen that the simulated model matches the simulated model. As using large antennas in the anechoic chamber is difficult, the antenna impedance was in the simulation setup to check the achieved sensitivity of the system.

5.2. Effect of Antenna Impedance

The tests above have shown that the simulations and measurements are the same in the band of interest. Thus, simulation models can be used to integrate the system with different antenna impedance which has been simulated with the cubesat model.
The sensitivity of the system with the antenna can be found by equation 5.17

$$S_p = \frac{S_n^2}{Z_0 l_{eff}^2} \tag{5.17}$$

Where, S_n is the total input-referred noise by the amplifier chain, Z_0 is the impedance of free space and l_eff is the effective length of antenna which can be found from equation 2.28. The antenna impedance found from simulations and used in ADS to find the achieved sensitivity of the system.

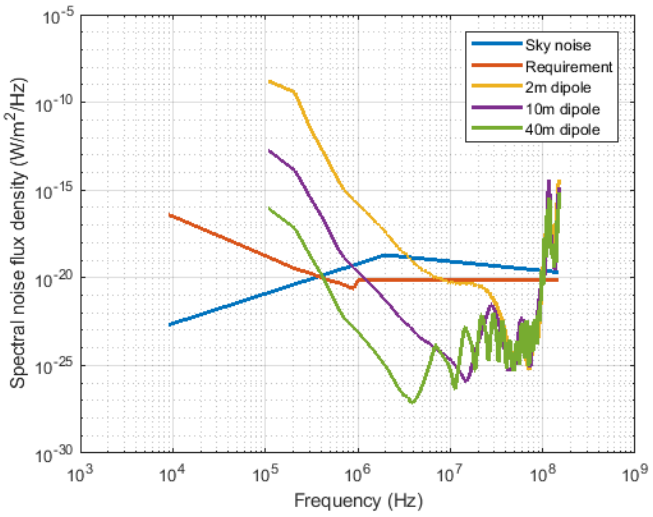

Figure 5.8: Graph showing the achieved sensitivity of the system with different antenna lengths.

Figure 5.8 shows the achieved sensitivity of the system with different antenna lengths. It is seen that, 1)Longer antenna achieve higher sensitivity.
2) there is an increase in noise at the low frequencies which causes the system to be out of specification at these low frequencies. Two main factors for this increase in noise were identified and they have been discussed in the next section.

5.3. Discussions

As seen in the previous sections, the noise behavior during measurement was higher than the calculated noise from chapter 4.4.2. It was found that during the analysis of individual blocks, some assumptions were incorrect. The issues are as follows:

- Increase in noise at low frequencies The noise at low frequencies is higher than the requirement. There are two major factors responsible for it, the interaction of the current noise from the amplifier and the antenna impedance and the effect of input transformer on low-frequency noise.

- It was also found that the common-mode rejection ratio was lower than the expected values. It was identified that the input transformer was reducing the common-mode rejection of the chain.

The following sections look at each of the given issues in detail and explain the mechanism for them. After which a new improved input stage is proposed for better noise performance.

5.3.1. Noise analysis

During noise analysis of the operational amplifier, the source impedance of the antenna was considered to be real and therefore the noise calculations were underestimated.
It was deduced that the noise behavior at low frequencies was increasing due to two factors. The first one is that the impedance of the antenna at low frequencies will be dominated by the capacitance of the antenna and the second one is that the transformer also influences low-frequency noise behavior. The following sections describe the issue in detail and provide extensive analysis of the cause of the increase in noise seen during measurements. The impedance of a short antenna at low frequency is dominated by its capacitance. There is a real part of impedance present called the radiation resistance but it is extremely small. Figure 5.9 shows the model of the antenna at low frequencies and model near its first resonance frequency.

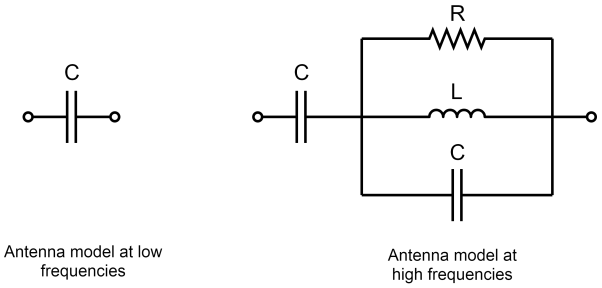

Figure 5.9: Figure showing a representation of the analog chain of the receiver.

This is used as the source impedance

Effect of source Impedance

The analysis from the section can be repeated with the source impedance of the antenna included as a capacitance.

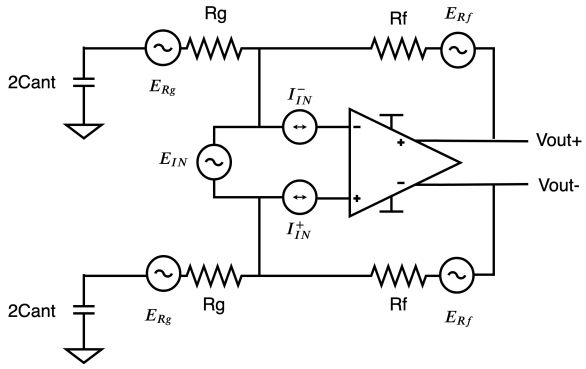

Figure 5.10: Image showing the op amp architecture and its corresponding noise sources with the source impedance

$$E_{od} = \sqrt{\frac{(2E_{in})^2 + (2I_{in}R_{eq})^2 + (2I_{in}R_{eq})^2 + [2(E_{Rg})(1-\beta)]^2 + [2(E_{Rg})(1-\beta)]^2}{(2\beta)^2} + E_{Rf}^2 + E_{Rf}^2} \tag{5.18}$$

Where,

R_{eq}= $\frac{(R_g + \frac{1}{j\omega C})R_f}{(R_g + \frac{1}{j\omega C}) + R_f}$,

$\beta_{feedback}$= $\frac{(R_g + \frac{1}{j\omega C})}{R_f + R_g}$,

E_{Rf}=$\sqrt{4kTR_f}$,

E_{Rg}=$\sqrt{4kTR_g}$,

Gain= $\frac{\beta - 1}{\beta} = \frac{-R_f}{R_g + \frac{1}{j\omega C}}$.

Using flat band values for E_{in} and I_{in} from the data sheet, 2nV/$\sqrt{Hz}$ and 4pA/$\sqrt{Hz}$ respectively at 100 kHz. The input referred noise can be found by dividing the output noise by the gain of the amplifier as shown in equation 5.19.

$$E_{in} = \frac{E_{od}}{Gain} \tag{5.19}$$

The difference in the analysis done earlier in section 4.4.2 is that the gain of the amplifier at low frequencies would be very low when resistive feedback is used as the antenna impedance is very high at low frequencies due to the capacitor. This can be seen as the noise was increasing at low frequencies. Therefore, for the next implementation, capacitive feedback should be used to provide gain at even low frequencies.

5.3.2. Analysis of noise with input transformer

A transformer can be modeled as an ideal block with its ABCD parameter and a magnetization induction L_m. The voltage gain of the transformer is dependant on its turn ration. The voltage is converted by the factor n and current is divided by the factor n. The impedance transformation factor is n^2. This model can be used to see the effect of the transformer on the voltage and current noise from the circuit.

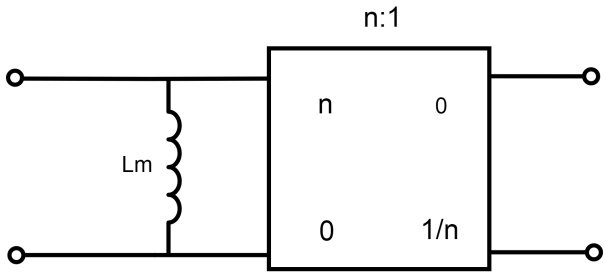

Figure 5.11: Image showing the model for a transformer, where the magnetization induction has been used to see the effects of noise on an otherwise ideal transformer modeled by its ABCD parameters.

Figure 5.11 shows a simplified transformer model used to calculate the effects of the noise at low frequencies. There is additional capacitance which has not been used in this model to maintain simplicity and give a first-order approximation. The magnetization induction has been used with the ABCD parameters of the transformer. This inductor can be either on the primary or the secondary side of the transformer and scales according to the turn ratio of the transformer.

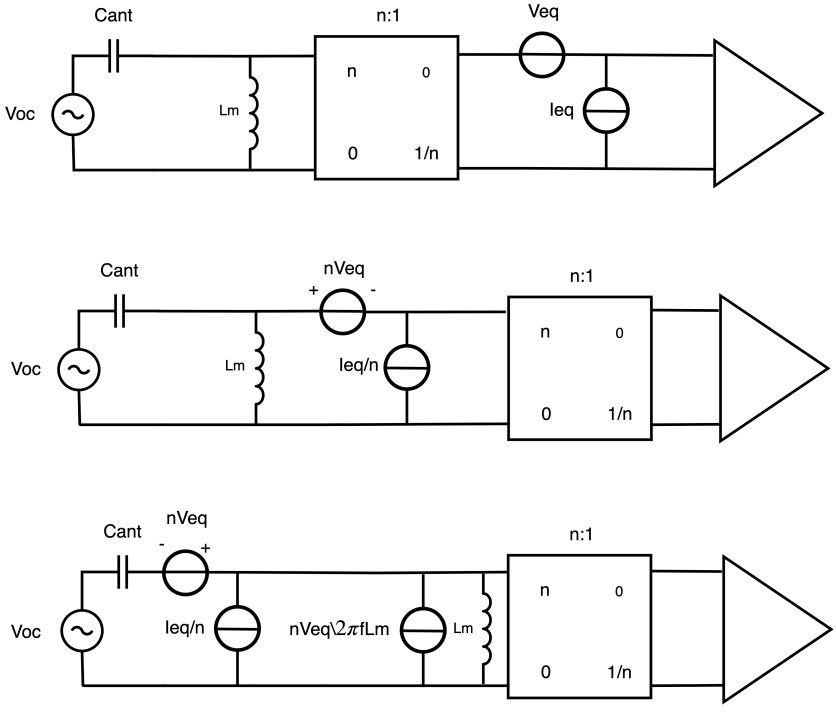

Figure 5.12: Image showing the schematic for the analog chain with the model of the antenna impedance, transformer, and the amplifier. The model uses a nullor with the noise modeled at the input as a current and voltage source. The image shows these noise sources are transformed to a reference plane before the transformer.

Figure 5.12 shows the model of the antenna impedance, transformer and the amplifier. The noise from the amplifier have been modeled as a voltage and a current source at the input of the amplifier. These noise sources are transformer over the transformer from the secondary side to the primary side. Due to the transformer, the voltage noise will increase by the turn ratio and the current noise will reduce by the same ratio. But due to the magnetization induction L_m causes a current noise term due to the transformation of voltage

over. This added term is dependant on the inductor value and the impedance of the antenna. The equivalent noise at the input can be expressed as shown in equation 5.20.

$$V_{inputeq} = \sqrt{n^2 V_{eq}^2 \left[1 + \frac{1}{4\pi^2 f^2 L_m^2 4\pi^2 f^2 C_{ant}^2}\right] + \left[\frac{I_{eq}^2}{n^2 4\pi^2 f^2 C_{ant}^2}\right]} \tag{5.20}$$

The equation 5.20 shows that the current noise formed due to the inductor, second term in the equation has both the inductance and capacitance of the antenna in the denominator. Therefore the noise contribution of that particular term would be higher at low frequencies. This is seen in the sensitivity cures where the noise at low frequencies is much higher. The combination of the current noise from the amplifier and the voltage noise over the inductance of the transformer causes a rise in the noise behavior at low frequencies. The inductance value of the transformer used was 2 mH, to reduce the effect of this noise, this value should be increased. This would require custom made transformers as most of the commercially available transformer have inductances in the same range.

5.3.3. Common mode rejection ratio

The common mode rejection ratio for an cascaded chain is given by equation 5.21 from the book [31].

$$\frac{1}{CMRR_{tot}} = \frac{1}{CMRR_1} + \frac{1}{F_1 CMRR_2} + ... + \frac{1}{F_1 F_2 F_{n-1} CMRR_n} \tag{5.21}$$

Where,
$CMRR_{tot}$= total CMRR of the cascaded chain,
$CMRR_i$=CMRR of the constituent at i^{th} position,
F_i is the rejection factor, which can be given by:

$$F = \frac{V_{od}}{V_{id}} \frac{V_{ic}}{V_{oc}} \tag{5.22}$$

Which is the ratio of the differential gain to the common-mode gain for voltage amplifiers with floating input and outputs.
It can be seen that the total CMRR of the chain is dominated by the first constituent.
BY measurements, it was found that the transformer's common-mode rejection ratio was less than that of the amplifier used at the input and therefore the input transformer was a contribution to reducing the common-mode rejection ratio at high frequencies.

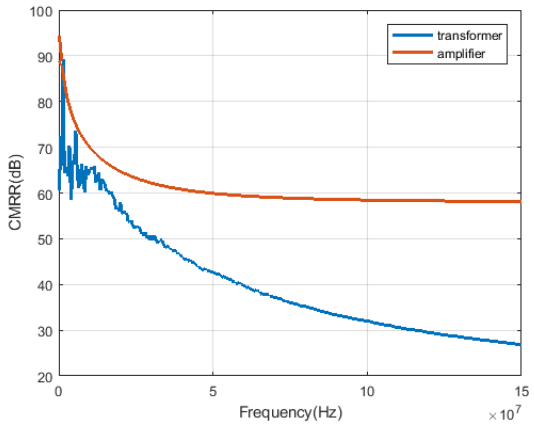

(a) Image showing the comparison of CMRR of the transformer and the amplifier.

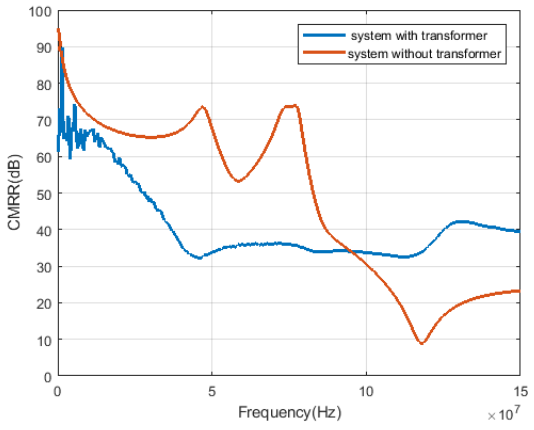

(b) Image showing the comparison of CMRR of the system transformer and the amplifier.

Figure 5.13: Image showing the CMRR of the transformer and the amplifier and the system CMRR with and without the transformer.

Figure 5.13 shows the comparison of the CMRR of the transformer and the amplifier. It can be seen that the CMRR of the amplifier is much higher than that of the transformer. Although the measurements contain

some common-mode noise which gives some peaks in the measurements. The next image shows the system CMRR with and without the transformer, it can be seen that the system without the transformer has a higher CMRR which is what the equation 5.21 predicts.

Therefore the issues described at the beginning of the section arise due to the high current noise of the amplifier and the input transformer being used. The common-mode rejection ratio is also reduced to the inferior CMRR of the transformer compared to the amplifier. Therefore the solutions can be:

- Noise: to reduce the effect of current noise from the amplifier at low frequencies, the length of the antenna can be increased as it increases the antenna capacitance, therefore, reducing the effect of the current noise. But the length of the antenna is already quite long and therefore this solution is not the best.
  The better solution is to reduce the noise from the input stage of the analog chain, which can be done by using devices with minimum current noises such as JFET or CMOS. The input transformer was being used to isolate the systems and provide immunity for common-mode currents running on the chassis. But as the transformer is reducing the sensitivity of the system, a different method for isolation needs to be found or custom made transformer can be ordered which has a high magnetization inductance value.

- CMRR: The transformer is also reducing the common-mode rejection ratio of the system as shown in section 5.3.3. Therefore the transformer has not been used in the next design.

5.4. Improved input stage for low noise

In the previous section, it is shown that the input stage can be designed for low noise to increase the sensitivity of the system. Therefore this section presents an alternative low noise solution for the first stage of the analog chain. To reduce the input-referred noise:

- The transformer from the input has also been removed from the design.

- As a low current noise solution is the apt choice to reduce the impact of the source impedance a JFET input stage amplifier or Op-Amp can be used.

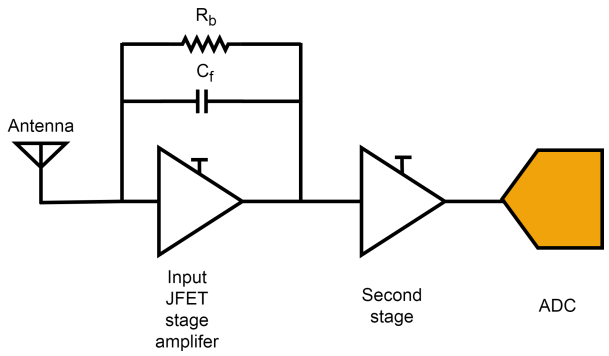

Figure 5.14: Image showing the block diagram of the integrator transimpedance amplifier with JFET input.

- The first stage: The changes are to be done in the first stage. An integrator trans-impedance architecture is used. As at low frequencies, the antenna acts as a capacitor, a feedback capacitor is used. This is different from the previous architecture chosen as there is gain at low frequencies as well. JFET's are used as an input stage as the current noise is three orders of magnitude lower compared to BJT devices. A big bias resistor is used in parallel to the feedback capacitor. The value of this resistor can be adjusted to shift the lower 1/f corner of noise.
  The input transformer has also been removed.

- Second stage: The filters after the first stage of amplification and the second stage used for gain can remain the same as they have very little effect on the input refereed noise.

Figure 5.14 shows the block diagram for the new input stage implementation. Only a single-ended implementation has been shown but a similar implementation can be done for the differential input stage as well.

To analyze the effects of noise with the new input stage, we consider the antenna impedance for a 10m dipole antenna, the input impedance of the JFET stage, transconductance (g_m) of the configuration and the effective length of the antenna. The sensitivity of the system, which can be attained with the input JFET stage used as an integrator trans-impedance amplifier can be found from equation 5.23

$$S_p = \frac{1}{Z_0 l_{eff}^2}\left(\frac{8kT}{3g_m}\left(1+\frac{C_f}{C_{ant}}+\frac{C_{iss}}{C_f+Cant}\right)^2+\frac{1}{4\pi^2 f^2 C_{ant}^2}\left(2qI_G+\frac{4kT}{R_b}\right)\right) \tag{5.23}$$

Where,
k=Boltzmann's constant (JK^{-1}),
T=temperature (K),
Z_0=impedance of free space Ω,
g_m=transconductance (S),
C_f=feedback capacitance (F),
C_{ant}=Antenna impedance (F),
C_{iss}=input capacitance of JFET (F),
l_{eff}=effective length of antenna (m),
f=frequency (Hz),
R_b=feedback resistor Ω.

It can be seen from the equation that the input capacitance of the JFET affects noise behavior. The second factor that majorly affects the noise factor is the bias resistor R_b. The value should be high to decrease the corner frequency. Using typical values for BF861C, where g_m is 30 mS, C_{ant} for a 2m dipole to be $20pF$ and C_f to be 5 pF and R_b to be 10 $Meg\Omega$, the sensitivity possible is in the order of $10^-20\ Wm^{-2}Hz^{-1}$. To achieve higher sensitivity, the gain of the first stage is increased by reducing the size of the feedback capacitor and increasing the size of the antenna. Also, op-amp alternatives can be used such as the Texas Instrument OPA818.

The two configurations with discrete JFET input stage and op-amp OPA818 are shown in figure 5.15

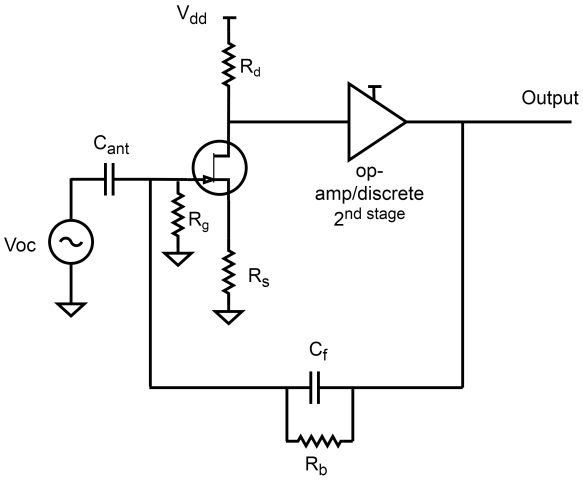

.png

(a) schematic diagram of the discrete JFET input stage with a second stage opamp.

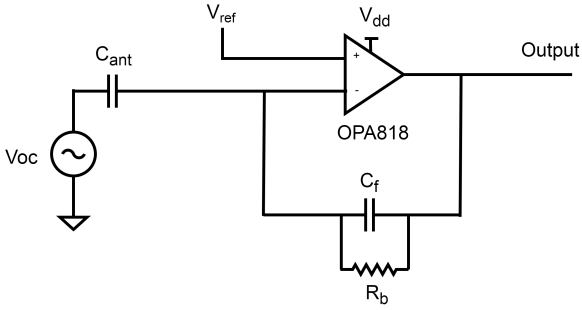

(b) Schematic of a JFET input op-amp OPA818 from Texas Instruments.

Figure 5.15: Image showing the two implementations, one with a discrete JFET input stage and the second one with a JFET input op-amp OPA818 by Texas Instruments.

Figure 5.15 shows the two implementations considered, one with discrete JFET BF861C as the input stage with a BJT amplifier as the second stage, the second one with a JFET input stage op-amp OPA818 by Texas instruments. For the ease of understanding, biasing has not been shown in the op-amp schematic. The op-amp

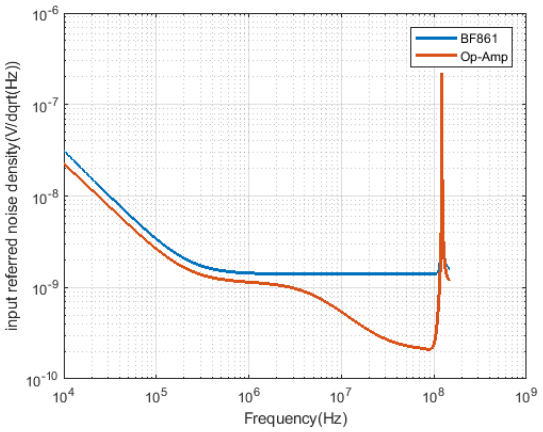

Figure 5.16: Image comparing the simulated input referred noise density of the discrete JFET input stage and OP818.

OPA818 is used as a single supply, therefore, the positive input is biased to mid-rail. The noise performance of both of the architectures is shown in figure 5.16.

Figure 5.16 shows that the input-referred noise from JFET input stages has been significantly reduced as the current noise from the devices is in the order of $fA/\sqrt{Hz}$ which is three order of magnitude lower than the BJT opamp used. Therefore the sensitivity achieved with JFET input stages is better. These designs are made for first order approximations and need to be further investigated on their performance on linearity, stability, PSRR, CMRR.

It can be seen that that in terms of noise performance, JFET devices provide a much better performance compared to BJT's. This is due to low current noise in the devices. Two implementations have been shown which give a first order approximation of the noise behaviour. The only drawback is that the antenna acts as a capacitor only till its first resonance and then the antenna model is more complex involving a parallel resonator. Therefore this configuration needs to be modified to use it for the entire band. A solution to this is to split the band into two parts, where the first part is below the first resonance of the antenna and the second part is above its first resonance. In the low frequency band, a JFET input stage amplifier can be used which provides low noise and in the high frequency band, the earlier implementation can be used, which has been measured to be linear and provides the required sensitivity.

5.5. Summary

Simulations were performed in Keysight ADS and the design was implemented by discrete components at ASTRON on a two-layer PCB. The measurement setup has been described for measuring the gain, linearity and open and short noise of the analog chain. The measured values match the simulated values, confirming the simulation setup. Single-ended and differential noise figure was also measured and it was found to match in the band but the discrepancy was seen at higher frequencies. After this, the antenna impedance was integrated into the simulation setup and the sensitivity is plotted in section 5.2. The sensitivity for a 10 m dipole antenna does not meet specifications below 3 MHz as the noise of the system increases. Two main issues were identified for this increases in noise

- Transformer - magnetization inductance.
- Current noise from the BJT amplifier.

These issues can be solved bu using a JFET at the input of the amplifier as the current noise is around three orders of magnitudes lower than that of the BJT amplifier. Two amplifiers were simulated to check the input-referred noise, one with a discrete input JFET and the second one being a JFET input stage Op-Amp. As shown in figure 5.16, the requirements can be met for a 10 m dipole antenna by using these JFET devices as the input stage and keeping the rest of the analog chain the same.

6

Conclusions and Future work

6.1. Conclusions

OLFAR project aims to deploy an autonomous swarm at the lunar orbit for low-frequency radio astronomy. This thesis has been done to design and implement a sensitive radio receiver for cubesat environments. The focus was on the analog signal path of the payload including the antenna, low noise amplifier, and filters. The design and implementation were done at ASTRON and measurements were done to confirm the simulated results. The findings, conclusion and discussion points for different parts are summarised below.

- Antenna Design: A dipole antenna is chosen as it provides low directivity and an Omni-directional radiation pattern. A study on three different antenna configurations has been done to find the polarization response and the IXR of the three configurations was compared. It was seen that the cross-dipole configuration provides a better performance almost throughout the band and therefore can be used instead of a "tri-dipole configuration", which would save power and area as it would reduce one analog receiver chain.

- RFI: A study has been done on various sources that produce RFI and can couple to the system to degrade its performance. The DC-DC converters in the power supply unit were found to be the main contributors to RFI in the frequency band. MIL-STD461C standards have been used to define the limit for radiated emission from subsystem inside and outside the cubesat for the system to be sky-noise limited. Similarly, a limit on the conducted emissions has also been imposed. Measurements are conducted to find the radiated and conducted emissions from DC-DC converters and it was found that the levels for RFI can be met with extensive filtering on the power lines and using methods such as encapsulating the converters in boxes to stop the propagation of emissions. Methods to mitigate the effects of interference have been suggested.

- System design: As the requirements for an analog chain are not yet well defined in previous literature, an attempt has been made to provide some requirements such as the dynamic range, linearity, noise budgets for different antenna lengths and gain of the amplifiers. Structured electronic design approach has been used to find the noise budget for the low noise amplifier for different antenna lengths, and it was found that a 10m dipole antenna provides enough budget for the amplifier to be implemented by discrete off the shelf components. A fully differential architecture has been chosen with a BJT op-amp to design the amplifier. Differential filters are also used to reduce the reliance on the ground plane. A transformer at the input of the amplifier has been used to isolate the amplifier and the antenna, which was later found to increase noise at low frequencies and reduce the common-mode rejection ratio.

- Measurements: Measurements for the gain, linearity, single-ended and differential noise figure were conducted and the measured values seem to match the simulated values. The measurements validated the simulation model, which was then used to integrate the antenna into the design to check the sensitivity of the system. Although the system achieves sensitivity greater than the NCLE payload, it was found that the current noise and the input transformer increase the noise at low frequencies and reduce the sensitivity of the system significantly.

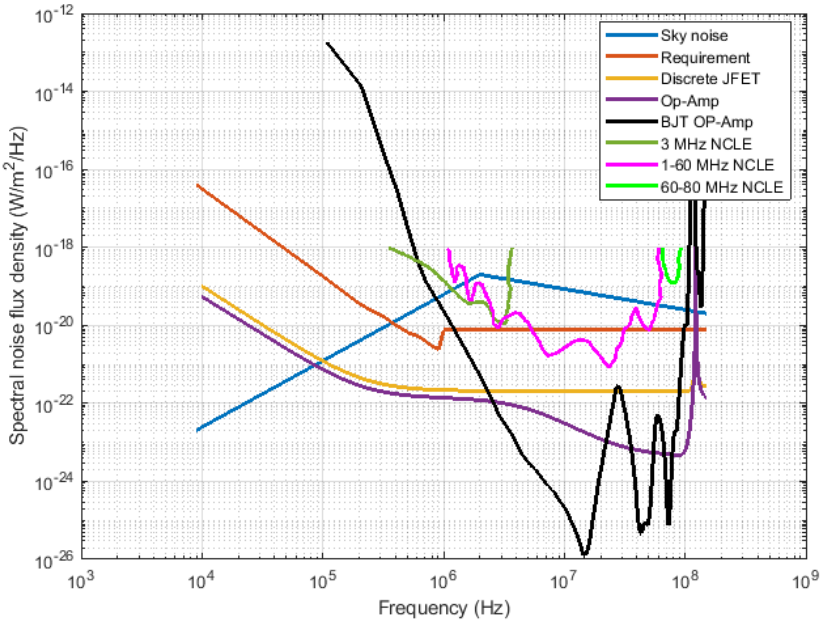

Figure 6.1: Image comparing the achieved sensitivity of the NCLE paylaod with the implemented design and the simulated JFET implementations.

To reduce the noise behavior at low frequencies and achieve higher sensitivity, a JFET input stage design is proposed. This can be implemented in two ways, one with a discrete JFET at the input stage followed by a BJT Op-Amp or a discrete implementation, the second one is by using a JFET input stage Op-Amp. Simulations have shown that both of these designs can provide much greater sensitivity throughout the band. The sensitivity of the NCLE payload, the measured BJT implementation, and the simulated JFET implementations have been shown in figure 6.1

6.2. Future Work

From the measured and simulated data, it can be seen that the simulation model are a good representation of the real-world components, therefore in the next steps, the proposed JFET design can be implemented and tested. In terms of subsystem design, the following provides a good pathway towards a first flight model for the OLFAR project:

- Measurements of RFI using a fully integrated power supply unit. As most of the RFI generated from the power supply unit, to get better estimates of the common mode and differential mode RFI, a full test should be conducted in an anechoic chamber and changes in the design can be made accordingly.
- Testing of hardware can be conducted using high altitude balloon experiments to test the robustness of the system.
- Study and implementation of a dedicated ADC should be done to serve the needs of high dynamic range which is needed for such applications.
- Study the feasibility of using CMOS technology and its performance compared to other technologies such as JFET and BJT for low-frequency astronomy from space and other such applications.

This thesis provided a nice starting point for further investigation of the other practical aspects of making sensitive radio receivers for cubesats. It can be seen that low current noise devices such as JFETs and CMOS should be used. There are still several factors that can affect the functionality of the system. As the cubesat would contain many more subsystems, the best way to characterize interference and behavior of the system would to conduct a fully integrated flight test and derive new requirements accordingly.

A

Appendix A

A.1. Antenna Simulation Results

A.1.1. Reflection Coefficient of different antenna length

ALTAIR Feko has been used to simulate dipole antennas of various lengths to find the reflection coefficient.

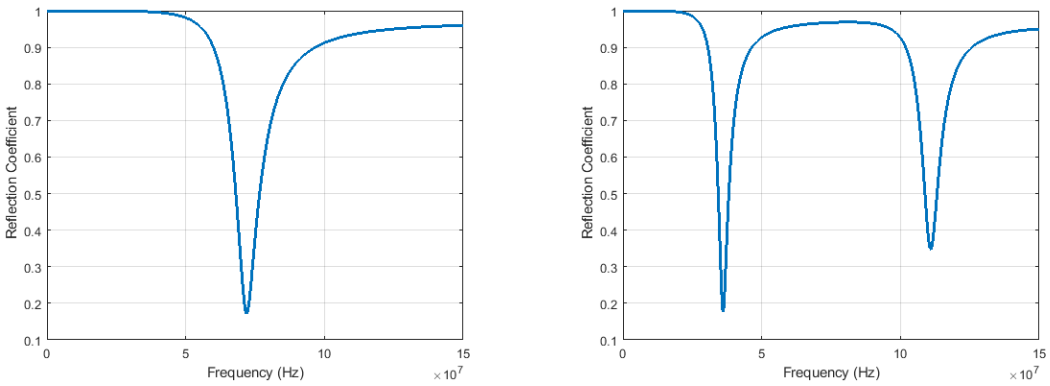

(a) Reflection coefficient of a 2m dipole antenna

(b) Reflection coefficient of a 4m dipole antenna

Figure A.1: Graphs showing the reflection coefficient for 2m and 4m dipole antenna

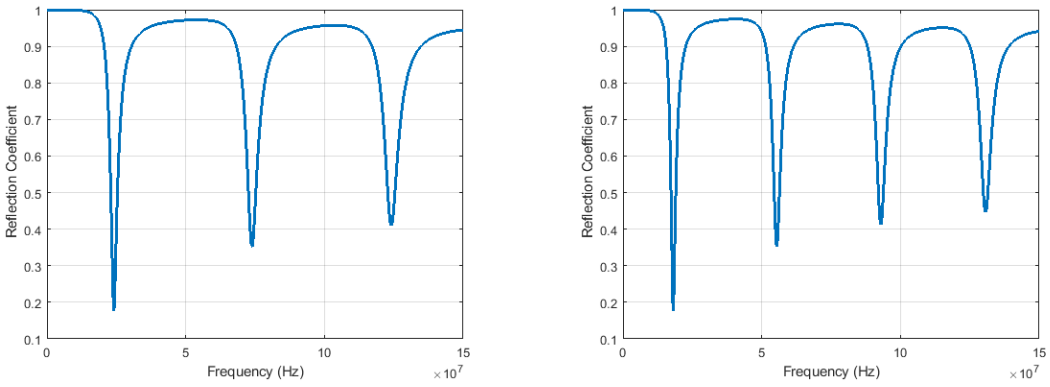

(a) Reflection coefficient of a 6m dipole antenna

(b) Reflection coefficient of a 8m dipole antenna

Figure A.2: Graphs showing the reflection coefficient for 6m and 8m dipole antenna

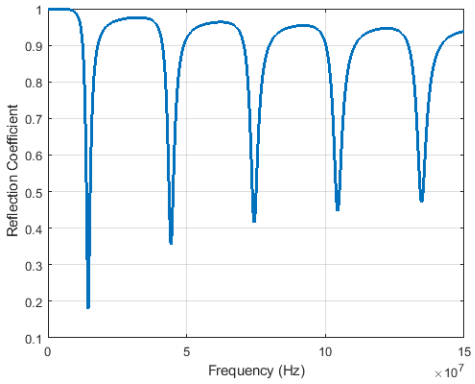

(a) Reflection coefficient of a 10m dipole antenna

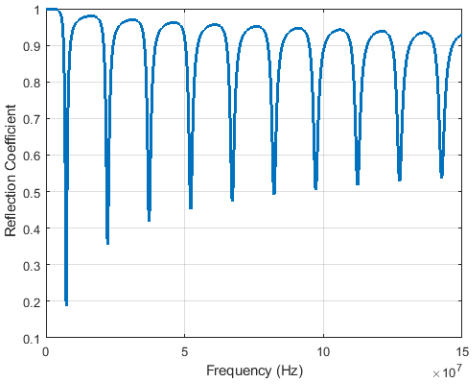

(b) Reflection coefficient of a 20m dipole antenna

Figure A.3: Graphs showing the reflection coefficient for 10m and 20m dipole antenna

A.1.2. Impedance of different antenna length

Imaginary Impedance

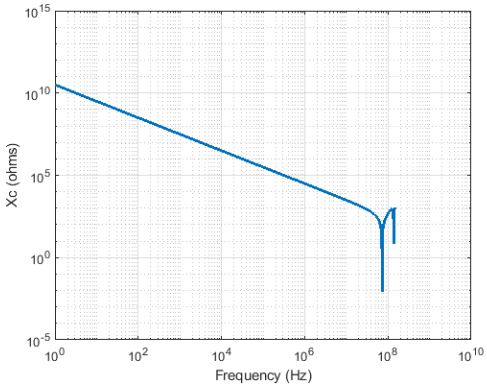

(a) Imaginary part of impedance of a 2m dipole antenna

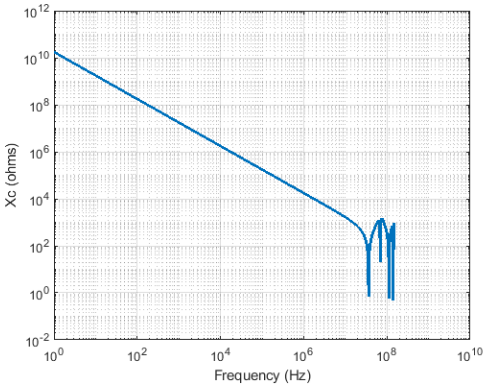

(b) Imaginary part of impedance of a 4m dipole antenna

Figure A.4: Graphs showing the imaginary part of impedance for 2m and 4m dipole antenna

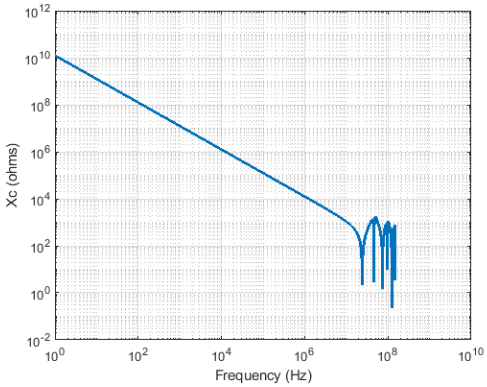

(a) Imaginary part of impedance of a 6m dipole antenna

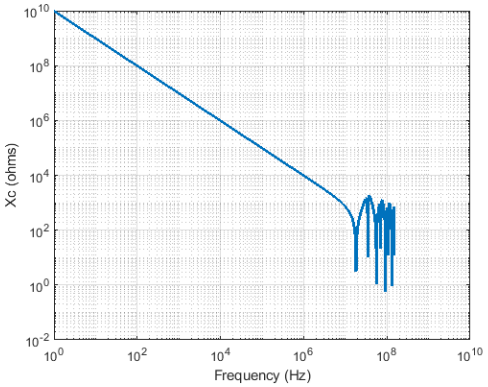

(b) Imaginary part of impedance of a 8m dipole antenna

Figure A.5: Graphs showing the imaginary part of impedance for 6m and 8m dipole antenna

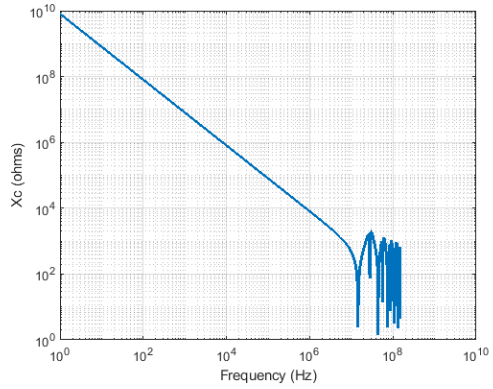

(a) Imaginary part of impedance of a 10m dipole antenna

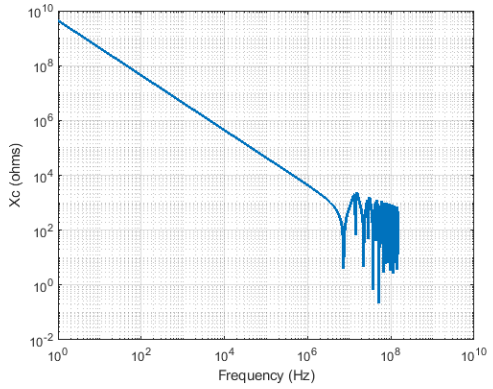

(b) Imaginary part of impedance of a 20m dipole antenna

Figure A.6: Graphs showing the imaginary part of impedance for 10m and 20m dipole antenna

Real Impedance

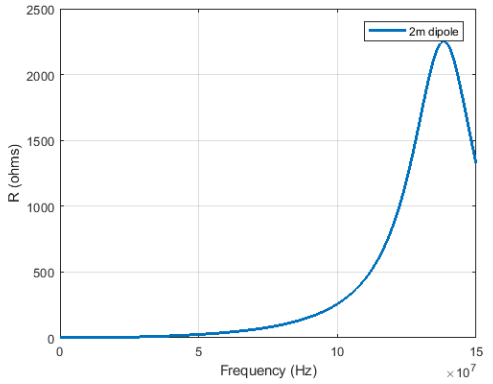

(a) Real part of impedance of a 2m dipole antenna

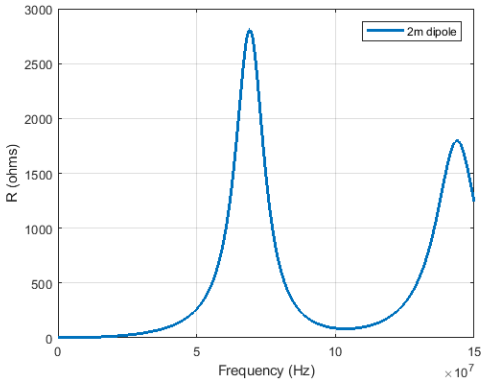

(b) Real part of impedance of a 4m dipole antenna

Figure A.7: Graphs showing the real part of impedance for 2m and 4m dipole antenna

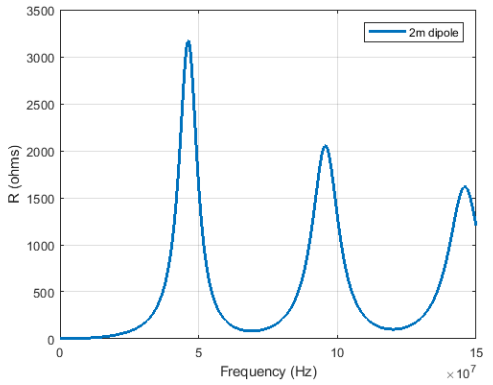

(a) Real part of impedance of a 6m dipole antenna

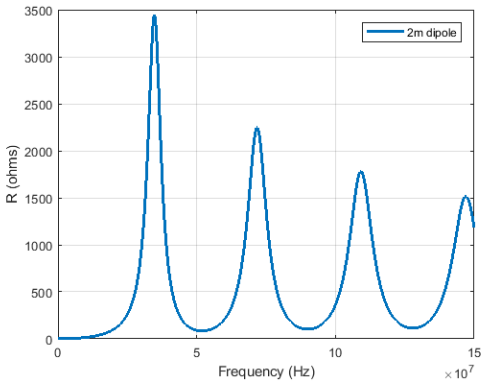

(b) Real part of impedance of a 8m dipole antenna

Figure A.8: Graphs showing the real part of impedance for 6m and 8m dipole antenna

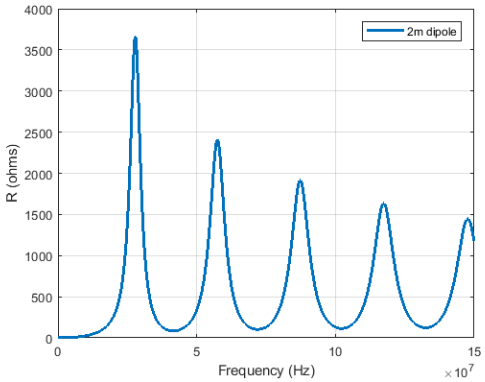

(a) Real part of impedance of a 10m dipole antenna

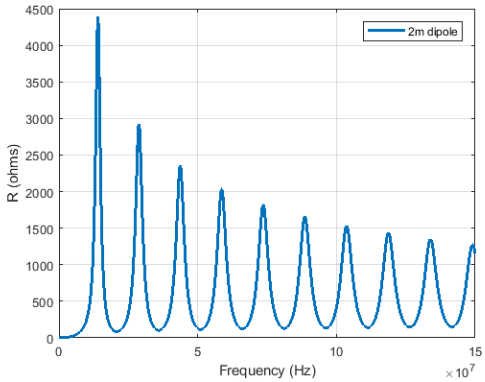

(b) Real part of impedance of a 20m dipole antenna

Figure A.9: Graphs showing the real part of impedance for 10m and 20m dipole antenna

A.1.3. Capacitance of antenna for different lengths

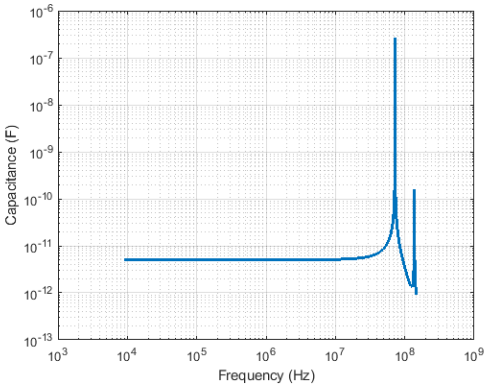

(a) Capacitance of a 2m dipole antenna

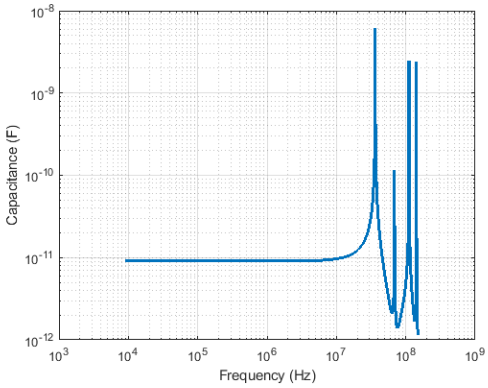

(b) Capacitance a 4m dipole antenna

Figure A.10: Graphs showing the capacitance for 2m and 4m dipole antenna

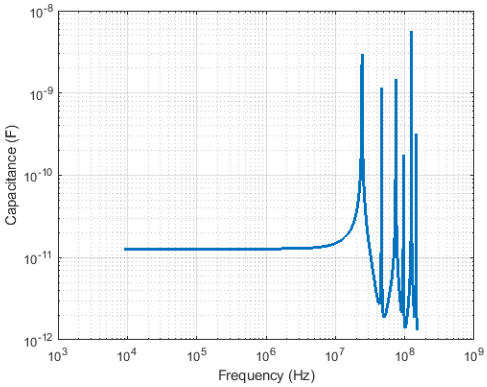

(a) Capacitance of a 6m dipole antenna

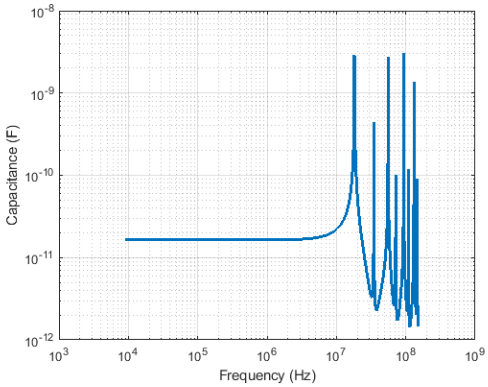

(b) Capacitance a 8m dipole antenna

Figure A.11: Graphs showing the capacitance for 6m and 8m dipole antenna

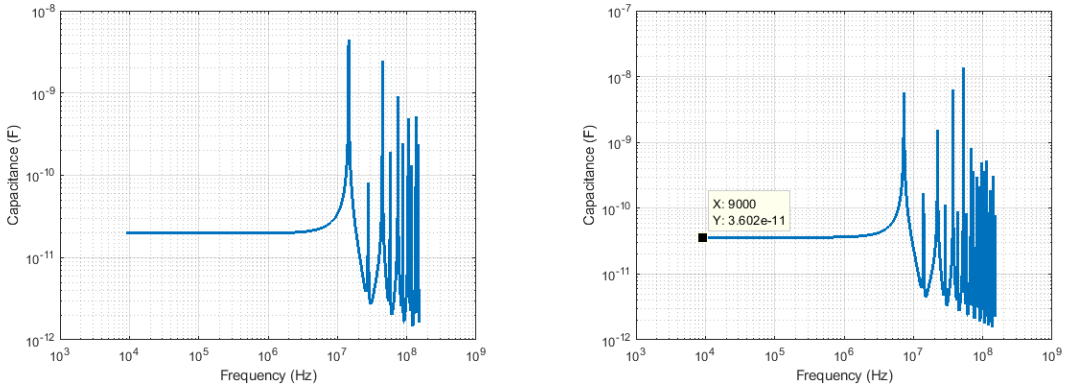

(a) Capacitance of a 10m dipole antenna

(b) Capacitance a 20m dipole antenna

Figure A.12: Graphs showing the capacitance for 10m and 20m dipole antenna

A.1.4. Effective length of antenna

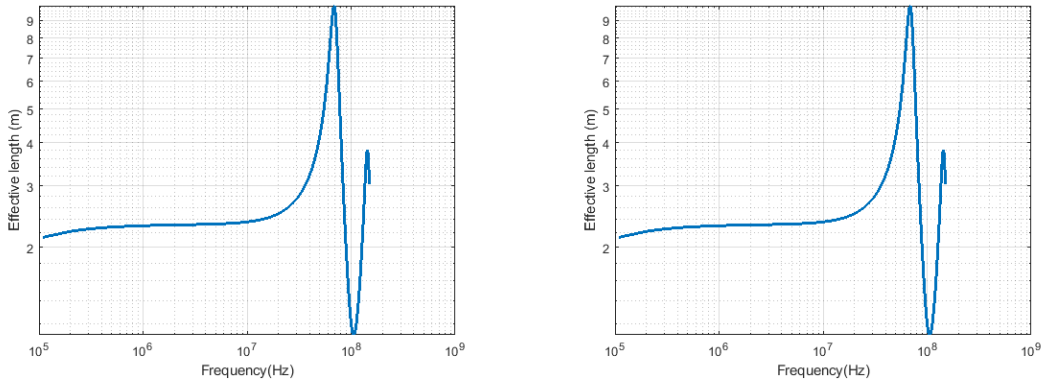

(a) Effective length of a 2m dipole antenna

(b) Effective length of a 4m dipole antenna

Figure A.13: Graphs showing the effective length for 2m and 4m dipole antenna

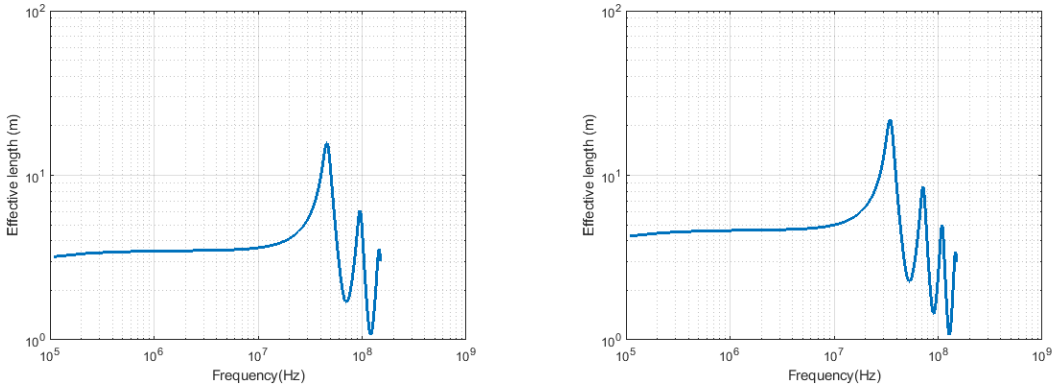

(a) Effective length of a 6m dipole antenna

(b) Effective length of a 8m dipole antenna

Figure A.14: Graphs showing the effective length for 6m and 8m dipole antenna

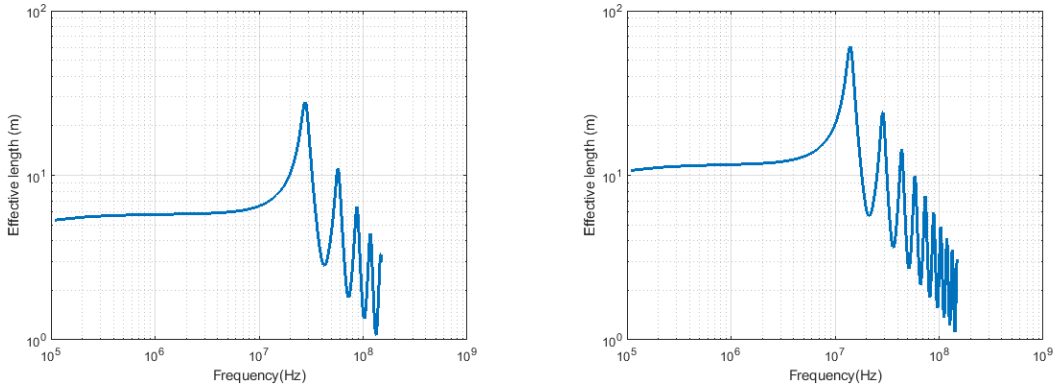

(a) Effective length of a 10m dipole antenna

(b) Effective length of a 20m dipole antenna

Figure A.15: Graphs showing the effective length for 10m and 20m dipole antenna

B

Appendix B

B.1. Measurement setup for radiated and conducted emissions

(a) Measurement setup for radiated emission test

(b) Measurement setup for radiated emission test with light source for solar panels

Figure B.1: Measurement setup for radiated emission test

(a) Measurement setup for conducted emission test

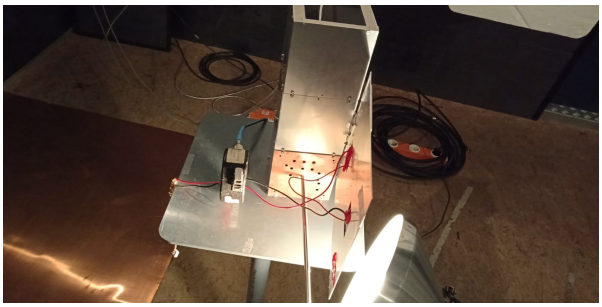

(b) Measurement setup for conducted emission test

Figure B.2: Measurement setup for conducted emission test

B.1.1. Setting of the spectrum analyzer

Trace
Swept SA
A.14.59,N9020A
526 EDP FS1 P26 ,01
Segment,0
Number of Points,1501

Sweep Time,56.669605610062
Start Frequency,3000000
Stop Frequency,50000000
Average Count,0
Average Type,LogPower(Video)
RBW,1000
RBW Filter,Gaussian
RBW Filter BW,3dB
VBW,3000
Sweep Type,Swept
X Axis Scale,Lin
PreAmp State,On
PreAmp Band,Low
Trigger Source,Free
Trigger Level,1.2
Trigger Slope,Positive
Trigger Delay,0
Phase Noise Optimization,Fast
Swept If Gain,Low
FFT If Gain,Autorange
RF Coupling,DC
FFT Width,411900
Ext Ref,10000000
Input,RF
RF Calibrator,Off
Attenuation,0
Ref Level Offset,0
External Gain,0
Trace Type,Clearwrite
Detector,Peak
Trace Math,Off
Trace Math Oper1,Trace5
Trace Math Oper2,Trace6
Trace Math Offset,0
Normalize,Off
Trace Name,Trace1
X Axis Units,Hz
Y Axis Units,dBm

B.2. Open circuit voltage at antenna

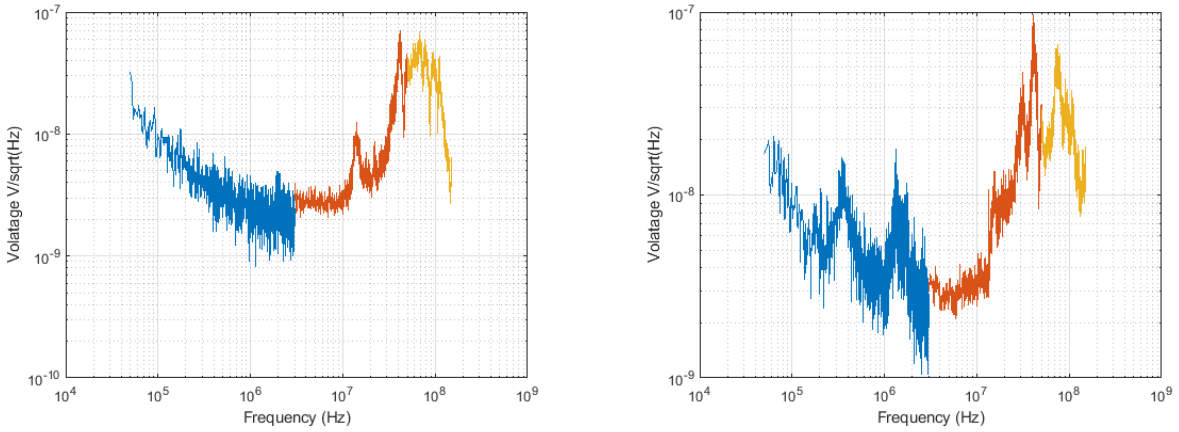

(a) Measured open circuit voltage at the antenna away from the solar panel

(b) Measured open circuit voltage at the antenna near the solar panel

Figure B.3: Measurement of the open circuit voltage on the two antennas with the DC-DC converter being operated via a solar panel for a 50 Ω load.

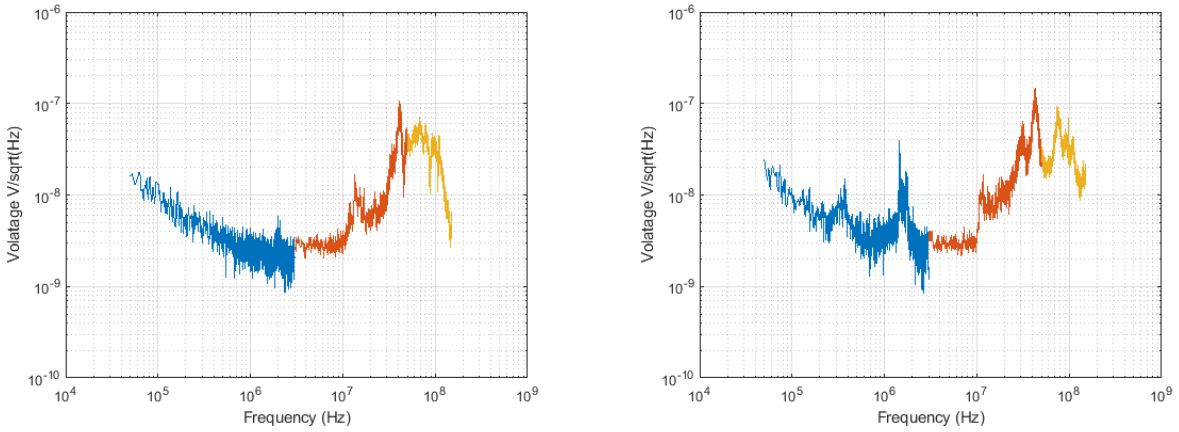

(a) Measured open circuit voltage at the antenna away from the solar panel

(b) Measured open circuit voltage at the antenna near the solar panel

Figure B.4: Measurement of the open circuit voltage on the two antennas with the DC-DC converter being operated via a solar panel for a 150 Ω load.

B.3. Integration test

The test done here were with a DC-DC converter that could not provide the optimal supply voltage, therefore the gain curves that are seen are different from the ones in the text.

Figure B.5: Lab test with DC-DC converter, antenna and low noise amplifier integrated in cubesat.

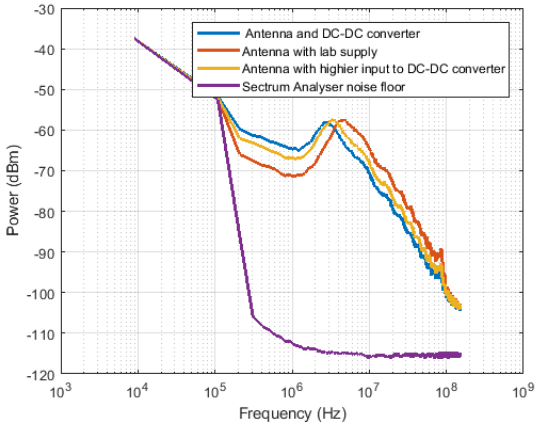

Figure B.6: Image showing the power spectrum of the test with three cases, DC-DC converter input voltage equal to supply voltage, higher than supply voltage and with just the lab power supply..

C

Appendix C

C.1. Implemented Amplifier and Filters

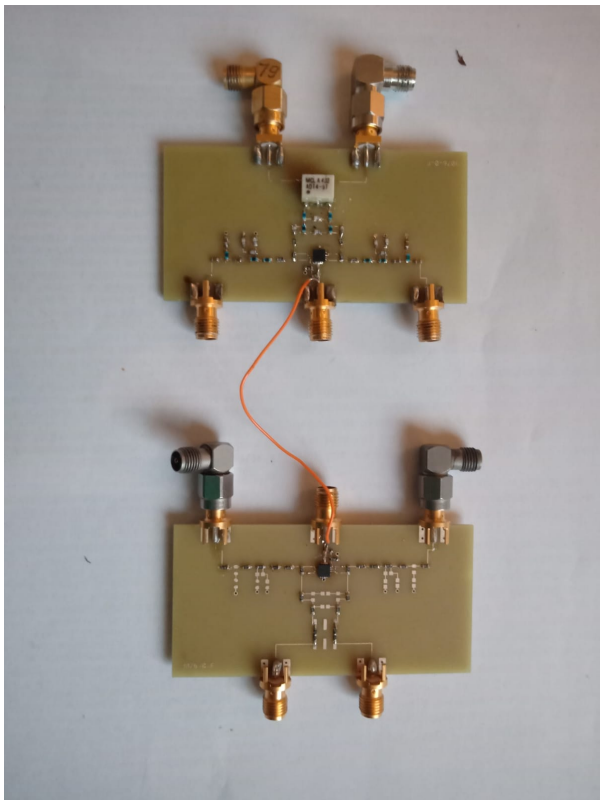

(a) Image showing the analog chain made at ASTRON

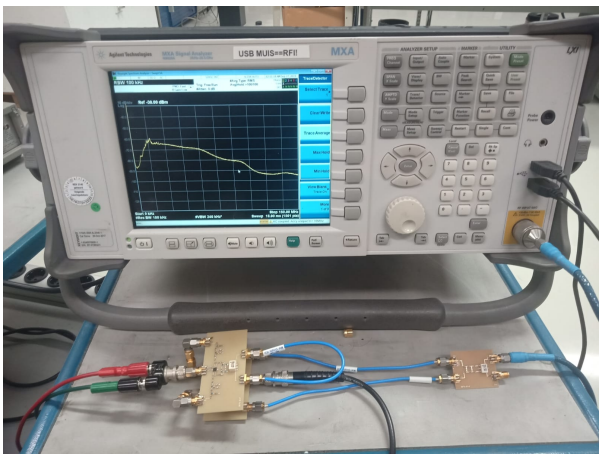

(b) Image showing the analog chain made at ASTRON for measurements.

Figure C.1: Image showing the analog chain made at ASTRON

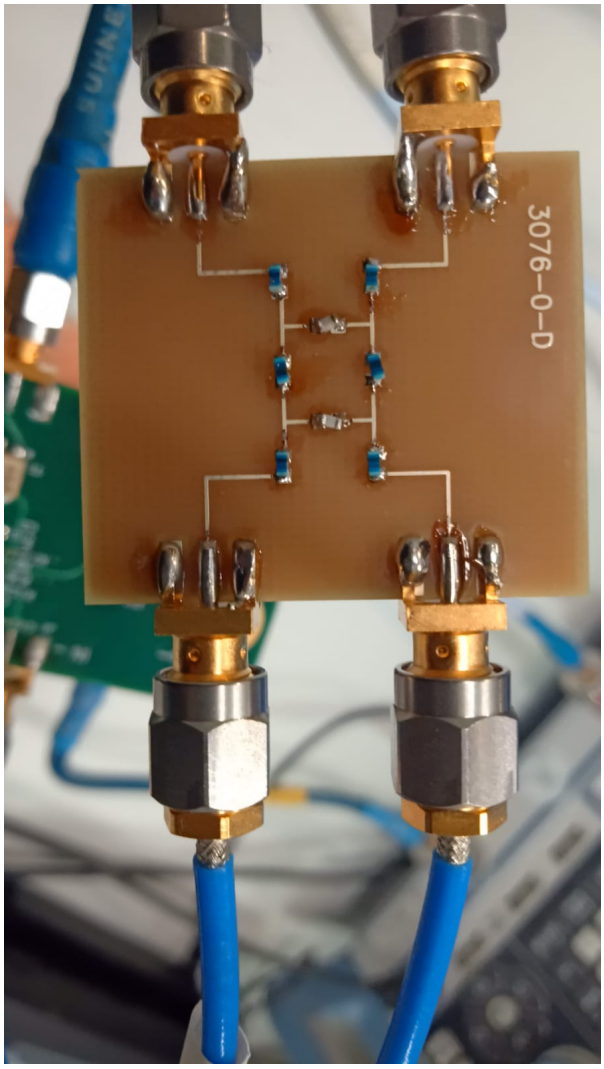

(a) Image showing the differential filter

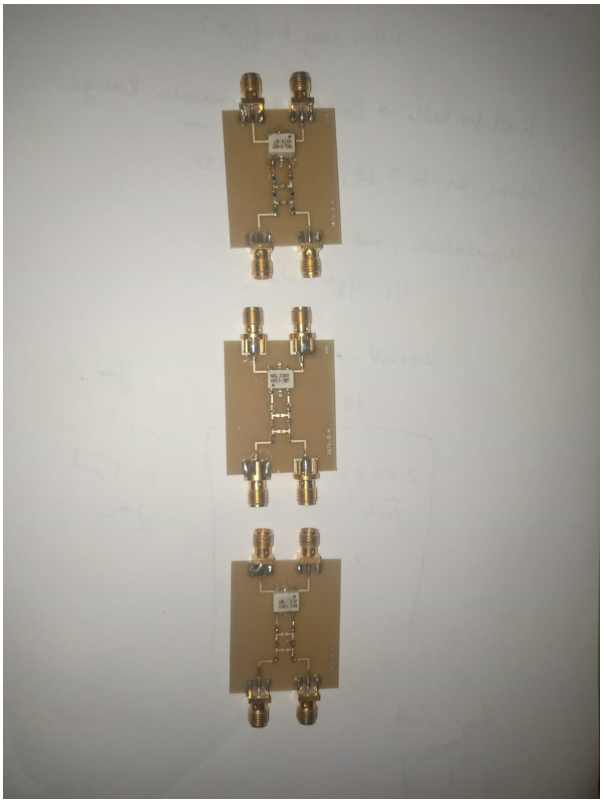

(b) Image showing the differential filter during measurement

Figure C.2: Image showing the differential filter

C.2. Linearity Measurement results

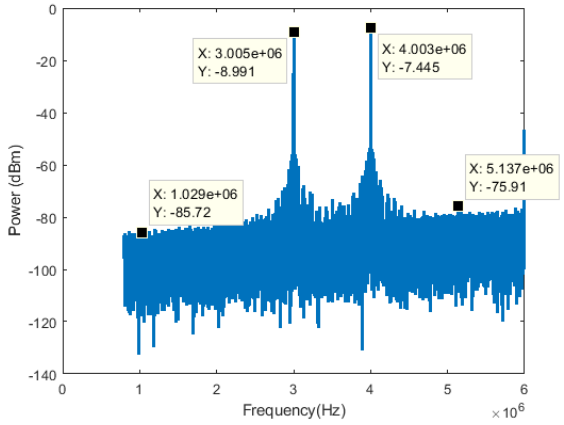

(a) Two tone spectrum at 3 MHz

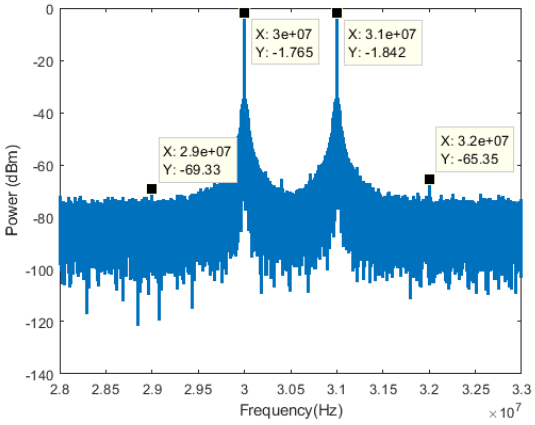

(b) Two tone spectrum at 30 MHz

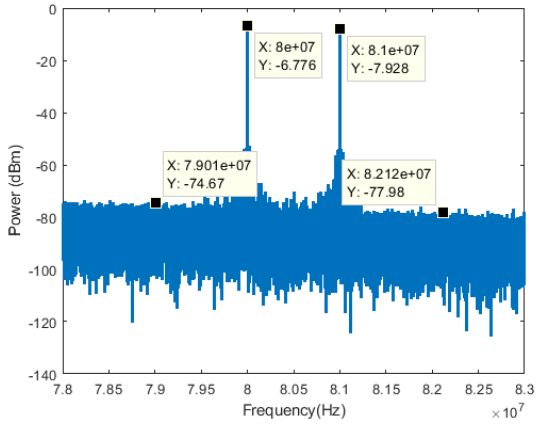

(c) Two tone spectrum at 80 MHz

Figure C.3: Graphs showing the spectrum of the two tone test, showing the third order harmonics with the two fundamental tone levels.

Bibliography

[1] K. G. Jansky. Electrical disturbances apparently of extraterrestrial origin. *Proceedings of the Institute of Radio Engineers*, 21(10):1387–1398, Oct 1933. doi: 10.1109/JRPROC.1933.227458.

[2] Event Horizon Telescope Collaborat, Kazunori Akiyama, Antxon Alberdi, Walter Alef, Keiichi Asada, Rebecca Azulay, Anne-Kathrin Baczko, David Ball, Mislav Balokovic, John Barrett, Dan Bintley, Lindy Blackburn, Wilfred Boland, Katherine L. Bouman, Geoffrey C. Bower, Michael Bremer, Christiaan D. Brinkerink, Roger Brissenden, Silke Britzen, Avery E. Broderick, Dominique Broguiere, Thomas Bronzwaer, Do-Young Byun, John E. Carlstrom, Andrew Chael, Chi kwan Chan, Shami Chatterjee, Koushik Chatterjee, Ming-Tang Chen, Yongjun Chen, Ilje Cho, Pierre Christian, John E. Conway, James M. Cordes, Geoffrey B. Crew, Yuzhu Cui, Jordy Davelaar, Mariafelicia De Laurentis, Roger Deane, Jessica Dempsey, Gregory Desvignes, Jason Dexter, Sheperd S. Doeleman, Ralph P. Eatough, Heino Falcke, Vincent L. Fish, Ed Fomalont, Raquel Fraga-Encinas, William T. Freeman, Per Friberg, Christian M. Fromm, and . First m87 event horizon telescope results. i. the shadow of the supermassive black hole. *Astrophysical Journal Letters*, 875(1), 4 2019. ISSN 2041-8205. doi: 10.3847/2041-8213/ab0ec7.

[3] Baptiste Cecconi, Moustapha Dekkali, Carine Briand, Boris Segret, J. N. Girard, André Laurens, Alain Lamy, David Valat, Michel Delpech, Mickael Bruno, Patrick Gélard, Martin Bucher, Quentin Nénon, Jean-Mathias Griessmeier, Albert-Jan Boonstra, and Mark J. Bentum. Noire study report: Towards a low frequency radio interferometer in space. *2018 IEEE Aerospace Conference*, pages 1–19, 2017.

[4] Wikipedia contributors. Radio telescope — Wikipedia, the free encyclopedia, 2019. URL `https://en.wikipedia.org/w/index.php?title=Radio_telescope&oldid=922305982`. [Online; accessed 26-October-2019].

[5] C. Bianchi and A. Meloni. Natural and man-made terrestrial electromagnetic noise: an outlook. *Annals of Geophysics*, 50(3):435–445, 2007. ISSN 2037-416X.

[6] M. L. Kaiser. A low-frequency radio survey of the planets with rae 2. *Journal of Geophysical Research (1896-1977)*, 82(7):1256–1260, 1977. doi: 10.1029/JA082i007p01256. URL `https://agupubs.onlinelibrary.wiley.com/doi/abs/10.1029/JA082i007p01256`.

[7] J. K. Alexander, M. L. Kaiser, J. C. Novaco, F. R. Grena, and R. R. Weber. Scientific instrumentation of the Radio-Astronomy-Explorer-2 satellite. , 40:365–371, May 1975.

[8] M. J. Bentum, M. K. Verma, R. T. Rajan, A. J. Boonstra, C. J. M. Verhoeven, E. K. A. Gill, A. J. van der Veen, H. Falcke, M. Klein Wolt, B. Monna, S. Engelen, J. Rotteveel, and L. I. Gurvits. A Roadmap towards a Space-based Radio Telescope for Ultra-Low Frequency Radio Astronomy. *arXiv e-prints*, art. arXiv:1909.08951, Sep 2019.

[9] Thyrso Villela, César Augusto Costa, Alessandra Brandão, Fernando Teixeira Bueno, and R. Leonardi. Towards the thousandth cubesat: A statistical overview. 2019.

[10] W. I. Axford. Observations of the Interplanetary Plasma. , 8:331–365, July 1968. doi: 10.1007/BF00184740.

[11] J.-M. Grießmeier, P. Zarka, and J. N. Girard. Observation of planetary radio emissions using large arrays. *Radio Science*, 46(5), 2011. doi: 10.1029/2011RS004752. URL `https://agupubs.onlinelibrary.wiley.com/doi/abs/10.1029/2011RS004752`.

[12] Sebastian Jester and Heino Falcke. Science with a lunar low-frequency array: From the dark ages of the universe to nearby exoplanets. *New Astronomy Reviews*, 53(1):1 – 26, 2009. ISSN 1387-6473. doi: https://doi.org/10.1016/j.newar.2009.02.001. URL `http://www.sciencedirect.com/science/article/pii/S1387647309000086`.

[13] P. Zarka, J.-L. Bougeret, C. Briand, B. Cecconi, H. Falcke, J. Girard, J.-M. Grießmeier, S. Hess, M. Klein-Wolt, A. Konovalenko, L. Lamy, D. Mimoun, and A. Aminaei. Planetary and exoplanetary low frequency radio observations from the Moon. , 74:156–166, December 2012. doi: 10.1016/j.pss.2012.08.004.

[14] Marc Klein Wolt, Amin Aminaei, Philippe Zarka, Jan-Rutger Schrader, Albert-Jan Boonstra, and Heino Falcke. Radio astronomy with the european lunar lander: Opening up the last unexplored frequency regime. *Planetary and Space Science*, 74(1):167 – 178, 2012. ISSN 0032-0633. doi: https://doi.org/10.1016/j.pss.2012.09.004. URL http://www.sciencedirect.com/science/article/pii/S0032063312002796. Scientific Preparations For Lunar Exploration.

[15] George A. Dulk. Radio emission from the sun and stars. *Annual Review of Astronomy and Astrophysics*, 23(1):169–224, 1985. doi: 10.1146/annurev.aa.23.090185.001125. URL https://doi.org/10.1146/annurev.aa.23.090185.001125.

[16] Hamish A. S. Reid and Heather Ratcliffe. A review of solar type iii radio bursts. 2014.

[17] H. G. Schantz. Electromagnetic energy around hertzian dipoles. *IEEE Antennas and Propagation Magazine*, 43(2):50–62, April 2001. doi: 10.1109/74.924604.

[18] Constantine A Balanis. *Antenna theory analysis and design*. Hoboken, New Jersey Wiley, 2016.

[19] Wikipedia contributors. Near and far field — Wikipedia, the free encyclopedia, 2019. URL https://en.wikipedia.org/w/index.php?title=Near_and_far_field&oldid=920688272. [Online; accessed 15-October-2019].

[20] Michael I. Mishchenko. Far-field approximation in electromagnetic scattering. *Journal of Quantitative Spectroscopy and Radiative Transfer*, 100(1):268 – 276, 2006. ISSN 0022-4073. doi: https://doi.org/10.1016/j.jqsrt.2005.11.044. URL http://www.sciencedirect.com/science/article/pii/S0022407305003912. VIII Conference on Electromagnetic and Light Scattering by Nonspherical Particles.

[21] Ieee standard for definitions of terms for antennas - redline. *IEEE Std 145-2013 (Revision of IEEE Std 145-1993) - Redline*, pages 1–92, March 2014.

[22] Ieee standard definitions of terms for antennas. *IEEE Transactions on Antennas and Propagation*, 17(3):262–269, May 1969. doi: 10.1109/TAP.1969.1139442.

[23] Y. Lu, Y. Huang, H. T. Chattha, and P. Cao. Reducing ground-plane effects on uwb monopole antennas. *IEEE Antennas and Wireless Propagation Letters*, 10:147–150, 2011. doi: 10.1109/LAWP.2011.2119459.

[24] Saou-Wen Su, Kin-Lu Wong, Yuan-Tung Cheng, and Wen-Shyang Chen. Finite-ground-plane effects on the ultra-wideband planar monopole antenna. *Microwave and Optical Technology Letters*, 43(6):535–537, 2004. doi: 10.1002/mop.20526. URL https://onlinelibrary.wiley.com/doi/abs/10.1002/mop.20526.

[25] David P. Smith, Martial Arts, A-J Boonstra, and S. J. Wijnholds. Characterisation of astronomical antenna for space based low frequency radio telescope. *2013 IEEE Aerospace Conference*, pages 1–9, 2013.

[26] R. Grootjans. Design of an astronomy front end for orbiting low frequency antennas for radio astronomy, June 2016. URL http://essay.utwente.nl/70404/.

[27] E. Cenacchi, A. Kraus, A. Orfei, and K.-H. Mack. Full stokes polarimetric observations with a single-dish radio telescope. *Astronomy Astrophysics*, 498(2):591–599, Mar 2009. ISSN 1432-0746. doi: 10.1051/0004-6361/200811210. URL http://dx.doi.org/10.1051/0004-6361/200811210.

[28] S. J. Wijnholds, M. V. Ivashina, R. Maaskant, and K. F. Warnick. Polarimetry with phased array antennas: Sensitivity and polarimetric performance using unpolarized sources for calibration. *IEEE Transactions on Antennas and Propagation*, 60(10):4688–4698, Oct 2012. doi: 10.1109/TAP.2012.2207340.

[29] T. D. Carozzi and G. Woan. A fundamental figure of merit for radio polarimeters. *IEEE Transactions on Antennas and Propagation*, 59(6):2058–2065, June 2011. doi: 10.1109/TAP.2011.2123862.

[30] J. Rajesh, S. Shastry, M. Thyagaraj, M. Rao, N. Ghatpande, and T. Danabalan. Emi prediction and analysis for experimental payloads of advanced communication technology satellite — gsat-4. In *2006 9th International Conference on Electromagnetic Interference and Compatibility (INCEMIC 2006)*, pages 53–59, Feb 2006.

[31] Anton J.M. Montagne. *structured electronic design a conceptual approach to amplifier design*. Delft Academic Press, 1.1 edition, 01 2019.

[32] Mil-std reference documents, 2004. URL `https://snebulos.mit.edu/projects/reference/MIL-STD`.

[33] Atsushi Kumamoto, Takayuki Ono, Yoshiya Kasahara, Yoshitaka Goto, Yuichi Iijima, and Satoru Nakazawa. Electromagnetic compatibility (emc) evaluation of the selene spacecraft for the lunar radar sounder (lrs) observations. *Earth, Planets and Space*, 60:333–340, 2008.

[34] David S. Prinsloo, Marvin Ruiter, Martial Arts, J. van de Marel, Albert-Jan Boonstra, Gert H. Kruithof, Michael Wayne Wise, Heino Falcke, Marc Klein-Wolt, and Jinglei Ping. Emi modelling of an 80 khz to 80 mhz wideband antenna and low-noise amplifier for radio astronomy in space. 2018.

[35] Wikipedia contributors. Noise temperature — Wikipedia, the free encyclopedia, 2019. URL `https://en.wikipedia.org/w/index.php?title=Noise_temperature&oldid=886818709`. [Online; accessed 14-November-2019].

[36] John Mckean. Introduction to radio astronomy.

[37] L. Belostotski and J. W. Haslett. A technique for differential noise figure measurement of differential lnas. *IEEE Transactions on Instrumentation and Measurement*, 57(7):1298–1303, July 2008. doi: 10.1109/TIM.2008.917673.